
# BRNO UNIVERSITY OF TECHNOLOGY

VYSOKÉ UČENÍ TECHNICKÉ V BRNĚ

## CENTRAL EUROPEAN INSTITUTE OF TECHNOLOGY BUT

STŘEDOEVROPSKÝ TECHNOLOGICKÝ INSTITUT VUT


# QUANTITATIVE COMPUTED TOMOGRAPHY

KVANTITATIVNÍ POČÍTAČOVÁ TOMOGRAFIE

SHORT DOCTORAL THESIS

TEZE DIZERTAČNÍ PRÁCE


AUTHOR — Ing. Jakub Šalplachta

AUTOR PRÁCE

SUPERVISOR — prof. Ing. Jozef Kaiser, Ph.D.

ŠKOLITEL



BRNO 2022

**Summary**

The main aim of this thesis is to study, explore and possibly move further the field of quantitative computed tomography (QCT) with specific focus on a laboratory-based submicron computed tomography (CT) system Rigaku nano3DX. This work is dealing with both aspects of the QCT, which are the acquisition of quantitative CT data and the utilization of CT data for quantitative analysis. Regarding the first aspect, specific focus is placed on assessment of current technological limits of submicron CT, where the technology-based tomographic artifacts are studied, and optimal reduction strategies are proposed. Also, practical aspects related to implementation of spectral CT in a form of dual-target CT (DTCT) using Rigaku nano3DX system, are solved by development of dedicated acquisition and data registration methodologies. For the quantitative analysis of CT data, two novel methods were developed. One was specifically designed for porosity analysis of additive manufactured samples with a respect to the crucial points of tomographic data processing, making it objective and reproducible. Second method was specifically designed for quantitative assessment of 3D models of biological tubular systems and was practically tested on a mouse model of Alagille syndrome.

**Abstrakt**

Hlavním cílem této práce je prostudovat, prozkoumat a případně posunout dále oblast kvantitativní počítačové tomografie (QCT) se specifickým zaměřením na laboratorní submikronový CT systém Rigaku nano3DX. Tato práce se zabývá oběma aspekty QCT, kterými jsou akvizice kvantitativních CT dat a využití CT dat pro kvantitativní analýzu. Pokud jde o první aspekt, specifický důraz je kladen na posouzení současných technologických limitů submikronového CT, kde jsou studovány tomografické artefakty způsobené právě technickými nedostatky a navrženy optimální redukční strategie. Také praktické aspekty spojené s implementací spektrálního CT ve formě dual-targetového CT (DTCT) pomocí systému Rigaku nano3DX jsou řešeny vývojem specializovaných metodologií pro akvizici a registrace dat. Pro kvantitativní analýzu CT dat byly vyvinuty dvě nové metody. Jedna z metod byla speciálně navržena pro analýzu porozity vzorků vyrobených metodou 3D-tisku a to s ohledem na klíčové aspekty zpracování tomografických dat, díky čemuž je tato metoda objektivní a reprodukovatelná. Druhá metoda byla speciálně navržena pro kvantitativní hodnocení 3D modelů biologických tubulárních systémů a byla prakticky testována na myším modelu Alagilleova syndromu.

**Keywords**

Quantitative Computed Tomography, QCT, CCD, sCMOS, tomographic artifacts reduction, dual-energy CT, porosity analysis, 3D models analysis

**Klíčová slova**

Kvantitativní počítačová tomografie, QCT, CCD, sCMOS, redukce tomografických artefaktů, duálně-energiové CT, analýza porosity, analýza 3D modelů

ŠALPLACHTA, Jakub. *Quantitative computed tomography.* Brno, 2023. Doctoral Thesis. Vysoké učení technické v Brně, Středoevropský technologický institut VUT, Central European Institute of Technology BUT. Supervisor Jozef Kaiser.

# Table of Contents


Introduction ..... 1

1 Aims of Thesis ..... 3

1.1 Reduction of technology-based tomographic artifacts ..... 3

1.2 Spectral imaging ..... 3

1.3 Quantitative analysis of CT data ..... 4

2 Methods ..... 5

2.1 CT devices ..... 5

2.1.1 Rigaku nano3DX ..... 5

2.1.2 GE phoenix v|tome|x L240 ..... 5

2.1.3 ThermoFisher Scientific Heliscan ..... 5

2.2 Software ..... 6

2.3 Practical assessment of a detector and image data quality ..... 6

3 Reduction of technology-based tomographic artifacts ..... 9

3.1 Optimization of parameters for analytical tomographic reconstruction ..... 9

3.1.1 Materials and methods ..... 9

3.1.2 Results ..... 11

3.1.3 Summary ..... 15

3.2 Practical assessment of detectors for submicron CT applications ..... 16

3.2.1 Materials and methods ..... 16

3.2.2 Results ..... 18

3.2.3 Summary ..... 24

3.3 Noise reduction for submicron CT data ..... 25

3.3.1 Noise model ..... 25

3.3.2 Proposed algorithm for estimation of noise absolute deviation ..... 26

3.3.3 Proposed algorithm for impulse noise reduction ..... 27

3.3.4 Shot noise reduction ..... 30

3.4 Ring artifacts reduction ..... 34

3.5 Assessment and reduction of rotational stages limitations ..... 37

3.5.1 Analysis of rotational stage stability ..... 37
3.5.2 Correction of rotational stage imprecision and instability ..... 43
4 Spectral imaging ..... 46
4.1 DTCT imaging using Rigaku nano3DX device ..... 46
4.2 DTCT acquisition settings ..... 48
4.2.1 Noise dependence on acquisition parameters ..... 48
4.2.2 Proposed strategies for exposure estimation ..... 53
4.3 DTCT data registration ..... 56
5 Quantitative analysis of CT data ..... 58
5.1 CT analysis of additive manufactured samples ..... 58
5.1.1 Reproducible porosity analysis (RPA) ..... 59
5.2 CT analysis of a mouse model for Alagille syndrome ..... 61
5.2.1 Quantitative analysis of 3D models of tubular systems ..... 62
6 Conclusion ..... 66
References ..... 67
Author's publications and other outputs ..... 77
Publications ..... 77
First-author ..... 77
Shared first-author ..... 77
Co-author ..... 77
Products ..... 78
Grants ..... 78
Conferences ..... 79

# Introduction

X-ray Computed Tomography (CT) is an imaging method used for a non-destructive evaluation (NDE) of internal structures of a sample. Although this technique was originally developed for medical applications, in the last decades it has been also utilized in various industrial and scientific fields. In principle, a set of projection images is acquired from various angles of a sample's rotation by X-ray beam illumination and detection of the attenuated radiation after sample passing. From such measured data, a 3D sample's information is retrieved using a reconstruction algorithm. The resulting CT data can be then utilized for various purposes from visualization to dedicated analysis of sample's properties – e.g., morphology, voids and pores detection, material properties and distribution etc. Especially in the recent years, the technical progress in field of high-resolution CT (referring to achievable spatial resolution on micron or submicron level) enabled utilization of this technique for quantitative analysis or as a dimensional metrology tool. [1; 2; 3]

However, CT technique suffers from many limitations of an acquisition process itself. The polychromatic nature of X-ray radiation used in standard CT scanners is responsible for dependence of attenuation properties of any sample˙s compound not only on its density and chemical composition but also on used CT system parameters and settings and moreover on the surrounding materials. Moreover, the accuracy of CT data can be further distorted by various tomographic artifacts. All those effects together distort the reliability and accuracy of resulting CT data. The main objective of Quantitative CT (QCT) is then a quantitative measurement of sample˙s properties based on undistorted attenuation information that is solely dependent on its internal composition. In industrial or scientific sphere of CT, these characteristics can, for instance, be: dimensional measurements [4], fibre's orientations [5], porosity analysis [6] or other parameters characterizing structures or material properties of given sample. The application of a high-resolution CT has already proven its applicability and benefits in various fields from R&D to basic research.

However, aiming for higher spatial resolution and implementation of advanced CT techniques (e.g., 4D CT or spectral CT), brings strict requirements for both the hardware and the software. Moreover, the crucial task for every technique used for any metrological assessment is determining measurement uncertainty, which requires analysis of all critical error sources. In recent years, spectral imaging methods (also known as multi-energy CT or dual-energy CT) have remerged in CT practise, that aim to increase the overall accuracy and quality of CT imaging and to practical implementation of advanced quantification tools for sample's characterization. However, practical implementation of spectral CT was lagged by the technological limits that were not solved up to recent years. Especially in sphere of high-resolution CT, the possibility of acquisition of undistorted CT data and its' further quantitative analysis is still highly limited by various technological aspects and lack of dedicated methodologies and correction solutions.

The main aim of this thesis is to study, explore and possibly move further the field of quantitative computed tomography (QCT) with specific focus on a laboratory-based submicron computed tomography (CT) system Rigaku nano3DX. This work is dealing with both aspects of the QCT, which are the acquisition of quantitative CT data and the utilization of CT data for quantitative analysis. Regarding the first aspect, specific focus is placed on an assessment of current technological limits of submicron CT, where the technology-based tomographic artifacts are studied, and optimal reduction strategies are proposed. Also, practical aspects related to implementation of spectral CT in a form of dual-target

CT (DTCT) using Rigaku nano3DX system, are solved by development of dedicated acquisition and data registration methodologies. For the quantitative analysis of CT data, two novel methods were developed. One was specifically designed for porosity analysis of additive manufactured samples with a respect to the crucial points of tomographic data processing, making it objective and reproducible. Second method was specifically designed for quantitative assessment of 3D models of biological tubular systems and was practically tested on a mouse model of Alagille syndrome.

Presented thesis can be divided into six main parts. In the first part, a theoretical background and literature review regarding the thesis topic is given. The focus is placed on subsection regarding tomographic reconstruction and technology-based tomographic artifacts, where existing solutions for their reduction are presented. Subsequently the aims of this thesis are described in more details. Following chapter contain description of CT devices, software and CT data quality assessment metrics used within scope of this work. Next three chapters contain overview and description of outcomes that have been achieved within the aims of this thesis. These are mainly focused on assessment of technology-based tomographic artifacts and development of dedicated reduction approaches. Further, the practical implementation of dual-target CT using Rigaku nano3D system is presented focused on development of dedicated acquisition and data registration methodologies. For the quantitative analysis of CT data, two novel methods are presented for porosity analysis of additive-manufactured samples and for analysis of 3D models of biological tubular systems.

# 1 Aims of Thesis

The general aim of this thesis is to study, explore and possibly move further the field of Quantitative CT, specifically dealing with submicron CT system Rigaku nano3DX. The content of this work can be divided into three major parts covering different aspects of QCT: the first part is dedicated to studying technical limitations of submicron CT and development of dedicated reduction strategies; second part is dedicated to practical implementation of spectral imaging in a form for dual-target CT; and the third part focuses on quantitative analysis of CT data.

## 1.1 Reduction of technology-based tomographic artifacts

The application of a high-resolution CT has already proven its applicability and benefits in various fields from R&D to basic research. However, aiming for higher spatial resolution and implementation of advanced CT techniques (e.g., 4D CT or spectral CT), brings strict requirements for both the hardware and the software. Especially in sphere of high-resolution CT, the possibility of acquisition of undistorted CT data is still highly limited by various technological aspects and lack of dedicated methodologies and correction solutions. In this work, specific focus is placed on assessment of the technological limits of submicron CT practically implemented using Rigaku nano3DX device, where the technology-based tomographic artifacts are studied, and optimal reduction strategies are proposed. Within realization of this aim several sub-tasks can be defined:

- determination of optimal reconstruction process for Rigaku nano3DX data using the ASTRA tomography toolbox,
- determination of optimal detector in terms of quality and accuracy of acquired data,
- development of noise reduction methodology for Rigaku nano3DX data,
- development of ring artifacts reduction solution for Rigaku nano3DX data,
- development of a solution for correction of rotational stage instability and inaccuracy during CT acquisition using Rigaku nano3DX.

## 1.2 Spectral imaging

Spectral CT, or multi-energy CT, is perceived as one of the key technologies for future development of CT in general. Spectral imaging methods generally aim to increase overall accuracy and quality of CT imaging including methods for tomographic artifacts reduction and to practical implementation of advanced quantification tools for sample's characterization. In terms of practical implementation of spectral CT, two main concepts can be applied, either the detector-based or X-ray source-based. The focus of this work is X-ray source-based dual-energy CT (DECT), which refers to scanning at two energy levels and is a special case of spectral CT. Dedicated CT systems were designed exclusively for DECT, such as the Rigaku nano3DX system, where this technique is implemented in a unique form of dual-target CT (DTCT). Using this device, not only two energy separate X-ray spectra but also material specific spectra can be achieved during DECT by switching the X-ray source target material. However, all the X-ray source-based approaches are practically limited by possible misalignment of acquired data and also by lack of knowledge about practical aspects of setting up DECT measurements. In this work, both these issues are addressed and practically implemented for Rigaku nano3DX device. The practical realization of this aim can be divided into following sub-tasks:

- determination of optimal DTCT acquisition process using Rigaku nano3DX,

- development of optimal registration procedure for DTCT data acquired by Rigaku nano3DX.

## 1.3 Quantitative analysis of CT data

CT data can be in general utilized for various purposes from visualization to dedicated analysis of sample's properties – e.g., morphology, voids and pores detection, material properties and distribution etc. However, there is still a lack of dedicated and fully automatic data processing tools for CT data, that would utilize its' full potential. This results into either using CT for visualization purposes only, or quantifying the CT data using non-standardized procedures based on operator's expertise and skills. However, these aspects rule out any trustworthy or reproducible results. Therefore, the aims of this work can be specified as:

- development of objective and reproducible porosity analysis procedure based on CT data,
- development of quantitative analysis tools for 3D models of biological tubular systems based on CT data.

# 2 Methods

In the following section, CT devices used for experiments in this doctoral thesis are described: Rigaku nano3DX, GE phoenix v|tome|x L240 and ThermoFisher Scientific Heliscan, all located at CEITEC Brno University of Technology. Apart from the utilized CT devices, the software tools, used evaluation metrics and standards are further described.

## 2.1 CT devices

### 2.1.1 Rigaku nano3DX

Most of the experiments and CT data presented in this work were acquired using laboratory-based CT system Rigaku nano3DX. Rigaku nano3DX is a detector-based submicron CT system. Achieving such high resolution is accomplished by using a high-power rotation anode X-ray source and high-resolution detection system. In the nano3DX, the magnification takes place in the detector using optical elements which results in small sample to detector distances. Using such settings, near-parallel beam geometry is achieved. This system also enables switching anode materials to optimize contrast for specific sample types, these materials are Cu and Mo. Apart from the material the targets also differ in terms of used tube current and voltage (Cu: 40 kV and 30 mA; Mo: 50 kV and 24 mA) and also in shape and size of a X-ray spot (effective size at 6° take-off angle: Cr and Cu – 0.07 mm circle; Mo – 0.15 x 0.1 mm ellipse). This machine has also possibility of utilization of a unique X-ray rotary target that enables Dual-Target CT (DTCT) measurements. Using such target not only two energy separate X-ray spectra but also material specific spectra are acquired.

### 2.1.2 GE phoenix v|tome|x L240

Industrial microCT system, GE phoenix v|tome|x L240, was used within analysis of rotational stage stability (section 3.5.1) and for application studies dealing with quantitative analysis of CT data (section 5). This microCT system is placed in the air-conditioned, walking cabinet where all components are on the granite-based 7-axis manipulator. This setup has the cone-beam geometry and is equipped with GE DXXR 250 flat panel detector. The sample limitations for this setup are: 500x800 $mm^3$ in terms of volume and 50 kg in terms of weight. This system can be equipped with two X-ray sources, which are the unipolar microfocus source and high-power nanofocus X-ray tube. Nominal parameters of these sources are stated in Table 1. [7]

*Table 1: Nominal parameters of GE phoenix v|tomex|x L240 X-ray sources, LVS – linear voxel size.*

| X-ray source | Voltage/ Power | Maximal LVS |
|---|---|---|
| Microfocus tube | 240 kV/ 320 W | ~ 2 µm |
| Nanofocus tube | 180 kV/ 15 W | ~ 1 µm |

### 2.1.3 ThermoFisher Scientific Heliscan

MicroCT system, ThermoFisher Scientific Heliscan, was used within analysis of rotational stage stability (section 3.5.1). This system is equipped with micro-focus X-ray source with tungsten target achieving 8W power and maximum accelerating voltage of 160 kV. The applicable focal spot size varies between 0.8 µm and 4 µm according to applied settings. The detector is a 16bit flat panel with 3072 × 3072 pixels and pixel size 139 µm. The setup has cone-beam geometry with maximum applicable SSD 130 mm and maximum applicable SDD 750 mm, using this arrangement voxel resolution up to 0.8 µm can

be achieved. For CT acquisition, several scanning trajectories are available: circular and helical with several options – single helix, double helix and space filling [8]. Using the helical scanning trajectory, tall samples, up to 100 mm, can be scanned without stitching.

## 2.2 Software

List of utilized software tools for data processing and analysis used within scope of this thesis is summarised in Table 2.

*Table 2: List of software used in this thesis for data processing and analysis.*

| **Software** | **Use** |
|---|---|
| Matlab® | Data processing and analysis |
| ImageJ [9] | Data visualization and analysis |
| VGStudio MAX | Data visualization and analysis |
| ASTRA Toolbox [10] | Tomographic reconstruction |

## 2.3 Practical assessment of a detector and image data quality

Several characteristics describe the quality of image data acquired by a detector, when these are mainly governed by noise and signal properties. In the Table 3, the utilized evaluation metrics are introduced together with ways of computing those measures from specific measurements.

*Table 3: List of evaluated image quality metrics with corresponding calculations used in this work.*

| **Category** | **Parameter** | **Definition/Calculation** |
|---|---|---|
| **Data quality** | Contrast to Noise Ratio (CNR) | $$CNR = \frac{\lvert\mu_o - \mu_b\rvert}{\sigma_b},$$ where $\mu_o$ and $\mu_b$ are mean intensity values of object and background respectively and $\sigma_b$ is standard deviation of background. [11] |
| | Signal to Noise Ratio (SNR) | $$SNR = \frac{\mu_o}{\sigma_b},$$ where $\mu_o$ is mean intensity value of object and $\sigma_b$ is standard deviation of background. [11] |
| | Local Contrast (C) | $$C = \frac{g_{max} - g_{min}}{g_{max} + g_{min}},$$ where $g_{max}$ and $g_{min}$ denote the maximal respectively minimal intensity values in the region of interest defined by a support window R centred around $i_0$, $j_0$ spatial coordinates. [11] |
| | Variance (VAR) | $$VAR = \frac{1}{n} \sum_{(i,j)\in R_{i0,j0}} (g(i,j) - \mu_R),$$ |

| | | |
|---|---|---|
| | | where $n$ is number of pixels (voxels) in support window $R$ centred around $i_0$, $j_0$ spatial coordinates, $g(i,j)$ is intensity value at spatial coordinates $i$, $j$ and $\mu_R$ is mean intensity value in window $R$. [11] |
| | Sum of Modified Laplacians (SML) | $$SML(i_0, j_0) = \sum_{(i,j) \in R} (\lvert -g(i+s,j) + 2g(i,j) - g(i-s,j) \rvert + \lvert -g(i,j+s) + 2g(i,j) - g(i,j-s) \rvert),$$ where R is support window centred around $i_0$, $j_0$ spatial coordinates, $g$ denotes intensity value at specified spatial coordinates and $s$ is defined step parameter. [11] |
| | Just Noticeable Blur (JNB) | $$JNG = c\frac{\sum w(e_{i,j})}{E},$$ where $e_{i,j}$ denotes edge pixel at spatial coordinates $i$, $j$ and $w$ is corresponding edge width, $E$ denotes number of all edge pixels and $c$ is a real valued factor. [11] |
| **Linearity** | Linearity analysis | Graphical plot analysis of detected signal as a function of exposure time / evaluated for bright-field frames. Linearity was then expressed as the root mean square of the distances between detected signal points and the linear regression fit line (a linear least-squares regression model was used). |
| **Noise properties** | Readout noise | Readout noise was extracted from the set of bias frames (i.e., dark-field frames acquired with the minimal exposure) by subtraction of average bias frame and then quantified using standard deviation. |
| | Dark current | For quantification linearity analysis of dark-field frames was used. Frames were acquired for exposures from 1 s to 30 s and from each frame mean bias frame was subtracted. Resulting dependence of average dark current signal on exposure time was then fitted using linear regression and the dark current was then defined as the slope of this fit. |
| | Total noise | Total noise is a compound of all noise sources. It was quantified from set of bright-field frames by subtraction of an average bright-field frame from intensity stabilized frames and then quantified using standard deviation calculation. |
| | Noise power spectrum (NNPS) | The NNPS is a characterization of the noise in the spatial frequency domain. In this work, we incorporated NNPS calculation as specified in IEC 62220-1: 2003(E) standard [12]: $$NNPS\,(u,v) = \frac{1}{S^2} \cdot \frac{\Delta x \Delta y}{M \cdot 256 \cdot 256} \cdot \left( \lvert DFT2(n_{ij}) \rvert^2 \right),$$ where $S$ denotes average signal in the subset, $\Delta x$ and $\Delta y$ are the pixel size in horizontal respectively vertical directions, $M$ is number of subsets, DFT2 denotes the discrete 2D Fourier transform and $n_{i,j}$ is extracted 2D noise image from given subset. |

| | | |
|---|---|---|
| | Hot pixels | Hot pixels are pixels with dark current significantly above the average. They were detected based on analysis of dark-field frames with 10 exposure levels from 20 s to 30 s. From such frames mean bias frames were subtracted so only dark current map images remained. In these images extreme dark values were detected using this formula:<br>$$g(x,y) = \begin{cases} 1, & if\ f(x,y) \geq M + 3 \cdot s \\ 0, & if\ f(x,y) < M + 3 \cdot s \end{cases}$$<br>where *f(x,y)* is analysed dark current frame for given exposure, *M* is median dark current value and s is the standard deviation (both calculated from *f*) and *g(x,y)* is binary value of output binary image g both at corresponding spatial coordinates x, y. As hot pixels were then considered pixels with extreme dark current values whose positions was not changing within analysed frames. |
| | Random hot pixels | These pixels are defined analogously as hot pixels but are mostly caused by scattered radiation. For detection similar scheme as for hot pixels was applied but in case of random hot pixels their positions were random within the frames. |
| **Spatial resolution** | JIMA RT RC-02B resolution test | Graphical analysis of minimal resolvable pattern – line profiles over selected pattern charts in both horizontal and vertical directions. For analysis representative frames were used – pixel-wise averaging of acquired frames with extreme values exclusion. To avoid any remaining effect of noise, analysed line profiles were taken through a band of 100 pixels thickness. |
| | Modulation transfer function (MTF) | MTF is considered as a measure of the spatial resolution of a liner imaging system. This function was calculated using procedure defined in: ASTM E1695-95(2013) standard [13]. As disk phantom a ruby ball with diameter 0.3 mm was used and corresponding CT data were acquired using acquisition parameters that simulated standard measurement scenario. From CT slice located at centre of used phantom the composite edge disk profile was generated and used for calculation of the edge response function (ERF). From this function the point spread function (PSF) was obtained as the derivate. MTF was then calculated as unity normalized amplitude of PSF Fourier transform.<br>Spatial resolution (*SR*) calculation:<br>$$SR = \frac{1}{2 \cdot MTF_{10\%}} \cdot vx,$$<br>$MTF_{10\%}$ is a frequency value [lp/voxel] at 10 % of MTF and *vx* is voxel-size value. |

# 3 Reduction of technology-based tomographic artifacts

In this chapter, are presented results, that have been achieved dealing with the topic of reduction of technology-based tomographic artifacts. These results are mostly focused on studying such artifacts and development of dedicated reduction strategies with specific focus on Rigaku nano3DX system.

## 3.1 Optimization of parameters for analytical tomographic reconstruction

Although it may seem that tomographic reconstruction is not related to the topic of technology-based tomographic artifacts, the truth is the opposite. It is an essential step of CT data acquisition process, when a selection of specific reconstruction algorithm and its settings has key importance for reconstructed CT data quality. This is valid especially for the class of analytical reconstruction methods, where the selection of the shape of apodized filter and its cut-off frequency is crucial using FBP-based algorithms. Therefore, this section is focused on searching optimal analytical reconstruction procedure using ASTRA tomography toolbox [10] for reconstruction of submicron CT data acquired by Rigaku nano3DX device. [14]

### 3.1.1 Materials and methods

Using implementation of FBP in ASTRA toolbox (v1.9.0), two parameters can be selected. These are: filter type and the cut-off point in the frequency domain. Regarding the filter type, 16 filters are available in ASTRA, where the Ramp filter can be considered as a standard. This filter is the high-pass filter with zero transmission of DC component and linear increase towards the highest frequencies, which leads to accentuation of high frequencies (i.e., image details and noise component). Therefore, for tomographic reconstruction of data that contain noise, it is better to weight the Ramp filter by specific function. The actual shape of the filter's transmission function has the effect on high frequencies reduction during the reconstruction process affecting the spatial resolution and noise properties in tomogram data. All the filters aim at reduction the frequency information through an amplitude of their transmission functions, i.e., adjusting this function inside the frequency interval from 0 Hz to Nyquist frequency (Nq). Specifically, Cosine and Hamming filters achieve good results in terms of noise suppression, but they do not preserve edges and details (their transmission reaches zeros zero quickly near the highest frequencies). The cut-off point in the frequency domain specifies the threshold above which higher frequencies are eliminated (see Figure 1). Setting this value to 1.0 will include the whole filter range without any effect on the transmission function shape (cut-off point value times the Nq frequency = the highest frequency that can be displayed in the image (0.5 cycles/pixel)). High value of this parameter leads to improvement of spatial resolution but neglecting the noise reduction. Values higher than 1.0 amplifies the transmission of high frequencies, which can be advantageous for some filter types in terms of details preservation. For images containing a high degree of complexity, the trade-off between the noise removal and features preservation needs to be find (i.e., compromise between the extent of noise reduction and fine details suppression). [14]

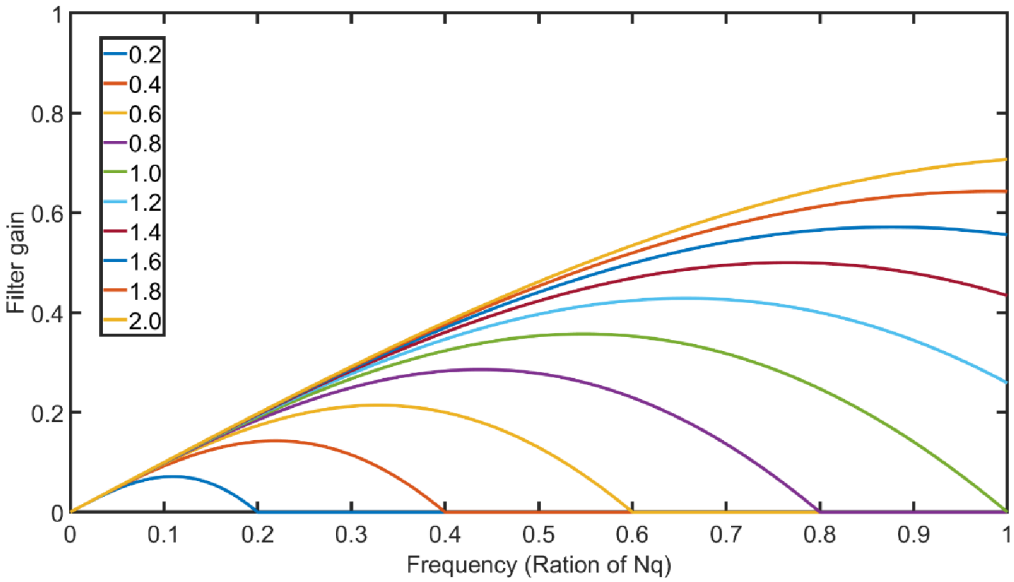


*Figure 1: Dependence of Cosine filter transmission functions in frequency domain based on used cut-off point values (used range from 0.2 to 2). [14]*

Specifically, all available 16 filters in ASTRA Toolbox were evaluated for range of cut-off points from interval 0.1 to 5.0 with step 0.1. This optimization was done using brute-force search with quantitative performance evaluation using two numerical metrics. These were: the peak signal-to-noise ratio (PSNR) and structural similarity index (SSIM) [15]. Apart from optimization of filtering settings, the dependence of noise reduction together with spatial resolution preservation on filtering settings were also studied. For evaluation of noise reduction, Signal to Noise Ratio (SNR) was used and in case of spatial resolution evaluation, the line profile analysis was conducted. For this evaluation synthetic data were generated. Specifically, 4 types of data were used (see Figure 2). These images were generated in image (tomogram) domain and then forward projected to sinogram domain. The data were simulated to have similar parameters as real nano3DX data, specifically to have pixel size 0.54 µm, used detector width 1648 pixels and to follow acquisition of 800 projection angles from angular range of 0° to 180°. To further test the effect of filter settings on noise reduction, Gaussian distributed noise with standard deviation 0.01 (reflects noise properties of real projection data) was added to generated sinograms. [14]

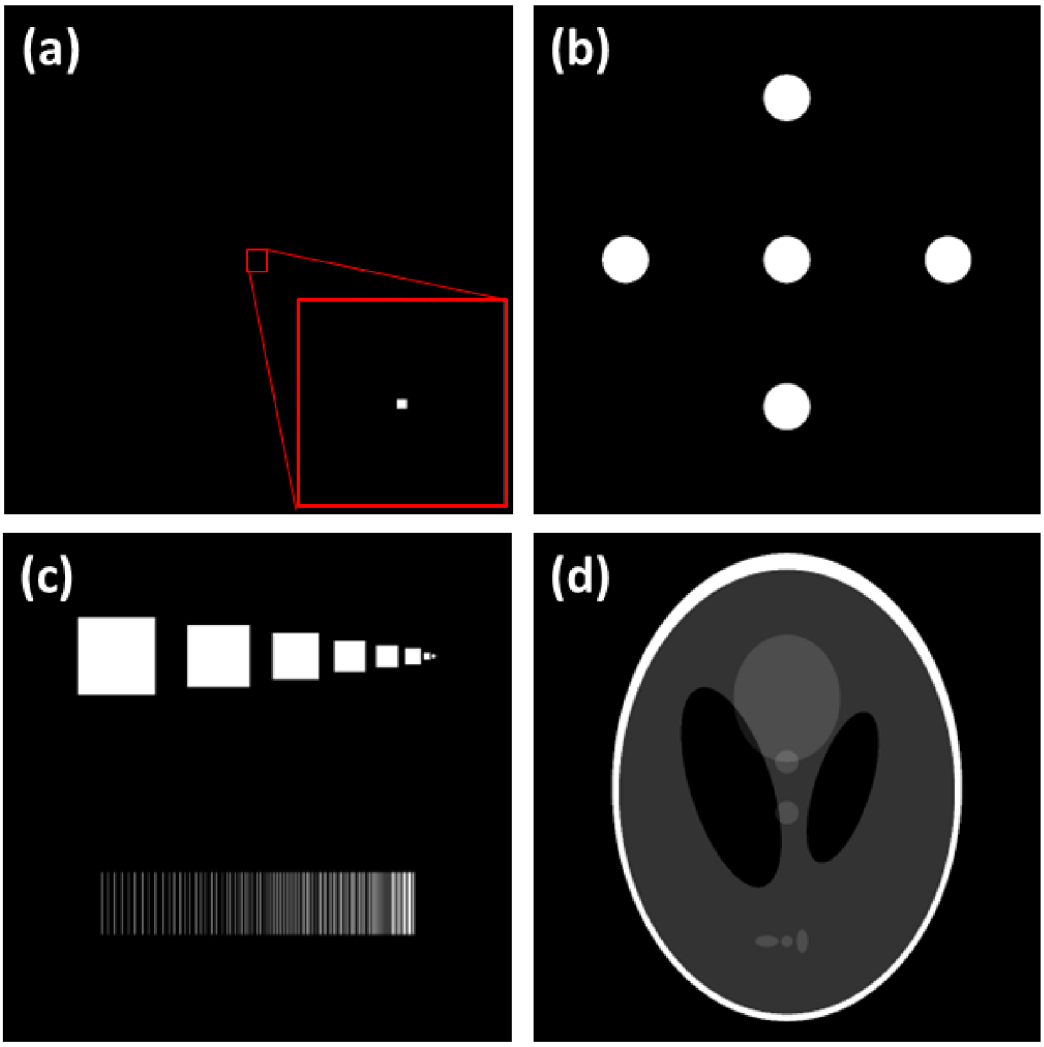


*Figure 2: Generated synthetic data for optimization of FBP filtering setting: a) Dirac delta function; b) circles phantom; c) spatial resolution phantom and d) Shepp-Logan phantom. [14]*

### 3.1.2 Results

#### *3.1.2.1 Filtration settings evaluation for ideal data*

It should be stated that this optimization was done assuming ideal conditions i.e., no noise and other tomographic artifacts presence in the data. The optimal filtration settings were estimated for each of 4 phantom images separately and then overall optimal settings was evaluated. It was revealed that FBP based reconstruction even with optimal settings is not an ideal system, when its response to Dirac delta function is not a point-spread function (see Figure 3). From line profile analysis of reconstruction results using filtration settings with the best score (see Figure 4), it is evident that in all the cases intensity was decreased and that the point-spread function was blurred. The best overall score achieved filtration settings using cosine filter with cut-off point 2.0 (see Table 4). From Figure 5, it is evident that transmission functions of filtration settings with best overall score are having almost the same course, forming an ideal transmission function for noise- and artifacts-free data. [14]

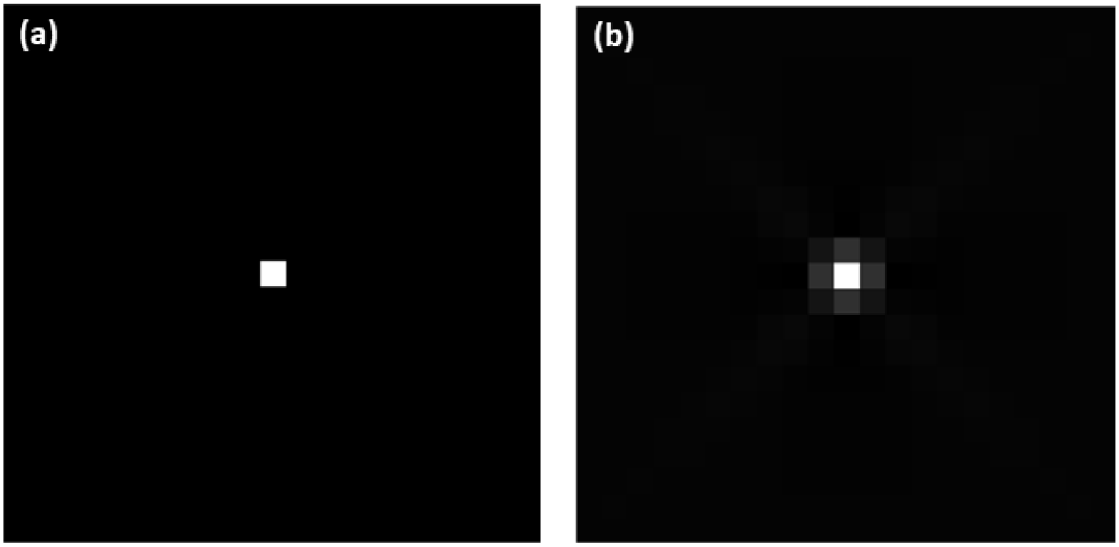


*Figure 3: Comparison of responses to Dirac impulse by ideal reconstruction system and real reconstruction system (used filter with best results for this phantom – Hamming filter with cut-off point = 1.8): a) Ideal reconstruction system and b) real reconstruction system. [14]*

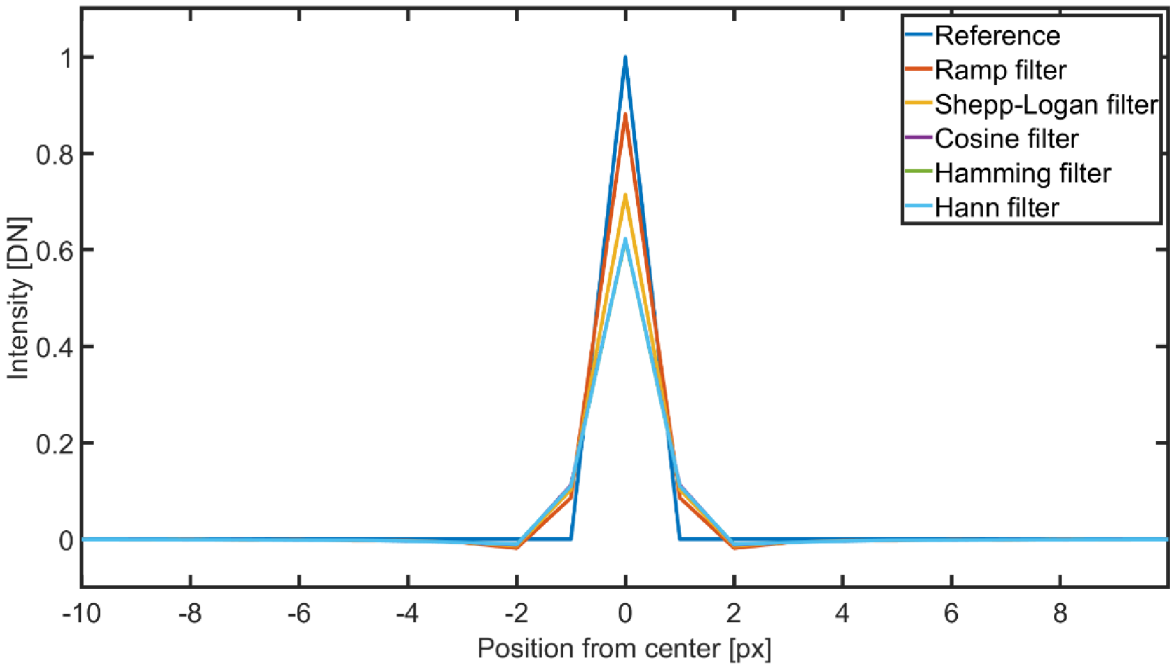


*Figure 4: Line profiles in horizontal directions over central area of Dirac impulse tomograms reconstructed with filtration settings that achieved best results for this phantom. [14]*

*Table 4: Overall optimal filtration settings for ideal data. [14]*

| Rank | Filter type | Cut-off point |
|---|---|---|
| **1.** | Cosine | 2.0 |
| **2.** | Hann | 2.8 |
| **3.** | Shepp-Logan | 1.1 |
| **4.** | Hamming | 2.7 |
| **5.** | Ramp | 1.0 |

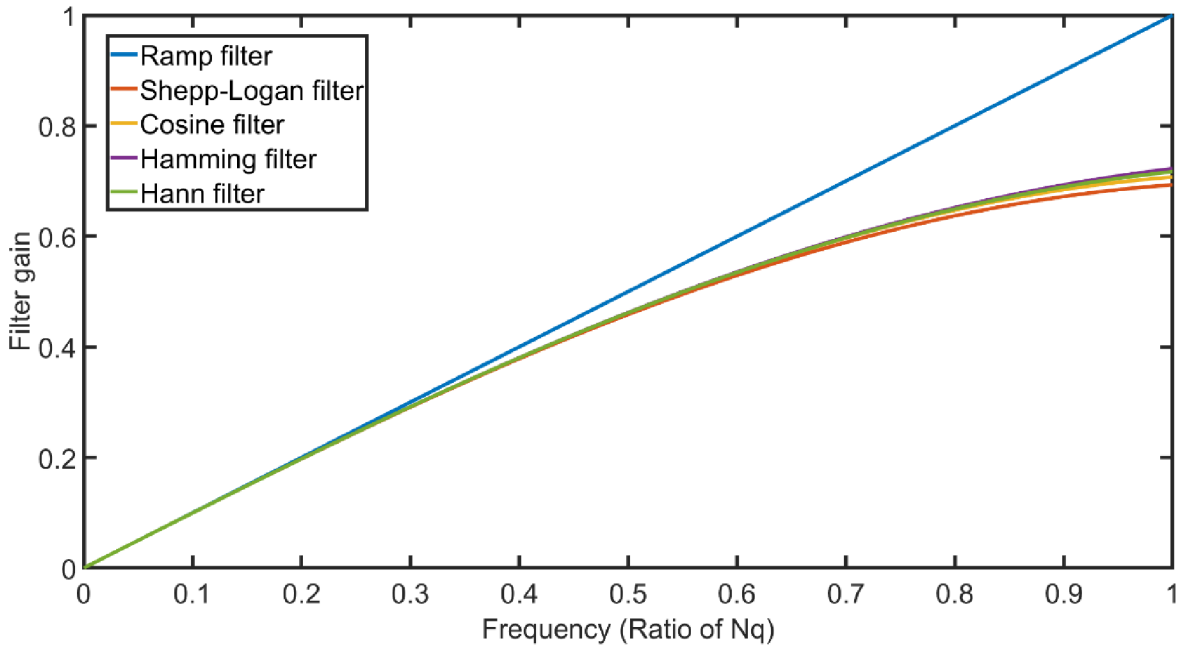


*Figure 5: Transmission functions in frequency domain of estimated optimal filtrations settings for ideal data. [14]*

### *3.1.2.2 Spatial resolution dependence on used reconstruction settings*

Using spatial resolution phantom, the effect of used cup-off point on achieved spatial resolution was studied. As filter type, the cosine filter was used due to its best overall results in previous section. This analysis was done using line profiles analysis over the chart-pattern (see Figure 6) covering the resolution areas from 4.0 µm to 0.5 µm. The assumption that with higher values of cut-off point the achieved spatial resolution increases, was confirmed. But it was found out that for used cosine filter the spatial resolution improvements were not significant from the cut-off point value 1.2. Even with the cut-off point 0.9 the highest tested resolution 0.5 µm was achieved. [14]

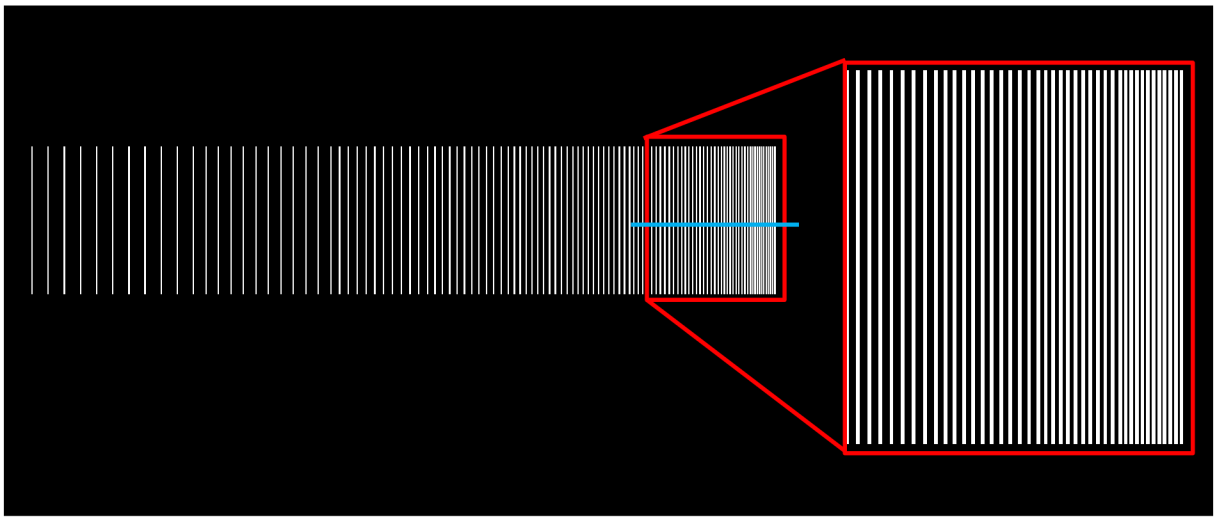

*a) Chart pattern of used spatial resolution phantom, by blue color is labeled the area used for line profile analysis: 4.0 µm – 0.5 µm.*

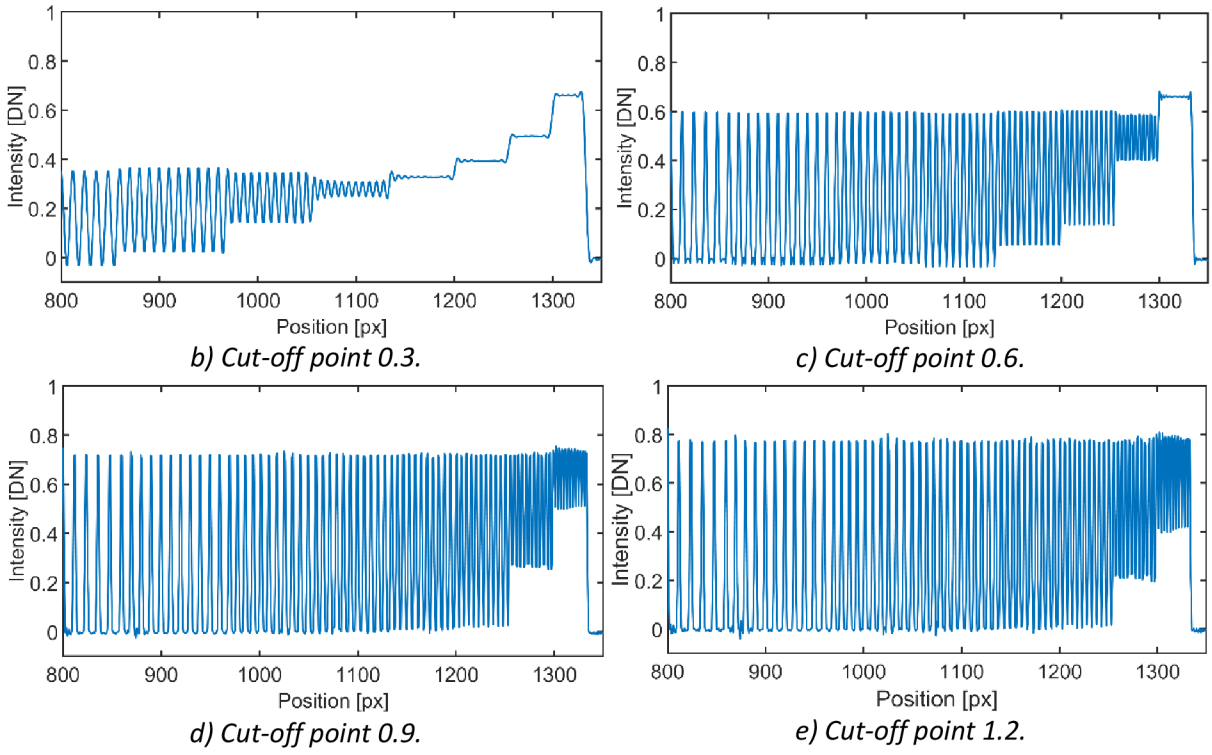


*b) Cut-off point 0.3.* *c) Cut-off point 0.6.*

*d) Cut-off point 0.9.* *e) Cut-off point 1.2.*

*Figure 6: Dependence of achieved spatial resolution on used cut-off point value for Cosine filter. [14]*

### *3.1.2.3 SNR dependence on used reconstruction settings*

For this study, Gaussian distributed noise with standard deviation 0.01 (reflects noise properties of real projection data) was added to sinograms of phantom images: circles phantom and spatial resolution phantom. For SNR calculation according to definition in section 2.3, the areas of signal and background were manually selected. The assumption, that with higher cut-off point values the SNR values decreases, was confirmed. The actual dependence of SNR on used filter type and used cut-off point

value is shown in Figure 7. This dependence was evaluated for filter types with best optimization score from previous study (3.1.2.1) and for cut-off point values from 0.1 to 5.0 with step 0.1. It was found out that this dependence has exponential course when the highest decrease of SNR values lies between cut-off points from 0.1 to 0.5 and that from cut-off point value 1.0 towards higher values this decrease is almost negligible. Overall best SNR results achieved the Hann, Hamming and cosine filters. However, it was found out that the first two named filters do not reach comparable resolution as cosine filter when having same SNR values. Specifically, it was found out that Hann or Hamming filters would need cut-off point values higher than 1.0 to achieve comparable spatial resolution as cosine filter with cut-off values less than 1.0. Therefore, cosine filter is selected as the optimal filter, in terms of acquired spatial resolution and noise reduction, with cut-off point values from 0.8 to 1.0. [14]

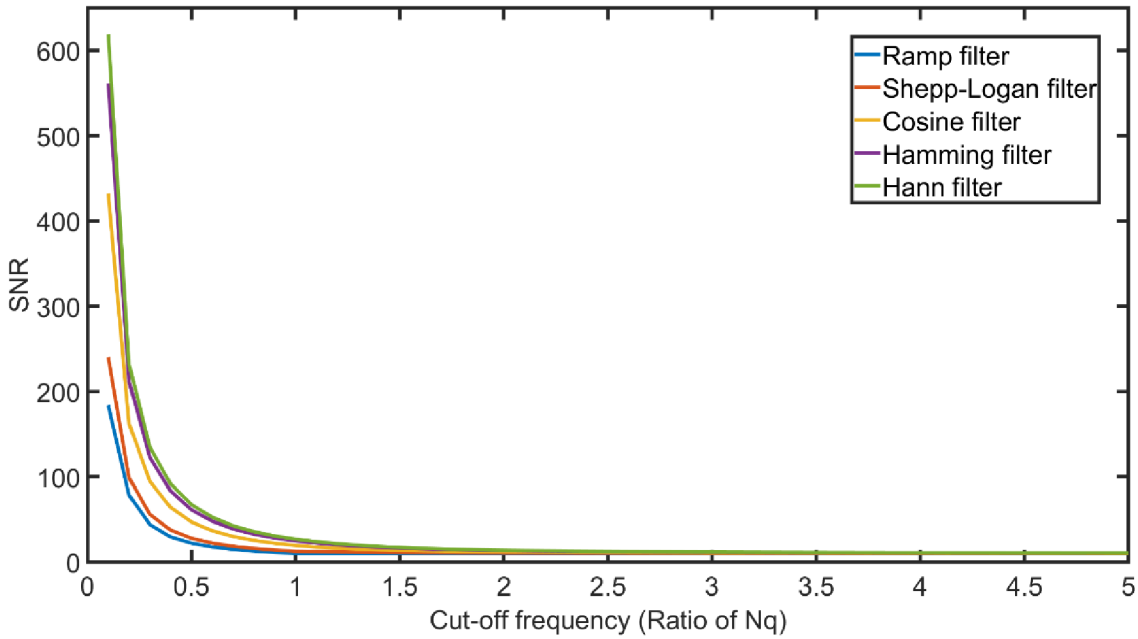


*Figure 7: Circles phantom – SNR dependence on used filter type and cut-off point value. [14]*

### 3.1.3 Summary

When dealing with FBP-based reconstruction of submicron CT data, there exists a compromise between the achieved spatial resolution and level of noise suppression during the reconstruction process. It was verified that Ram-Lak and Shepp-Logan filters do not provide optimal results for noisy data compared to the Hamming, Hann and Cosine filters that achieved the best results in terms of noise reduction. It is suggested that, for reconstruction of noisy projection data, the cut-off point should be selected less than 1.0 (< Nq) but not too low to preserve sufficient spatial resolution. In this interval the Cosine filter achieved the best results in terms of spatial resolution preservation compared to other filters. Therefore, Cosine filter is selected, and the optimal cut-off values interval is proposed to be 0.8 – 1.0, depending on data type and amount of noise. Such defined FBP reconstruction is further used within scope of this work. [14]

## 3.2 Practical assessment of detectors for submicron CT applications

The key component of any CT system is a detection system. Despite the technical development, the current detector's technology is still limited by various technical aspects that influence achievable spatial resolution of a CT system and overall quality of acquired data by presence of tomographic artifacts such as ring artifacts or noise. However, for their optimal reduction it is essential understand their cause and study their properties. In the sphere of submicron CT, the integrating detectors based on CCD or CMOS technology are predominantly used, when historically the CCD-based sensors were considered as golden standard in terms of achievable data quality. In this study, performance of three integrating detectors (one CCD- and two sCMOS-based) is conducted for laboratory-based submicron CT system Rigaku nano3DX to assess possibilities of current sCMOS technology. Properties of each detector were evaluated as well as the quality and noise properties of acquired data. Part of the results have been already presented at international conference, Industrial Computed Tomography (ICT 2019), for more details please refer to: [16].

### 3.2.1 Materials and methods

For purposes of this work Rigaku nano3DX was equipped with Rigaku's scientific X-ray CDD camera (XSight™ Micron LC X-ray CCD camera [17]), scientific X-ray sCMOS camera (XSight™ Micron LC X-ray sCMOS camera [18]) and Rigaku's prototype camera using sCMOS technology, these cameras were labelled as CCD, sCMOS1 and sCMO2 respectively. Summary of cameras' nominal parameters without an optical lens unit is listed below in Table 5.

*Table 5: Nominal parameters of tested cameras without an optical lens unit.*

| Technical features | CCD | sCMOS 1 | sCMOS 2 |
|---|---|---|---|
| Array size | 3320(H) x 2500(V) | 2048(H) x 2048(V) | 2560(H) x 2160(V) |
| Pixel size | 5.4 µm | 6.5 µm | 6.5 µm |
| Sensor diagonal | 22.5 mm | 18.8 mm | 21.8 mm |
| Nonlinearity | < 1% | <0.2% | <0.2% |
| Dynamic range | 2300: 1 | 21 400: 1 | 21 400: 1 |
| Acquisition gain | 0.45 e-/ADU | 0.52 $e^-$/ADU | 0.52 $e^-$/ADU |
| Readout noise | 11 e- rms | 1.4 $e^-$ rms | 1.4 $e^-$ rms |
| Readout rate | 8 Mpix./s (≈ 1 fps) | 40 fps (@ 16 bit) | 30 fps (@ 16 bit) |
| Dark current | 0.001 e-/pix./s -35ºC | 0.14 $e^-$/pix./s @ 0ºC | 0.0169 $e^-$/pix./s @ -10ºC |
| Binning | Independent on-chip binning in x, y | 2 x 2, 3 x 3, 4 x 4, 8 x 8 | 2 x 2, 3 x 3, 4 x 4, 8 x 8 |
| Peak quantum efficiency | 56% @ 540 nm | 82% @ 550 nm | 58% @ 550 nm |
| Shutter type | Electromechanical | Rolling shutter | Rolling shutter |
| Data interface | USB 2.0 | USB 3.0 | USB 3.0 |

For comparison of all tested cameras various data types were acquired which are stated in Table 6, with used acquisition settings and evaluated parameters – for more detail about evaluated parameters refer to Table 3. For measurements with CCD and sCMOS 1 camera, the sensors temperature was kept at 0 °C. For second tested sCMOS camera, the sensor temperature was set to -10 °C to evaluate effect of cooling on noise properties. Used exposure times for X-ray projection data were selected based on optimal contrast (dependent on amount of detected signal) and on intended

analysis purpose of the data. For comparison of all systems in terms of CT data acquisition, the exposure time was first selected for CCD camera based on optimal contrast and the exposure for sCMOS based cameras was subsequently derived to achieve equal detected signal level as for CCD. The evaluated CT data of a ruby ball (0.3 mm diameter) and a glass cup sample were reconstructed, from only background and flat-field corrected projections, using reconstruction settings specified in section 3.1. No data processing or corrections such as noise or ring artefacts reduction were used in our study. For some analysis DN (Digital numbers) of acquired data were converted to number of detected electrons using vendor's conversion specifications.

*Table 6: List of acquired data with corresponding acquisition parameters and evaluated parameters.*

| **Data** | **Acquisition parameters** | | | **Evaluated parameters** |
|---|---|---|---|---|
| | **CCD** | **sCMOS 1** | **sCMOS 2** | |
| Bias frames | Exposure: 10 ms; Binning: 1x1; Pixel size: 5.5 µm; Frames: 10 | Exposure: 10 ms; Binning: 1x1; Pixel size: 6.5 µm; Frames: 10 | Exposure: 10 ms; Binning: 1x1; Pixel size: 6.5 µm; Frames: 10 | Read-out noise |
| Dark background frames | Exposure: 1-30 s; Binning: 1x1; Pixel size: 5.5 µm; Frames: 30 | Exposure: 1-30 s; Binning: 1x1; Pixel size: 6.5 µm; Frames: 30 | Exposure: 1-30 s; Binning: 1x1; Pixel size: 6.5 µm; Frames: 30 | Dark current<br>Hot pixels<br>Random hot pixels |
| Bright frames | Target: Cu; Exposure: 1-30 s, 60 s; XD = 0.7 mm; Binning: 1x1; Pixel size: 0.27 µm; Frames: 30, 20 | Target: Cu; Exposure: 1-30 s, 30 s; XD = 0.7 mm; Binning: 1x1; Pixel size: 0.32 µm; Frames: 30, 20 | Target: Cu; Exposure: 1-30 s, 30 s; XD = 1.1 mm; Binning: 1x1; Pixel size: 0.32 µm; Frames: 30, 20 | Noise properties<br>Linearity |
| JIMA RT RC-02B frames | Target: Cu; Exposure: 30 s, 60 s; XD = 0.9 mm; Binning: 1x1; Pixel size: 0.27 µm; Frames: 10/ chart position | Target: Cu; Exposure: 30 s; XD = 0.7 mm; Binning: 1x1; Pixel size: 0.32 µm; Frames: 10/ chart position | Target: Cu; Exposure: 30 s; XD = 1.1 mm; Binning: 1x1; Pixel size: 0.32 µm; Frames: 10/ chart position | Spatial resolution<br>Data quality |
| CT data – Ruby ball (0.3 mm diameter) | Target: Mo; Exposure: 13 s; XD = 0.2 mm; Binning: 2x2; Voxel size: 0.53 µm; Projections: 802 | Target: Mo; Exposure: 4.5 s; XD = 0.2 mm; Binning: 2x2; Voxel size: 0.64 µm; Projections: 802 | Target: Mo; Exposure: 6 s; XD = 0.2 mm; Binning: 2x2; Voxel size: 0.64 µm; Projections: 802 | Spatial resolution<br>Data quality |
| CT data – Glass capillary* | Target: Mo; Exposure: 16 s; XD = 0.2 mm; Binning: 2x2; Voxel size: 0.53 µm; Projections: 802 | Target: Mo; Exposure: 6 s; XD = 0.2 mm; Binning: 2x2; Voxel size: 0.64 µm; Projections: 802 | Target: Mo; Exposure: 8 s; XD = 0.4 mm; Binning: 2x2; Voxel size: 0.64 µm; Projections: 802 | Data quality |

** For sCMOS 2 CT measurement not the same sample as for CCD and sCMOS 1 was used – only same structure.*

### 3.2.2 Results

#### *3.2.2.1 Noise properties analysis*

Numerical results of conducted noise properties analysis are presented in Table 7. It is evident that CCD camera poses higher readout noise and also the dark current compared to sCMOS 1, when cooling both sensors to 0 °C. Second tested sCMOS camera had slightly higher readout noise than sCMOS 1, but much lower dark current compared to both other tested cameras, confirming the thermal dependence of dark current noise. Both tested sCMOS cameras had higher total noise than CCD camera which is evident from numerical results and also from both 1D and 2D normalized noise power spectra (Figure 8 and Figure 9). Specifically, in 2D total noise NNPS are evident high intensity crosses (Figure 9) for tested sCMOS cameras. The worst hot pixels and random hot pixels results achieved sCMOS 1, contrary to sCMOS 2 achieved the best hot pixels results which again reflects the positive effect of cooling.

*Table 7: Results of noise properties analysis.*

| | **Readout noise [e⁻ rms]** | **Dark current [e⁻/pix/s]** | **Total noise [e⁻ rms]** | **Hot pixels [%]** | **Random hot pixels [% / frame]** |
|---|---|---|---|---|---|
| CCD | 10.67 | 0.102 | 101.53 | 0.06 | 0.24 |
| sCMOS 1 | 1.32 | 0.057 | 118.75 | 0.47 | 0.74 |
| sCMOS 2 | 1.35 | 0.007 | 103.68 | 0.04 | 0.73 |

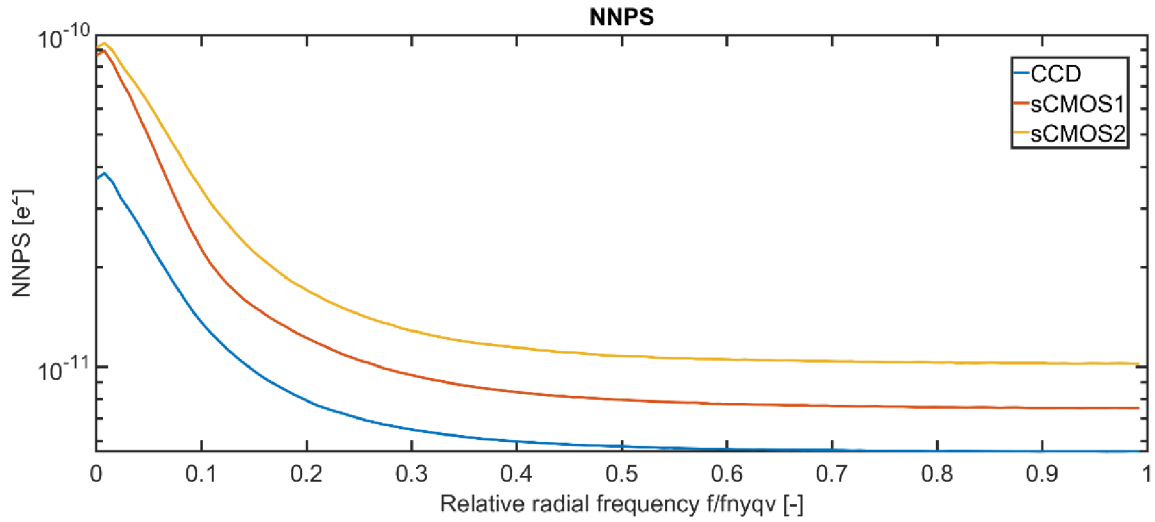

Figure 1

*Figure 8: Comparison of 1D NNPS for all tested cameras.*

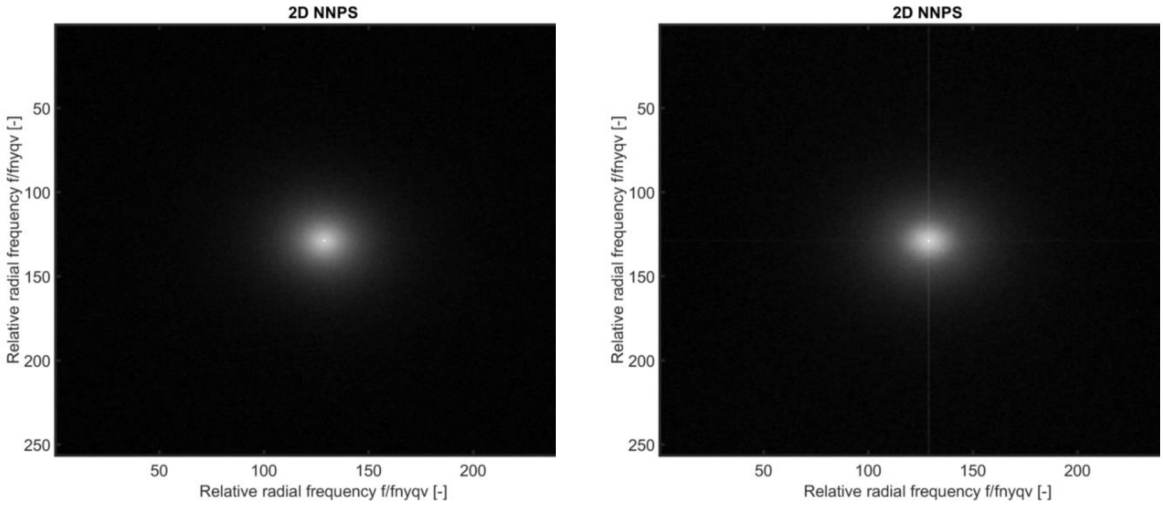


*a) CCD* *b) sCMOS 1*

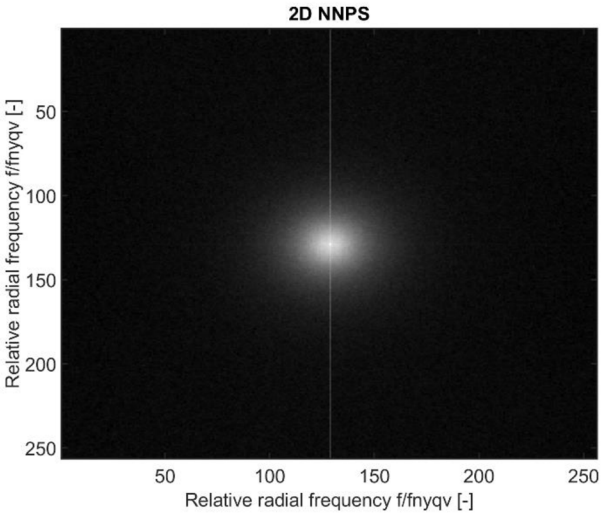


*c) sCMOS 2*

*Figure 9: 2D NNPS for all tested cameras.*

### *3.2.2.2 Spatial resolution analysis*

Achievable spatial resolution of Rigaku nano3DX system was evaluated for all tested cameras in both projection and tomogram domain using JIMA RT RC-02B resolution test and MTF analysis (defined in section 2.3). It was revealed that in projection domain and the system was able to reach 0.5 µm resolution in both horizontal and vertical directions for all tested cameras. In case of CCD camera, the resolution was comparable in both spatial direction (see Figure 10). However, in case of sCMOS cameras, it was revealed that the resolution was higher in horizontal direction (see Figure 10). The results of spatial resolution estimation in CT domain according to ASTM E1695-95 are stated in the Table 8. The best achievable spatial resolution was for CCD camera, which corresponds to its smallest voxel-size value and good data quality. Although, both sCMOS cameras had same voxel-size value, the sCMOS2 has worse achievable spatial resolution. This correspond to results of JIMA RT RC-02B resolution test (Figure 10), where is sCMOS 2 had blurrier line profile in vertical direction.

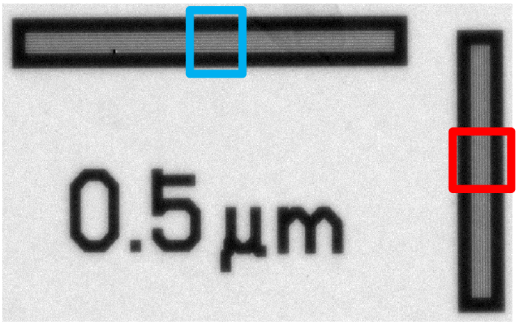


*a) CCD*

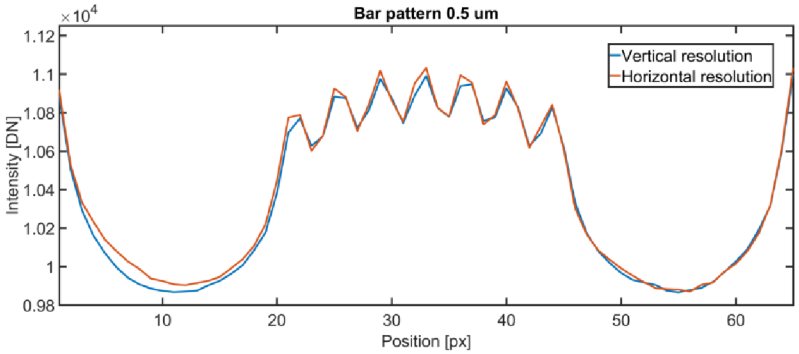


*b) CCD*

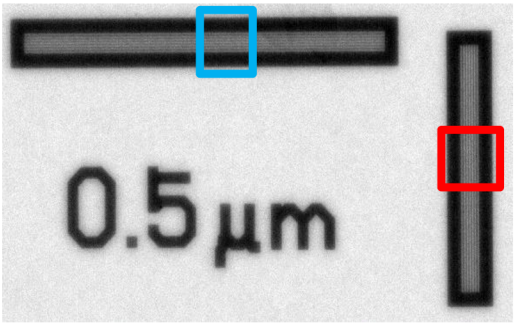


*c) sCMOS 1*

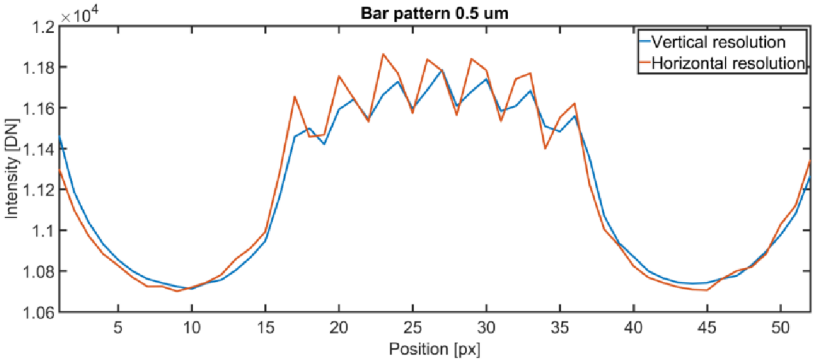


*d) sCMOS1*

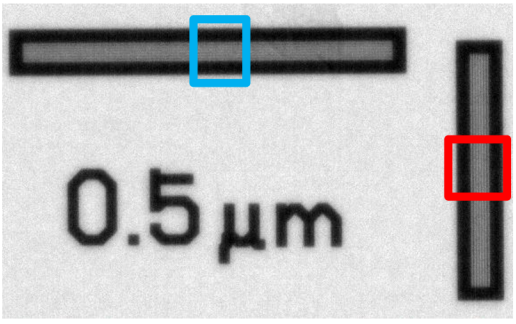


*e) sCMOS 2*

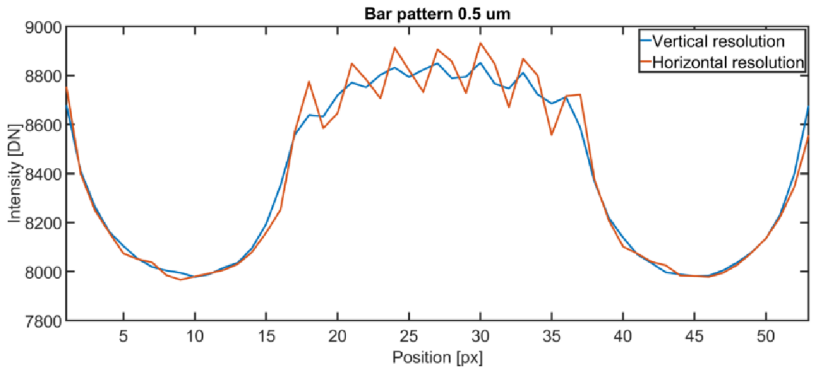


*d) sCMOS2*

*Figure 10: JIMA RT RC-02B resolution test: JIMA 0.5 µm chart; labelled areas were used for resolution line profile analysis.*

*Table 8:Results of MTF analysis*

| Camera | MTF 10 % level [lp/µm] | Spatial resolution [µm] |
|---|---|---|
| CCD | 0.307 | 0.863 |
| sCMOS1 | 0.342 | 0.933 |
| sCMOS2 | 0.286 | 1.115 |

### *3.2.2.3 Linearity analysis.*

Based on conducted linearity analysis, it was revealed that all cameras have responses linearly proportional to amount of incident photons (Figure 11). For all cameras the root mean square error (RMSE) of the distances between detected signal points and the linear fit was found to be negligible (Table 9).

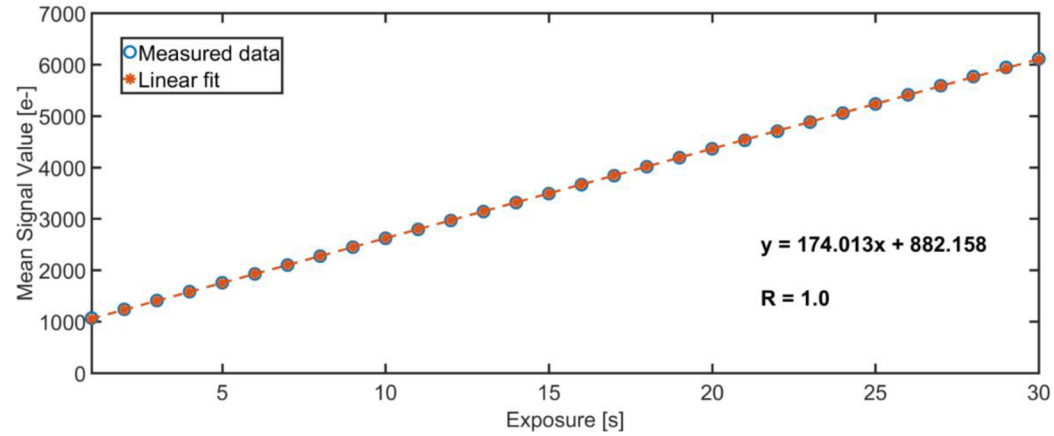


*a) CCD*

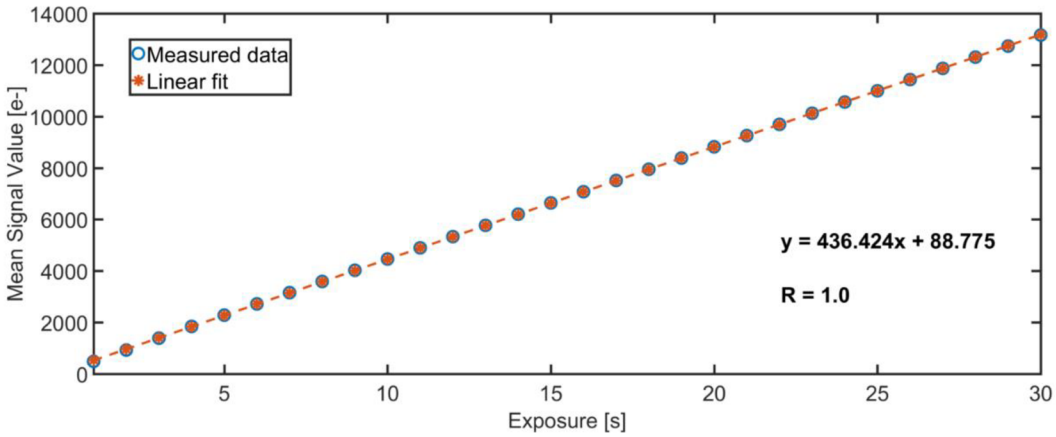


b) sCMOS1

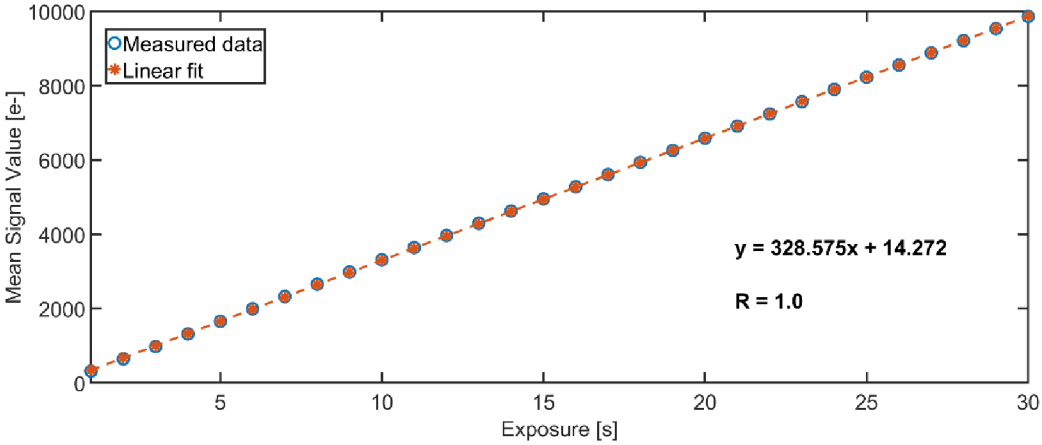


c) sCMOS2

*Figure 11: Bright-field frames linearity analysis.*

*Table 9: Results of linearity analysis – expressed as the root mean square of the distances between detected signal points and linear regression fit.*

| Camera | RMSE [%] |
|---|---|
| CCD | 9.93e-11 |
| sCMOS1 | 2.05e-10 |
| sCMOS2 | 7.22e-11 |

#### *3.2.2.4 Data quality*

Quality of acquired data was evaluated quantitatively and qualitatively. In projection domain, there were no significant data quality differences between all cameras except the vertical pattern that was visible in both sCMOS 1 and sCMOS 2 data (Figure 12). However, this pattern was visible only in central area of the projection images – detector rows covering sample area. This resulted to severe ring artifacts present in CT data acquired by tested sCMOS cameras (Figure 13). These artifacts were also present in CCD acquired data but not in such extent (Figure 13), which corresponds with results from hot pixels' analysis (Table 7). For quantitative evaluation six measures were calculated in both projection and tomogram domain and the results are presented in Table 10 and Table 11. For all evaluated data, the CCD camera reached higher SNR. Low SNR results in case of both rested sCMOS cameras can correspond to hot pixels population that could affect the analysis, specifically in tomogram domain (Table 11). In case of same exposure for all tested cameras (JIMA chart pattern), sCMOS 1 reached the best overall results compared to CCD and sCMOS 2, which corresponds to level of detected signal. Also, for situations, when comparable signal was detected by all tested sensors, sCMOS cameras reached better or comparable results to CCD camera.

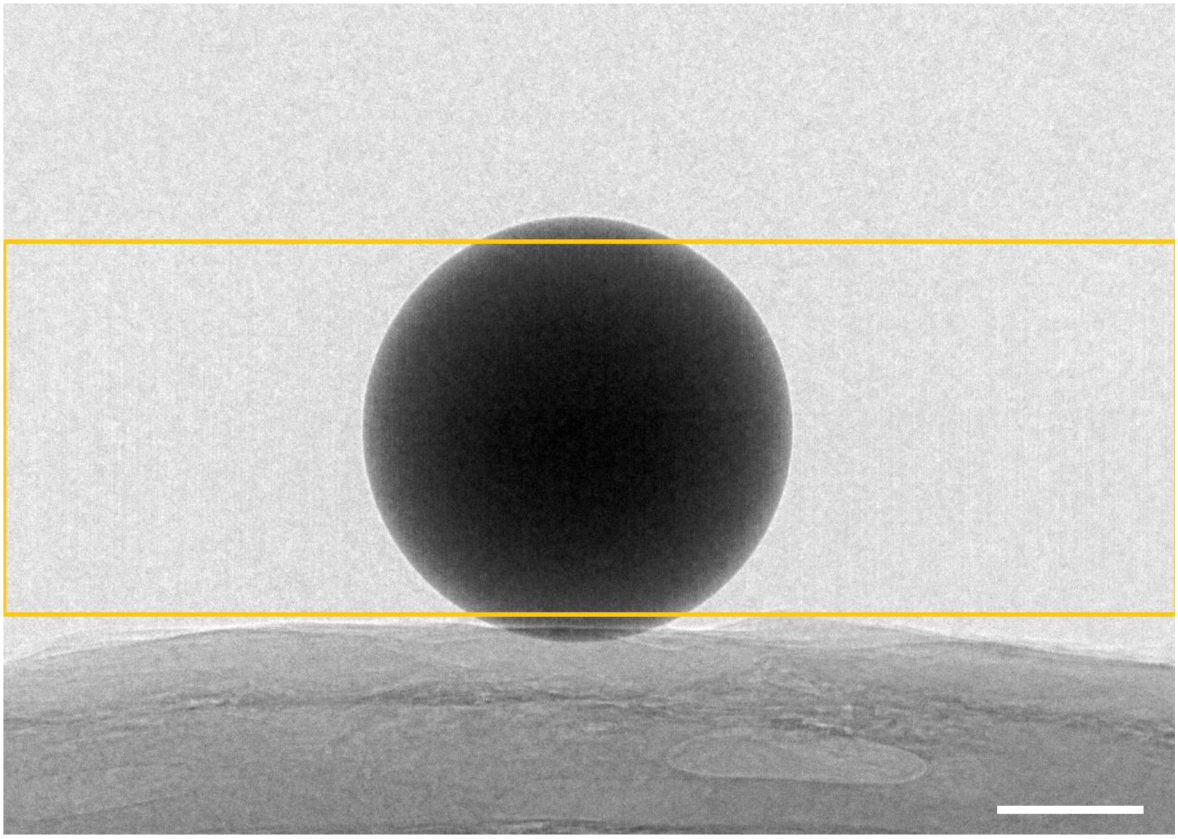

*Figure 12: Example of projection image of Ruby ball – acquired by sCMOS 2. The vertical pattern is visible in central area – labelled by yellow rectangle; scale bar: 100 µm.*

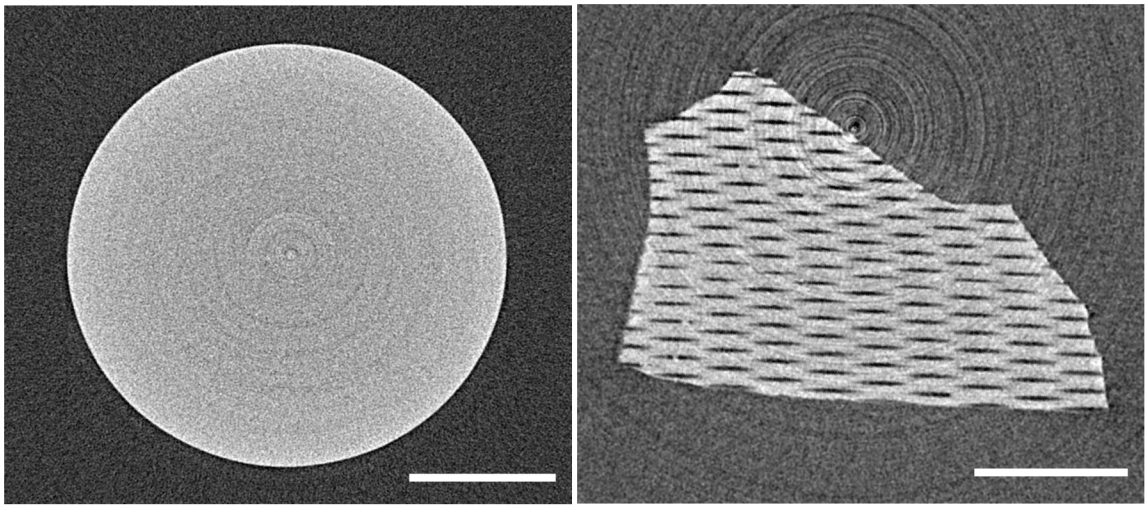

*a) Ruby ball – CCD* *b) Glass capillary – CCD*

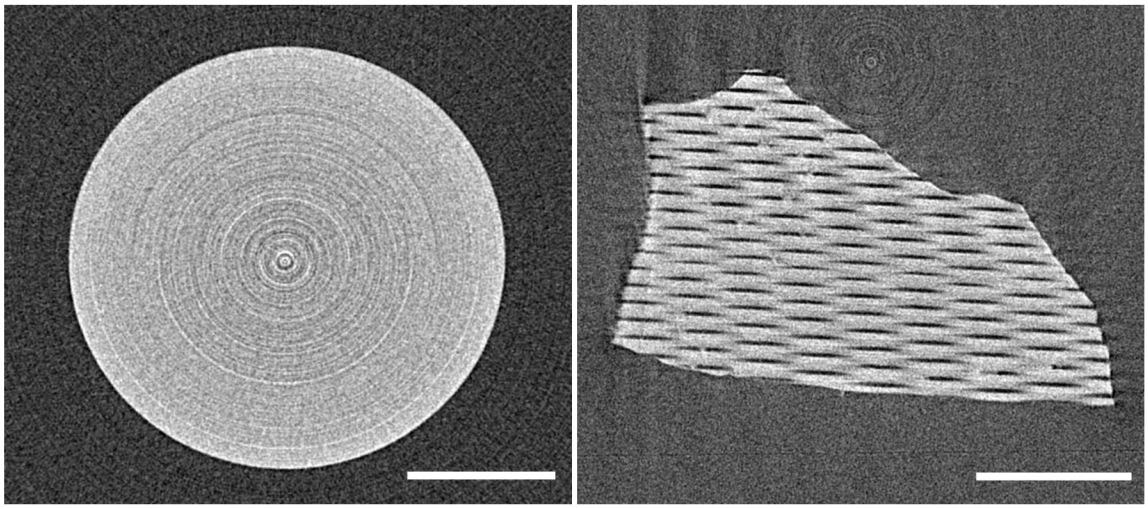

*c) Ruby ball – sCMOS 1* *d) Glass capillary – sCMOS 1*

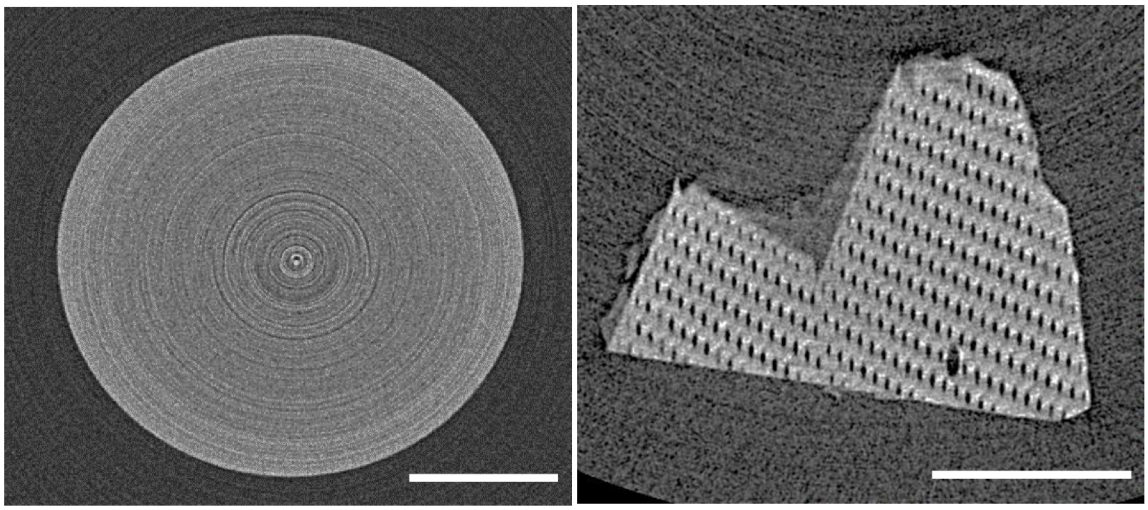

*e) Ruby ball – sCMOS 2* *f) Glass capillary – sCMOS 2*

*Figure 13: Comparison of raw CT images without any processing (no ring artifacts and noise reduction) acquired by tested cameras; central areas are shown; scale bar: 100 µm.*

*Table 10: Results of data quality analysis for acquired projection data.*

| | CCD | | | | sCMOS 1 | | | sCMOS 2 | | |
|---|---|---|---|---|---|---|---|---|---|---|
| | JIMA (30 s) | JIMA (60 s) | Ruby ball | Glass cap. | JIMA (30 s) | Ruby ball | Glass cap. | JIMA (30 s) | Ruby ball | Glass cap. |
| **CNR** | 7.07 | 10.15 | 28.83 | 28.80 | 10.51 | 17.75 | 25.52 | 10.20 | 21.20 | 27.30 |
| **SNR** | 8.73 | 9.10 | 3.53 | 51.0 | 6.89 | 3.17 | 9.60 | 4.26 | 3.99 | 15.97 |
| **C** | 0.56 | 0.61 | 1.0 | 0.14 | 0.72 | 1.0 | 0.48 | 0.88 | 1.00 | 0.53 |
| **VAR** | 3e-3 | 4e-3 | 1.85e-5 | 1.47e-4 | 0.01 | 1e-3 | 8.91e-4 | 2.7e-3 | 1.5e-3 | 4.4e-3 |
| **SML** | 184.76 | 185.48 | 381.94 | 280.53 | 164.25 | 3778.60 | 137.63 | 137.41 | 6303.33 | 162.45 |
| **JNB** | 1.39 | 2.61 | 0.98 | 2.09 | 3.20 | 0.63 | 2.75 | 2.51 | 0.81 | 3.08 |

*Table 11: Results of data quality analysis for tomographic data.*

| | CCD | | sCMOS 1 | | sCMOS 2 | |
|---|---|---|---|---|---|---|
| | Ruby ball | Glass cap. | Ruby ball | Glass cap. | Ruby ball | Glass cap. |
| **CNR** | 6.15 | 4.44 | 6.11 | 4.41 | 6.13 | 5.33 |
| **SNR** | 79.28 | 278.15 | 26.63 | 26.06 | 27.38 | 34.47 |
| **C** | 0.08 | 0.03 | 0.39 | 0.40 | 0.40 | 0.34 |
| **VAR** | 1.98e-4 | 1.03e-4 | 2e-3 | 0.01 | 1.4e-3 | 6.4e-3 |
| **SML** | 1158.71 | 106.31 | 1682.12 | 519.72 | 1754.90 | 187.52 |
| **JNB** | 7.89 | 4.52 | 6.94 | 5.13 | 11.94 | 16.22 |

### 3.2.3 Summary

In this study, comparison of CCD- and two sCMOS-based detectors in field of submicron CT was conducted using Rigaku nano3DX system. All detectors were compared in terms of their properties and also acquired data quality. For that, image data of phantoms as well as selected samples from material sciences were acquired and evaluated in projection and tomogram domain. Acquired results showed that there were not negligible differences between all tested cameras, specifically in terms of noise properties, achieved spatial resolution and number of hot pixels. However, it was shown that both sCMOS-based detection systems can be used for the task of submicron CT. Specifically, they had better quality and noise properties results for low exposure time measurement scenarios compared to situation when CCD sensor was used. Therefore, those detectors can be used for imaging of fast dynamic processes where it is crucial to keep the acquisition time as low as possible.

## 3.3 Noise reduction for submicron CT data

In this section work regarding noise reduction in the sphere of submicron CT is presented and summarized. First, noise properties were studied and then several algorithms were tested for reduction of all noise compounds found in the data. All acquired knowledge was then used for proposal of optimal noise reduction procedure in 3D projection data acquired by means of submicron CT system Rigaku nano3DX using XSight™ Micron LC X-ray CCD camera [17]. Part of the results have been already presented in form of a poster at 12th International Conference on Computer Graphics, Visualization, Computer Vision and Image Processing (CGVCVIP 2018) in Madrid, Spain: [19]. [14]

### 3.3.1 Noise model

Results regarding noise properties from previous study (3.2.2.1) were used and further extended. Here, the focus was placed on estimating a noise distribution model which is an essential parameter for optimal noise reduction. First, the total noise was extracted from set of bright-field frames (acquisition parameters are specified in Table 6) by subtraction of an average bright-field frame from intensity stabilized frames. Such extracted noise was further analysed using normal probability plot analysis (Figure 14). It was revealed that two main components can be separated from the extracted total noise: one following Gaussian distribution (Shot noise) and the second outside this distribution with values around borders of used intensity dynamic range (classified as random valued impulse noise). The first and major noise component (in terms of number of affected pixels) was further analysed to confirm its distribution (Figure 15), when the actual distribution of this component was compared to reference Gaussian distribution having the same characteristics, i.e. mean value and variance. [14]

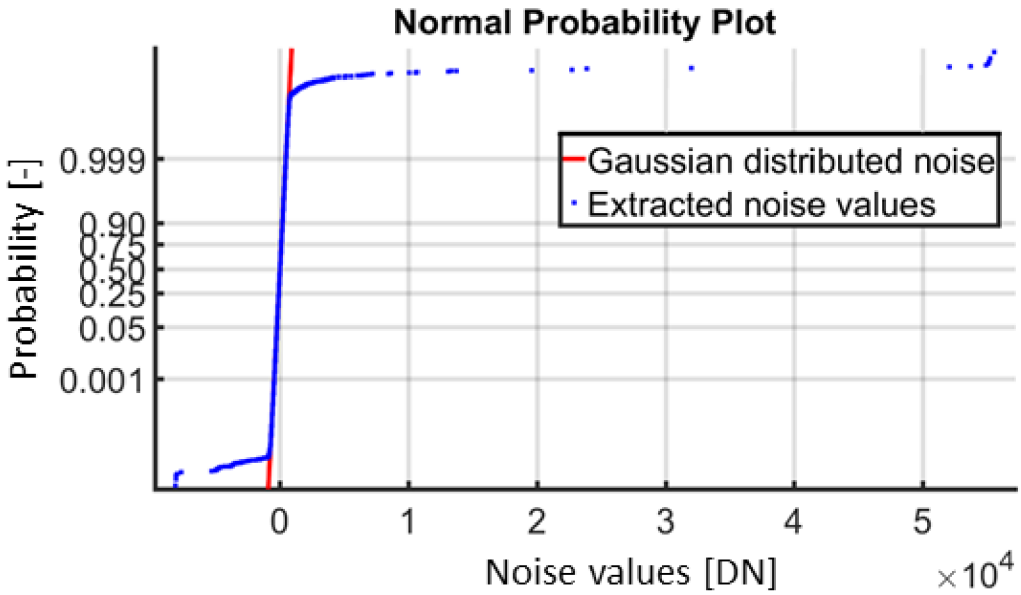


*Figure 14: Normal probability plot analysis of extracted total noise. [14]*

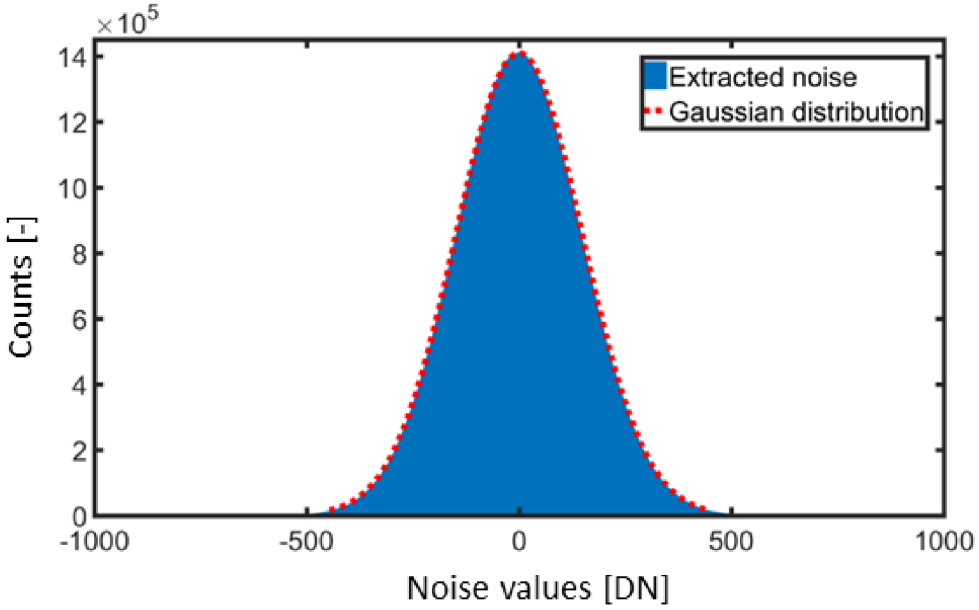


*Figure 15: Comparison of shot noise distribution with reference Gaussian distribution having the same characteristics, i.e., mean value and variance. [14]*

### 3.3.2 Proposed algorithm for estimation of noise absolute deviation

As beforehand mentioned, exact noise characteristics are essential for optimal noise reduction. Specifically, in case of Gaussian distributed noise, most denoising algorithms sets their parameters based on standard deviation of noise present in data. In this work, new algorithm was proposed for exact noise absolute deviation estimation. This algorithm is based on Imearkear method [20] and inspired by its modification published by Tai [21]. [14]

In original algorithm noise variance is calculated as weighted average of convolution result of input image with 2D kernel:

$$N = \begin{bmatrix} 1 & -2 & 1 \\ -2 & 4 & -2 \\ 1 & -2 & 1 \end{bmatrix}. \tag{3-1}$$

This kernel was derived to be insensitive to the Laplacian of an image. However, it was revealed that this assumption is not always fulfilled. Especially in highly textured images, thin lines and other small structures can be perceived as noise, resulting in noise over-estimation. Therefore, Tai in his work [21] proposed to first perform edge detection using Sobel operator and then follow Imearkear approach [20], but exclude detected edge pixels from variance calculation. However, it was found that even this modification is not sufficient for highly textured images with low levels of noise, where the noise standard deviation was in many cases overestimated. [14]

Our proposed approach was inspired by Tai's method [21], but different edges and structures detection approach is used. These features are detected using local standard deviation calculation followed by global thresholding with automatic threshold selection based on statistical evaluation. Specifically, as edge pixels are considered the pixels with high local standard deviation values. Using

this detection approach all structural pixels can be precisely identified and then excluded from absolute deviation calculation using the formula:

$$\sigma = \sqrt{\frac{\pi}{2}} \frac{1}{6 \sum (1 - G)} \sum |(I(x, y) * N)(1 - G)|, \tag{3-2}$$

where *I(x,y)* is the input image at spatial coordinates *x,y*; *N* is the convolution kernel described by equation (3-2) and *G* is result of edge and remaining structures detection. [14]

#### *3.3.2.1 Results*

Functionality of proposed algorithm was tested using Shepp-Logan phantom with several levels of Gaussian distributed noise added to its original values. For this analysis, the input data were normalized to intensity range from 0 to 1. Results were also compared to previously mentioned methods and stated in Table 12. The proposed algorithm achieved superior results for low levels of noise and in total reached the minimal overall deviation to reference standard deviation values compared to the other tested methods. [14]

*Table 12: Comparison of noise estimation methods. [14]*

| **Reference value** $\sigma_{ref}$ | **Immerkear** $\sigma$ | **Tai** $\sigma$ | **Proposed method** $\sigma$ |
|---|---|---|---|
| 0.0 | 0.002 | 0.001 | 0.000 |
| 0.001 | 0.003 | 0.002 | 0.001 |
| 0.005 | 0.007 | 0.006 | 0.005 |
| 0.01 | 0.012 | 0.011 | 0.010 |
| 0.05 | 0.051 | 0.051 | 0.050 |
| 0.1 | 0.101 | 0.101 | 0.100 |
| 0.25 | 0.251 | 0.250 | 0.250 |
| 0.5 | 0.501 | 0.501 | 0.501 |
| 0.75 | 0.750 | 0.750 | 0.750 |
| 1.0 | 1.003 | 1.003 | 1.003 |
| $\sum \lvert \sigma_{ref} - \sigma \rvert$ | **0.014** | **0.010** | **0.004** |

### 3.3.3 Proposed algorithm for impulse noise reduction

Median filter [22] has been widely accepted as solution for impulse noise reduction with high computational efficiency while on the other hand leading to blur and certain loss of information. Therefore, modified versions of it have been till now developed to overcome these drawbacks: adaptive median filter [23; 24; 25], weighted median filter [26; 27], decision based median filter [28; 29], fuzzy median filters [30; 31; 32] or switching median filters [33; 34; 35]. However, till today not fully acceptable and universal solution exists for the submicron CT data. In this work, new impulse noise reduction algorithm was proposed specifically for such data.

This algorithm is a switching median filter, having the first step noise affected pixels detection and followed by correction of those pixels in second step. Detection of affected pixels is based on a local image statistic called ROAD ("Rank-Ordered Absolute Differences") published by Garnett [34]:

$$ROAD_m(x) = \sum_{i=1}^{m} r_i(x), \tag{3-3}$$

where $r_i$ is the $i^{th}$ smallest absolute intensity difference of the pixels in squared shaped neighbourhood around the pixel *x*, when in the original work is recommended to use $m = 4$. The ROAD statistic provides a measure of how close a pixel value is to its four most similar neighbours, when the unwanted impulses will vary greatly in intensity from most or all of their neighbouring pixels, whereas most pixels composing the actual image should have at least half of their neighbouring pixels of similar intensity, even pixels on an edge [34]. To further improve identification of impulse noise affected pixels, it is proposed to calculate ROAD values for both original image and for median filtered image and subtract results from each other, further followed applying the log function on the result. This leads to suppression of negative structural effect and to amplification of differences between affected pixels with small dissimilarity and non-affected pixels in their neighbourhood.

As noise-affected pixels are subsequently identified those pixels which achieved statistically significant high dissimilarity values:

$$g(x,y) = \begin{cases} 1, & if\ f(x,y) \geq \bar{f} + 2 \cdot \sigma_f \\ 0, & if\ f(x,y) < \bar{f} + 2 \cdot \sigma_f \end{cases} \tag{3-4}$$

where *f(x,y)* is the input log transformed subtraction result of ROAD statistics from original and median filtered data and the threshold value to corresponds to sum of mean value and twice the standard deviation of the input *f* and *g(x,y)* is binary value of output binary image g both at corresponding spatial coordinates x, y. For correction, the detected noise pixels ($g(x,y) = 1$) are replaced by values from median filtered image from corresponding coordinates *x*,*y*. This replacement strategy is proposed to achieve good computational effectivity.

#### *3.3.3.1 Results*

For practical testing of proposed algorithm Lenna test image was used due to its sufficient structural complexity. Random valued impulse noise was added to this image, where its values were generated randomly around borders of used dynamic range and the affected positions were also selected randomly to cover 5 % of all image pixels (see Figure 16). Proposed algorithm was tested and compared to other methods that are in practice used (standard median filter [22], Progressive switching median filter (PSMF) [33] and Noise adaptive fuzzy switching median filter (NAFSM) [32]). Their results were compared in terms of three selected metrics: the peak signal-to-noise ratio (PSNR), mean squared error (MSE) and structural similarity index [36], where the original noise unaffected Lenna test image is considered as reference. From the results, stated in Table 9, it is evident that proposed algorithm achieved best scores compared to other tested methods. For visual evaluation, the results of proposed algorithm are demonstrated in Figure 16 and Figure 17. Especially in Figure 17, the structural preserving capabilities of proposed algorithm are clearly visible compared to standard median filter. [14]

*Table 13: Comparison of selected methods for impulse noise reduction using Lenna image. [14]*

| Method | PSNR [dB] | MSE | SSIM |
|---|---|---|---|
| Median | 33.750 | 4.221 e-4 | 0.907 |
| PSMF | 43.736 | 4.243 e-5 | 0.995 |
| NAFSM | 24.592 | 0.004 | 0.645 |
| Proposed | 45.547 | 2.794 e-5 | 0.996 |

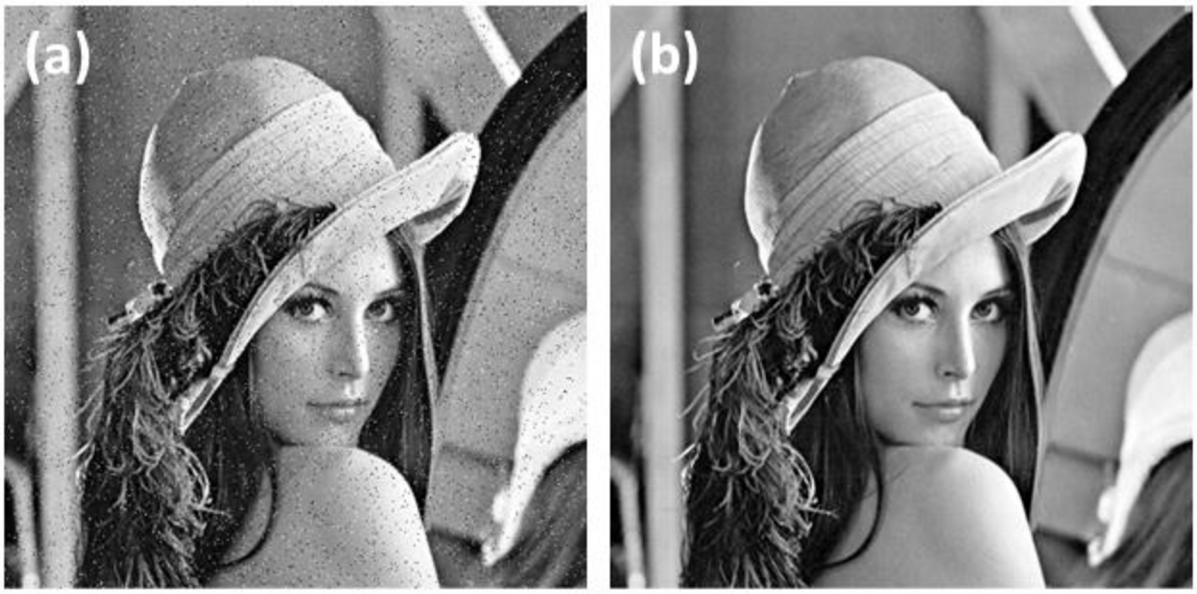


*Figure 16: Results of proposed impulse noise reduction algorithm demonstrated on the Lenna test image: a) input image; b) filtered image.*

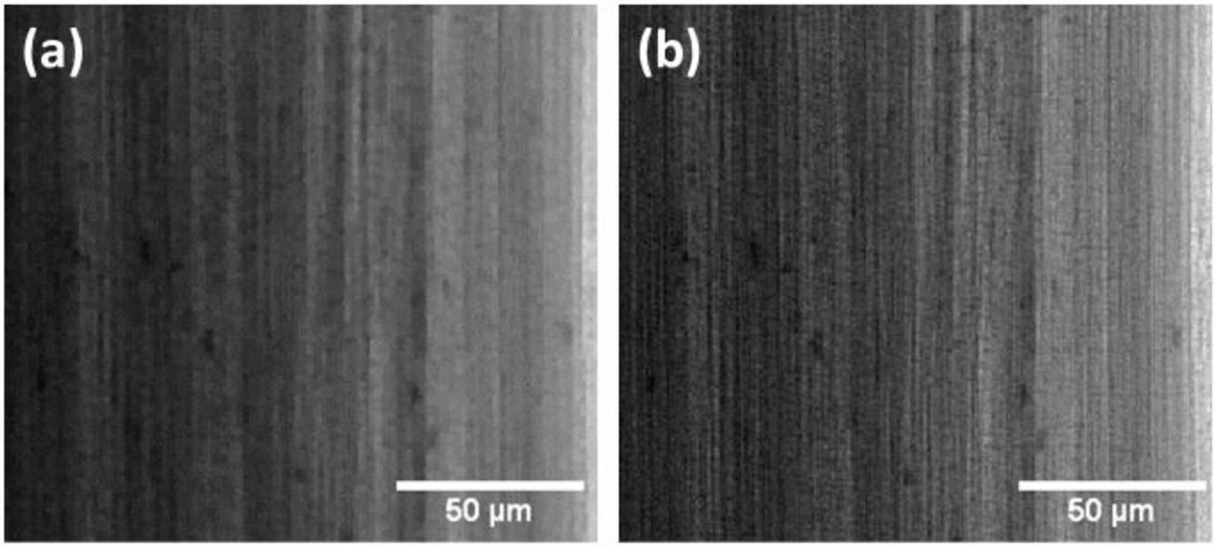


*Figure 17: Comparison of impulse noise reduction capabilities on real projection data: a) standard median filter; b) proposed filter. CT system: Rigaku nano3DX; Sample: bamboo stick. [19]*

### 3.3.4 Shot noise reduction

For reduction of shot noise, three algorithms were tested: 3D implementation of Gaussian filter [37], Non-Local-Means (NLM) filter optimized for 3D data [38] and Collaborative approach for enhanced denoising under low-light excitation (CANDLE) [39]. Those methods were specifically selected according to either their low computational cost (Gaussian) or reported superior results (NLM and CANDLE). Methods were tested both in projection and tomogram domain. In projection domain, the JIMA chart resolution pattern was used (data acquisition parameters are specified in Table 6). In tomogram domain, two types of samples were selected: single material sample of ruby ball (Lens unit: L1080, Binning: 2x2, Target: Mo, Exposure: 6 s, voxel size: 2.11 µm) and highly complex sample of Arabidopsis seedpod (Lens unit: L0270, Binning: 2x2, Target: Cu, Exposure: 28 s, voxel size: 0.53 µm). The evaluated CT data were reconstructed using reconstruction settings specified in section 3.1. For quantitative assessment, the achieved spatial resolution and data quality were selected as the evaluation metrics. Spatial resolution was evaluated both in projection and tomogram domain using JIMA RT RC-02B resolution test and MTF analysis (defined in Table 3). As data quality metrics, the SNR and CNR were selected. Specific settings of used methods were tuned according to visual perception of processed data or according to recommendations from original authors.

#### *3.3.4.1 Results*

In projection domain, the frame's averaging strategy (10 frames were used) was further incorporated and within the results evaluation considered as reference. Quality of denoising can be visually evaluated in Figure 18 but only minor differences are visible there for all tested methods. Such minor differences are also reflected by the line profile analysis presented in Figure 19 and data quality assessment in Table 14. In the quantitative evaluation (Table 14), the frame's averaging reached the worst results, which might correspond to number of averaged frames. On contrary, the Gaussian filter achieved the best numerical results. Table 14: Results of data quality analysis in projection domain.

*Table 14: Results of data quality analysis in projection domain.*

| | SNR | CNR |
|---|---|---|
| **Original** | 37.73 | 6.30 |
| **Averaging** | 89.16 | 16.39 |
| **Gaussian** | 109.47 | 23.26 |
| **NLM** | 104.72 | 20.40 |
| **CANDLE** | 103.58 | 21.52 |

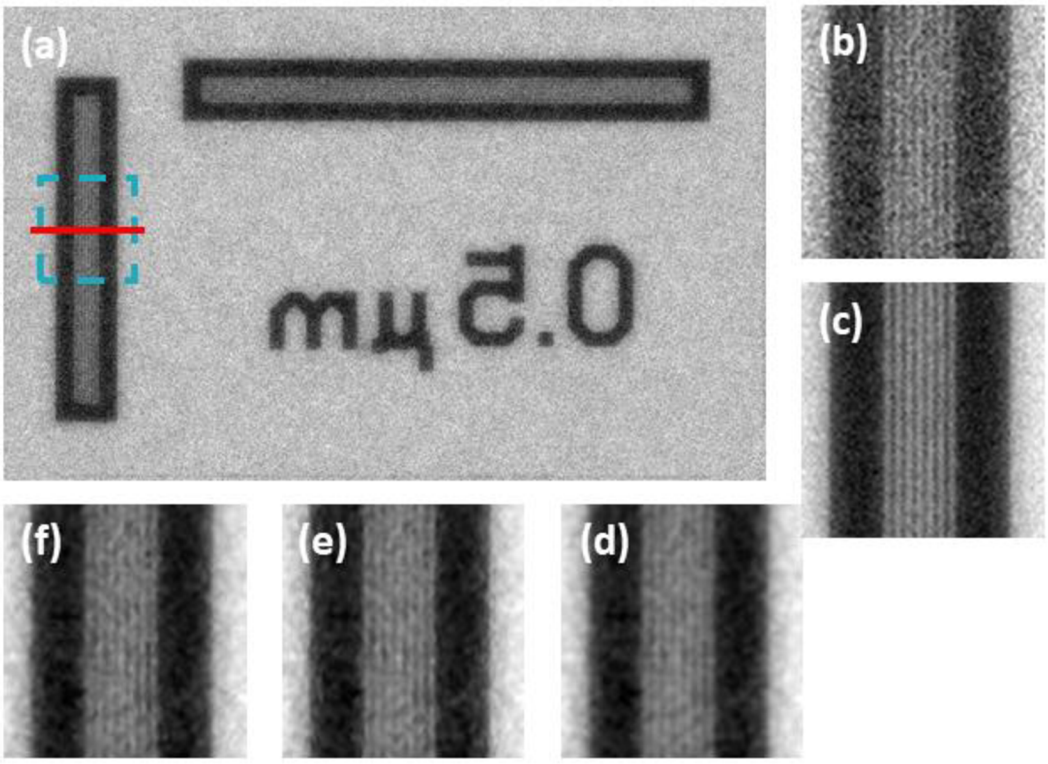


*Figure 18: Comparison of tested denoising methods in projection domain on JIMA RT RC-02B chart pattern: a) and b) original data; c) frames averaging; d) CANDLE; e) NLM and f) Gaussian. Red line indicates region assessed by line profile analysis.*

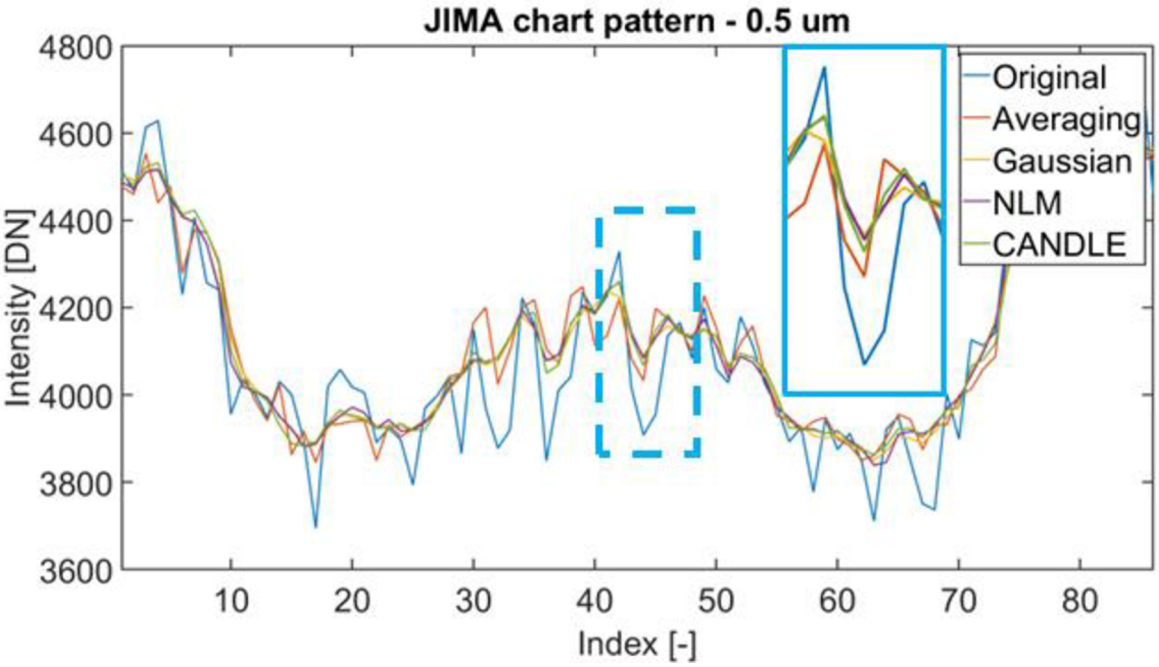


*Figure 19: Comparison of tested denoising methods in projection domain using JIMA RT RC-02B resolution test.*

In tomogram domain, the CANDLE algorithm achieved the best overall results, corresponding to its local adaptation for noise inhomogeneity and noise stabilization. This algorithm achieved unmatched smoothing and details preservation capabilities independent on sample's complexity (Figure 20 and Figure 21). This is further reflected by quantitative assessment (Table 15 and Table 16), where the spatial resolution preservation can be pointed out (Table 15). However, such high-quality results were balanced by high computational demands (Table 15 and Table 16). Therefore, it was concluded that depending on domain (i.e., projection or tomogram) specific algorithm should be used.

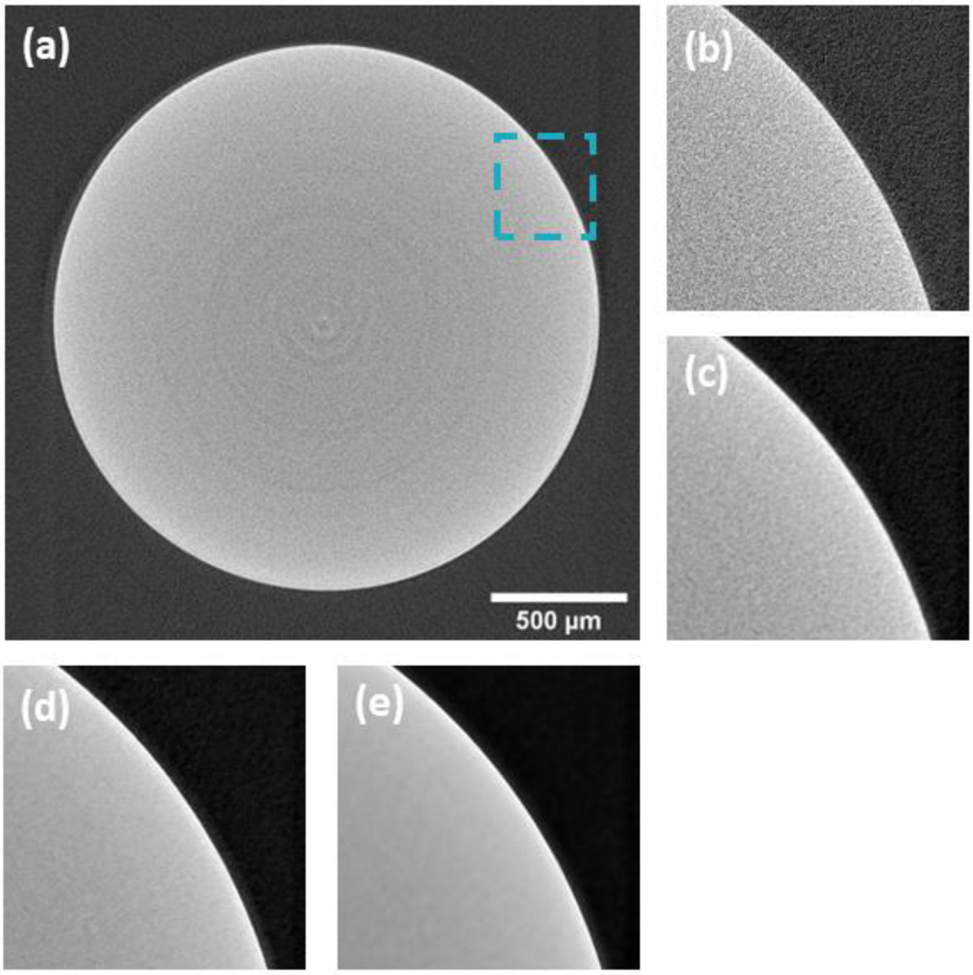


*Figure 20: Comparison of tested methods in tomogram domain on single material sample (ruby ball): a) and b) original; c) Gaussian; d) NLM and e) CANDLE.*

*Table 15: Results of data quality and spatial resolution analysis in tomogram domain for single material sample (ruby ball). The computational time (t) was evaluated for 1000 x 1000 x 11 data and on PC with Intel® Core™ i7-7800x, 3.55 GHz, 128 GB RAM.*

| | SNR | CNR | SR [µm] | t [s] |
|---|---|---|---|---|
| **Original** | 7.99 | 4.97 | 2.15 | - |
| **Gaussian** | 34.33 | 21.40 | 2.79 | 0.48 |
| **NLM** | 44.37 | 28.07 | 2.34 | 24.40 |
| **CANDLE** | 122.27 | 63.21 | 2.13 | 222.28 |

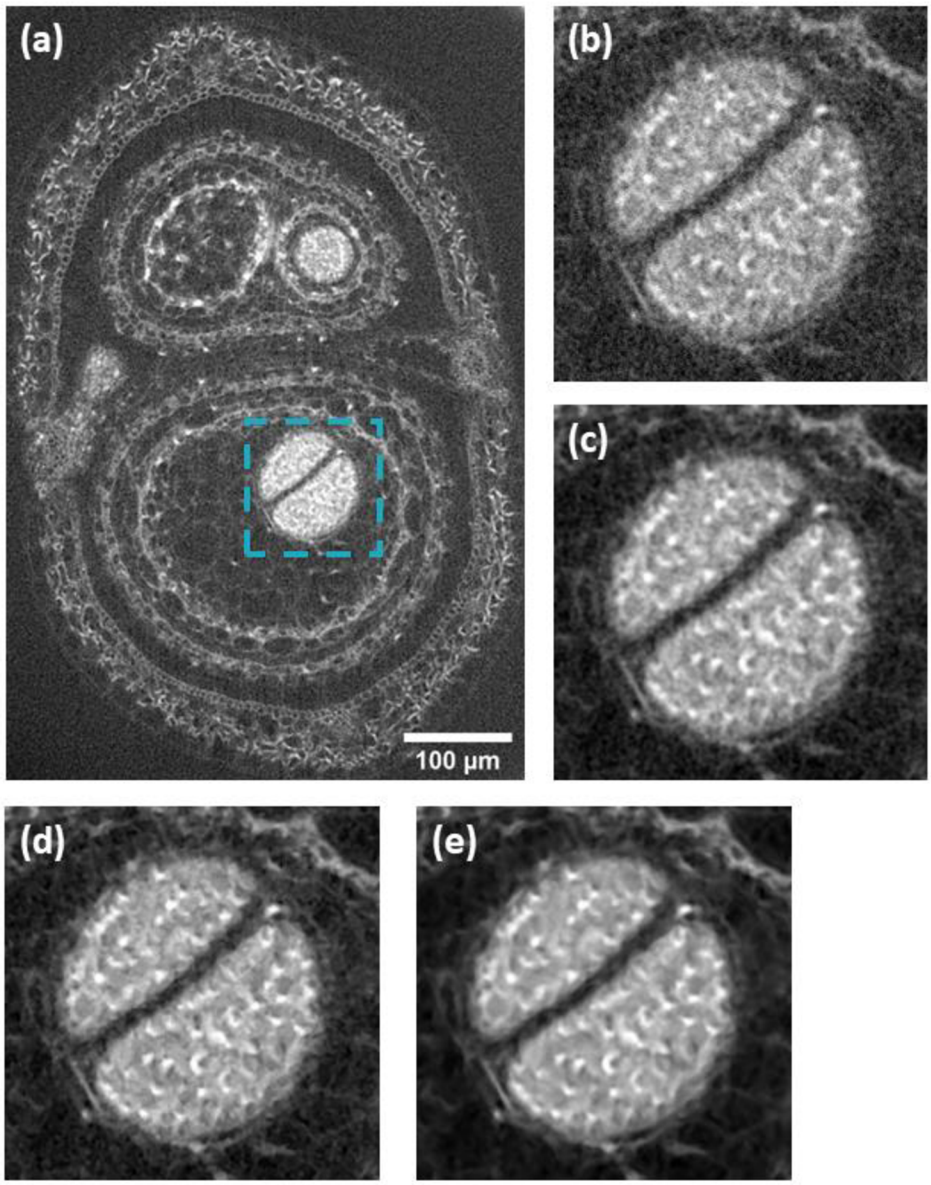


*Figure 21: Comparison of tested methods in tomogram domain on complex sample (Arabidopsis seedpod): a) and b) original; c) Gaussian; d) NLM and e) CANDLE.*

*Table 16: Results of data quality and analysis in tomogram domain for complex sample (Arabidopsis seedpod). The computational time (t) was evaluated for 1341 x 900 x 11 data and on PC with Intel® Core™ i7-7800x, 3.55 GHz, 128 GB RAM.*

| | SNR | CNR | t [s] |
|---|---|---|---|
| **Original** | 6.82 | 7.65 | - |
| **Gaussian** | 8.72 | 14.76 | 0.44 |
| **NLM** | 8.07 | 15.44 | 12.02 |
| **CANDLE** | 9.34 | 23.80 | 204.59 |

## 3.4 Ring artifacts reduction

CT data are often affected by severe ring arti-facts. They appear as concentric ring-like features superimposed on the imaged scene and are centred on the object's centre of rotation. Ring artifacts are mainly caused by imperfect detector pixels, where a perfect pixel's response should be linearly proportional to the amount of photons incident on the detector. There are many different underlying causes for individual pixels to have imperfect responses. These include defects in the scintillator, the detector itself, and the readout electronics. Moreover, the detector responses may vary due to numerous time-dependent drifts, such as thermal drifts, and also due to changes in the X-ray spectrum. No matter the cause, ring artifacts degrade the resulting image quality. Therefore, it is desirable to remove or at least significantly reduce the presence of ring arti-facts in CT data. However, in the field of submicron CT, the small size of detector pixels used in nano CT devices does not enable an application of any hardware-based method for removing ring artifacts, leaving image-based processing methods as the most promising way for an effective ring artifacts removal. Several approaches from this class exist, but each with some deficiencies, such as the degradation of data quality and spatial resolution, which is inconsistent with the core purpose of submicron CT. [40]

In the scope of this work, a new two-step ring artifacts reduction scheme was proposed that combines several selected ideas from image-based processing methods into one complex method with a goal to overcome their individual weaknesses and limitations. This procedure was developed for the artifacts' reduction in the sinogram domain and is based on a categorization of ring artifacts into two types. The ring artifacts are categorized based on the observation of responses from different kinds of deficiencies in sinograms and on their specific hardware causes (see Figure 22). In the proposed reduction scheme, each of these classes is then addressed separately using dedicated detection and reduction procedures. The novel iterative schemes based on relative total variations (RTV) [41] were integrated to detect the artifacts. The correction process uses the image inpainting, and the intensity deviations smoothing method. The reduction strategy was optimized for each artifact type separately to preserve the spatial resolution and sample's structural information, which are the most important factors in the field of submicron CT. Practical functionality of the prosed method was verified on both synthetic data and real CT data. It shows a high efficiency of ring artifacts removal, and a robustness to character of input data and used detection system in context of other tested ring artifacts correction techniques. The practical testing demonstrated that the proposed ring artifacts reduction procedure, compared to other methods (see Figure 23), can achieve superior results in the following criteria: artifacts detection accuracy, overall performance, robustness to detection system, and the ability to preserve the spatial resolution. In this section only the main features and results of this procedure are presented, for more details please refer to the published work [40] or Appendix section.

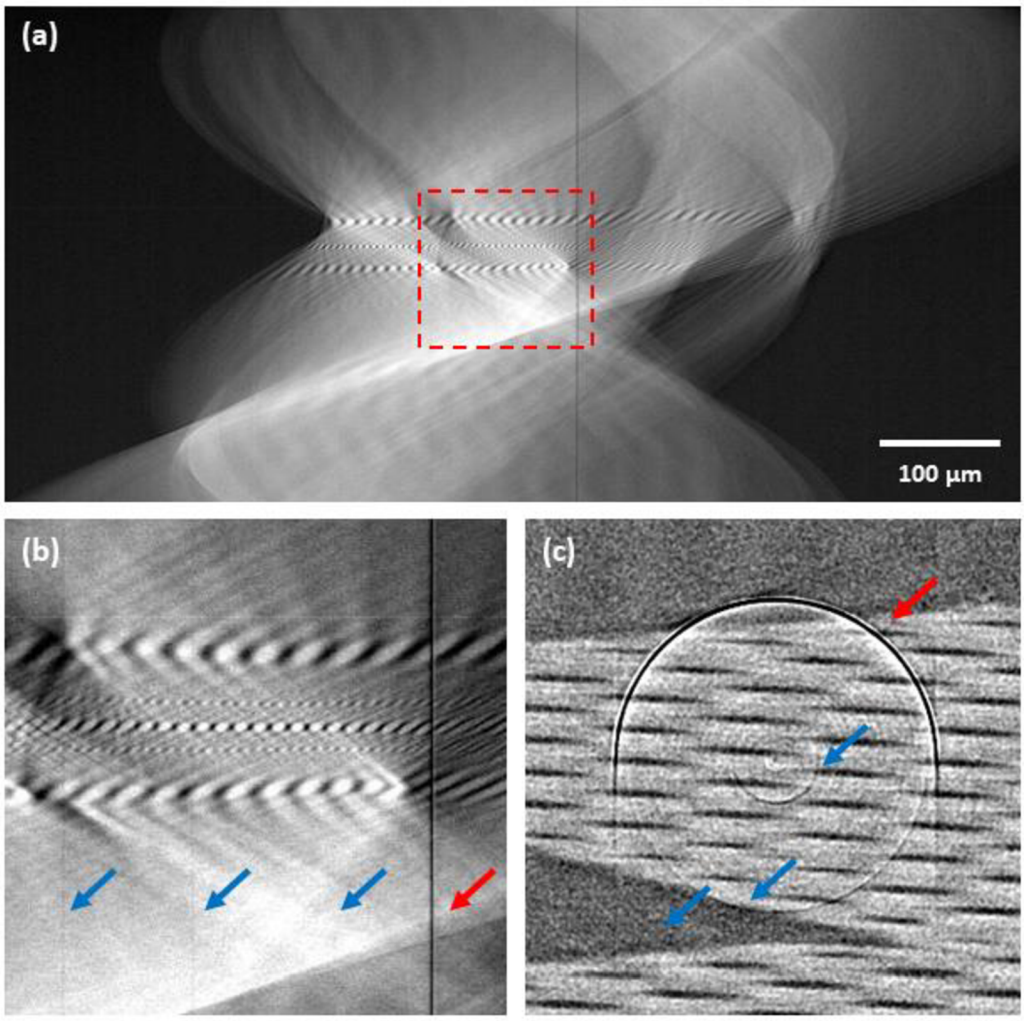


*Figure 22: Example of ring artifacts affected data with proposed classification scheme—glass capillary sample acquired with a charge-coupled device (CCD)-based camera: (a) sinogram; (b) detail of sinogram central area; (c) central area of corresponding tomogram. Red arrows indicate the high-level ring artifacts and blue arrows the low-level ring artifacts. [40]*

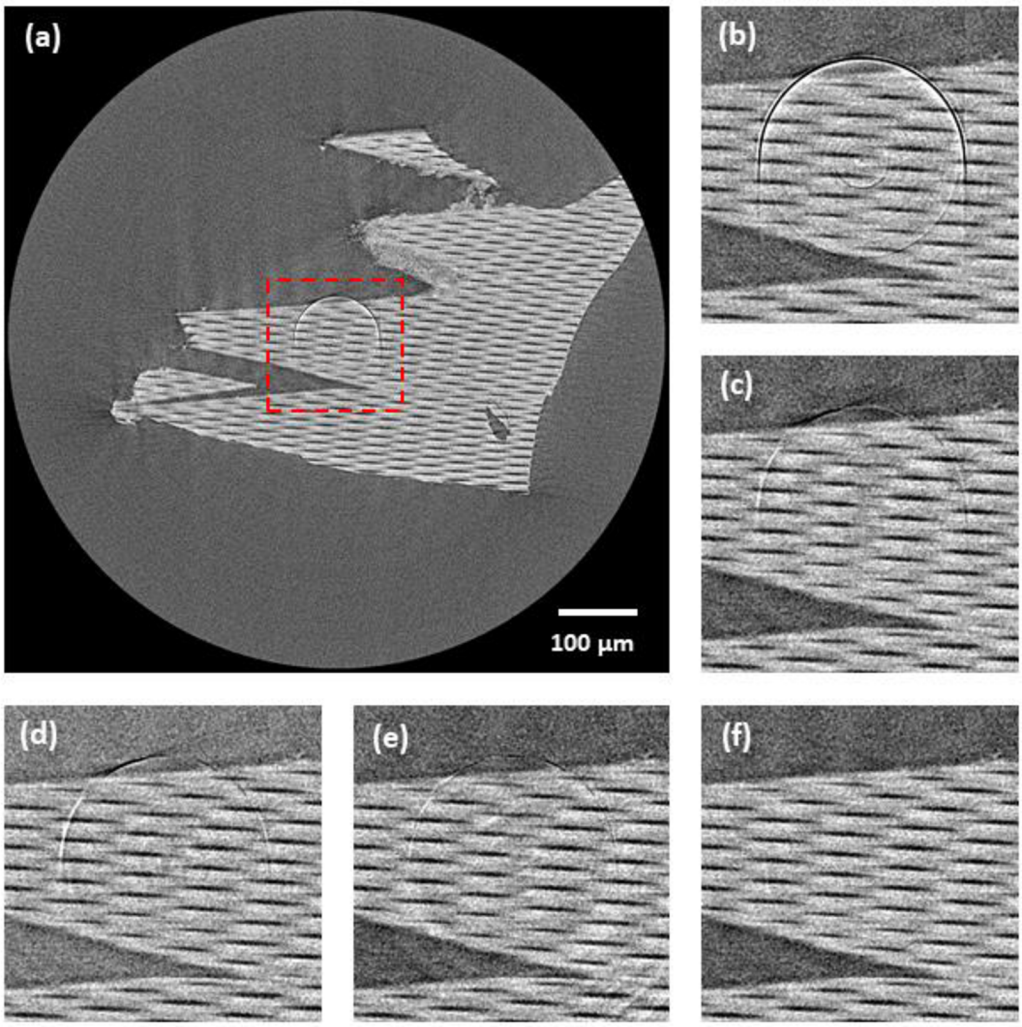


*Figure 23: Comparison of tomograms after ring artifacts reduction by tested methods—real computed tomography (CT) data of glass capillary array acquired with a CCD-based camera: (a) original tomogram (without any correction)—red labelled area marks central area visualized in following images; (b) original; (c) Münch [42]; (d) Eldib [43]; (e) Vo [44]; (f) proposed. For visualization, the same contrast setting was used for all the images. [40]*

## 3.5 Assessment and reduction of rotational stages limitations

The application of submicron CT has already proven its applicability and benefits in various fields from R&D to basic research. But the crucial task for every technique used for any metrological assessment is determining measurement uncertainty, which requires analysis of all critical error sources. For high-resolution CT measurements, the geometrical misalignments of system components and their positional instabilities, including vibrations and thermal instability, are one of the most critical. The aim of this work was to study those limitations and develop optimal solution for their reduction. The main outcome of this work is a dedicated sample's holder with reference area (partially developed in the scope of TAČR Zéta grant - TJ02000127) and corresponding methodology for correcting stage instability and imprecision during CT acquisition process. Part of the results was presented at International Conference on Tomography of Materials & Structures (ICTMS 2022, Grenoble, France, title of submission: "Beyond the limits of lab-based submicron CT for metrology").

### 3.5.1 Analysis of rotational stage stability

In this section, the stability and precision of rotational stage at submicron CT system Rigaku nano3DX is studied. First, thermal dependence of stage positional stability was assessed and then its' overall precision during CT acquisition process was evaluated and put to the context of other laboratory-based CT systems.

#### *3.5.1.1 Thermal stability*

In this experiment, evaluation procedure was proposed to study the thermal dependence of rotational stage stability at Rigaku nano3DX system. Because it was not possible to measure this stability with sufficient precision directly, alternative approach was used. This procedure included acquisition of series of projection images (Lens unit: L0270, Binning: 2x2, Target: Cu, Exposure: 30 s, pixel size: 0.54 µm) of static scene (i.e. no intentional stage movement involved) including reference area in the FoV (see Figure 24) – prototype of latter presented sample's holder was used which contained fiducial marker (Ø 25 µm). The total length of the experiment was set to 300 minutes (corresponding to average CT acquisition process this CT system). The Rigaku nano3DX system does not include internal cooling inside measurement chamber, therefore inside's temperature is dependent on the room temperature. Therefore, during the whole experiment temperatures inside the measurement chamber and room temperature was measured using the datalogger ALMENO 2590-4AS (measurement arrangement is shown in Figure 25). The fiducial present in the FoV was automatically detected in each radiogram using processing procedure defined in section 3.5.2 and position of its' centre was evaluated during the experiment, considering the fiducial's position at beginning of the experiment (i.e., first projection) as reference. To avoid any misinterpretation of the results, the used holder with reference area was placed on the rotational stage 2 hours before the experiment to let it properly set.

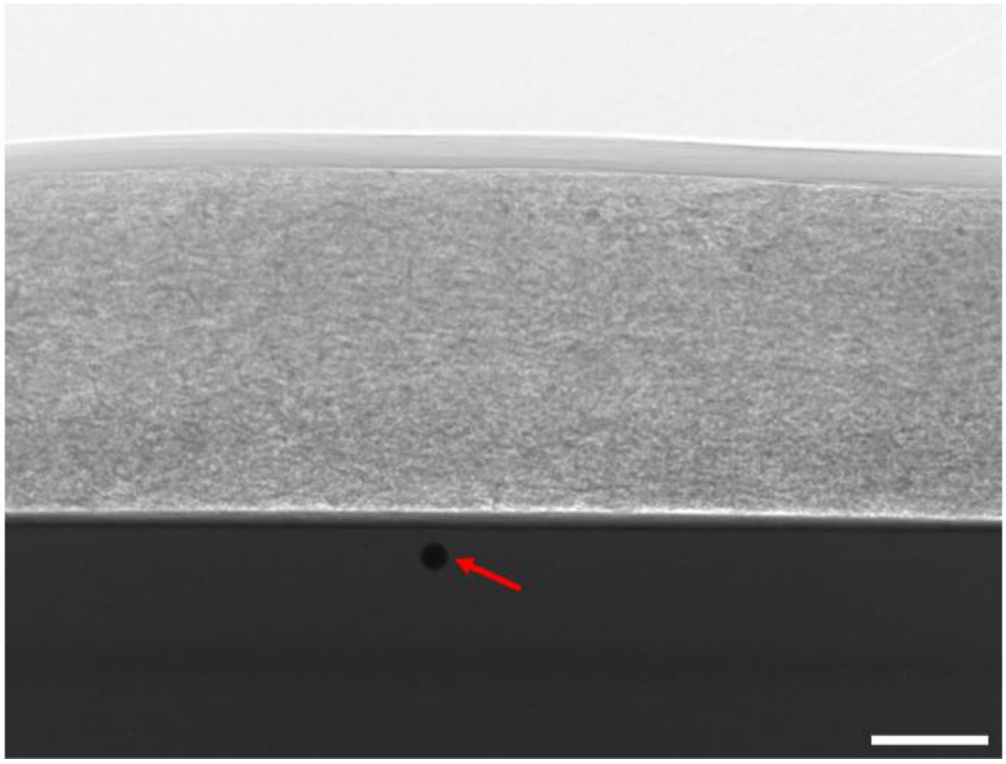

*Figure 24: Radiogram of evaluated static scene containing a reference area (marked by red arrow) in the FoV. Scale bar: 100 µm.*


*Figure 25: Arrangement used within the experiment – red arrow indicates sensor for measuring room temperature and blue arrow indicates sensor used for measuring chamber temperature.*

During the experiment, evaluated temperatures were found to be variable: room temperature fluctuated in interval 22.0 °C – 24.4 °C (mean: 22.7 °C, standard deviation: 0.6 °C) and temperature inside measurement chamber varied in interval 23.0 °C – 24.3 °C (mean: 23.6 °C, standard deviation: 0.3 °C). The temperature's fluctuations, considering the temperature in the beginning of experiment as reference, are visualised in the Figure 26. It was found out that this temperature gradient was affecting the detected stage movement (see Figure 27). This movement was more prominent in vertical direction, when the maximum was 2.6 µm compared to reference position (i.e., fiducial's position in the beginning of experiment). The fiducial's movement was found the be correlated with the temperature in the measurement chamber with the Pearson's correlation coefficients -0.74 for horizontal direction and 0.47 for vertical direction. In this experiment, it was found out that it is crucial to keep the temperature in the measurement chamber during the submicron CT acquisition process as stable as possible, when even the fluctuations below 1°C can result in significant instability of rotational stage affecting results of submicron CT data acquisition.

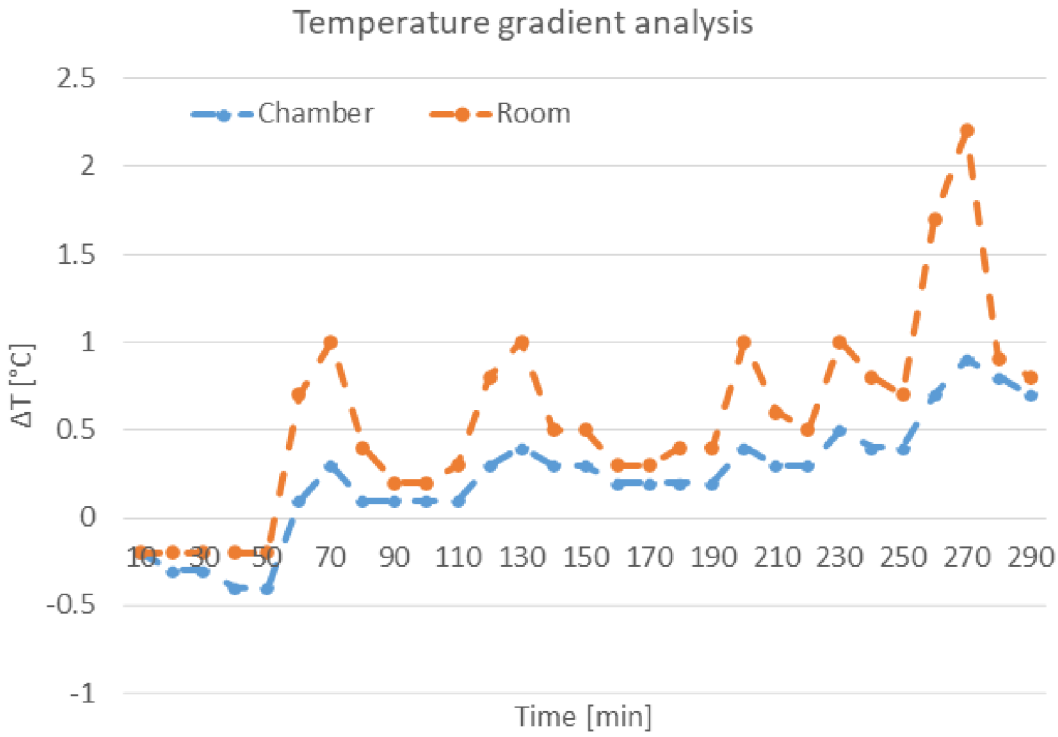


*Figure 26: Temperature fluctuations during the experiment: the temperature in the beginning of experiment was considered as reference.*

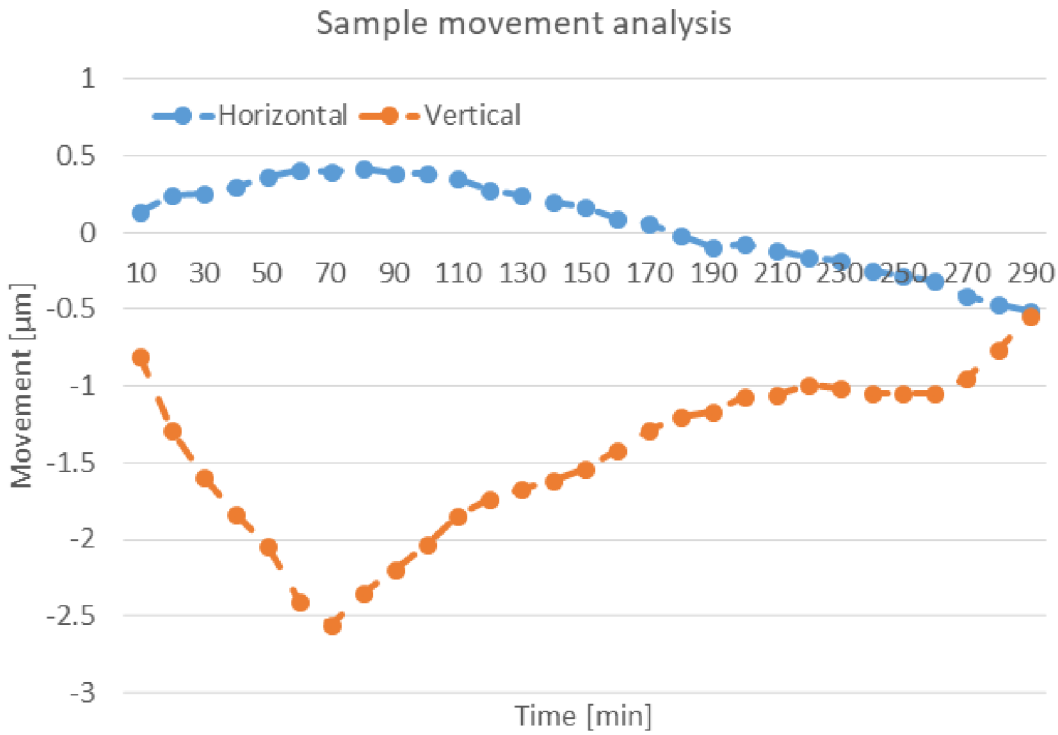


*Figure 27: Stage movement during the experiment: visualised as gradient considering the fiducial's position in the beginning of experiment as reference.*

### *3.5.1.2 Assessment of rotation stage stability and precision during CT acquisition*

In this part, the main aim was to analyse the rotational stage stability and precision during the CT acquisition process. Practical realization of this task was divided into two separate experiments. Firstly, the assessment was conducted for submicron CT acquisition using Rigaku nano3DX system, using 2 measurement strategies: a) relaxation of a sample on the rotational stage before measurement (i.e., sample mounted on the holder with reference area was placed on the rotational stage 2 hours before the experiment to let it properly set) and b) no relaxation involved (i.e., measurement was started immediately after sample's mounting on the stage). Secondly, the assessment was realized for CT acquisition with voxel resolution above one micron and put in the context of three lab-based CT systems (Rigaku nano3DX, Thermofisher Heliscan and GE phoenix v|tome|x L240), for those measurements no sample's relaxation period before acquisition was employed. Used acquisition parameters of all conducted measurements are summarized in Table 17, specific parameters were set according to standard measurement scenarios and following manufacturer's recommendations to measure given sample with the best possible spatial resolution. In case of GE phoenix v|tome|x L240 two measurement settings were involved, when the hardware-based ring artifacts reduction (i.e., intentional stage movement during CT acquisition) was either on or off. For all the measurements the prototype sample's holder with reference area was used together with processing procedure defined in section 3.5.2

*Table 17: Acquisition parameters of CT measurements performed within analysis of rotational stage stability during CT acquisition, for all devices circular trajectory was used.*

| **Device** | **Rigaku nano3DX** | | | **Thermofisher Heliscan** | **GE phoenix v\|tome\|x L240** |
|---|---|---|---|---|---|
| Voltage | 40 kV | 40 kV | 40 kV | 60 kV | 50 kV |
| Current | 30 mA | 30 mA | 30 mA | 120 mA | 120 mA |
| Exposure | 16 s | 16 s | 20 s | 4 s | 0.4 s |
| Binning | 2x2 | 2x2 | 2x2 | 1x1 | 1x1 |
| Voxel size | 0.53 µm | 0.53 µm | 1.06 µm | 1.19 µm | 2.00 µm |
| Averaging | - | - | - | 2 | 2 |
| Angle range | 180° | 180° | 180° | 360° | 360° |
| Projections | 800 | 800 | 800 | 3150 | 2300 |
| Relaxation | Yes | No | No | No | No |

Firstly, the effect of sample's relaxation on the rotational stage before submicron CT acquisition was evaluated. According to the results (Figure 28 and Figure 29), it is evident that including the stabilization period was beneficial especially in the initial phase of the CT measurement. In the remaining part of the measurement there were no significant differences, when both measurement scenarios followed similar periodic trend probably corresponding to the temperature fluctuations in the measurement chamber.

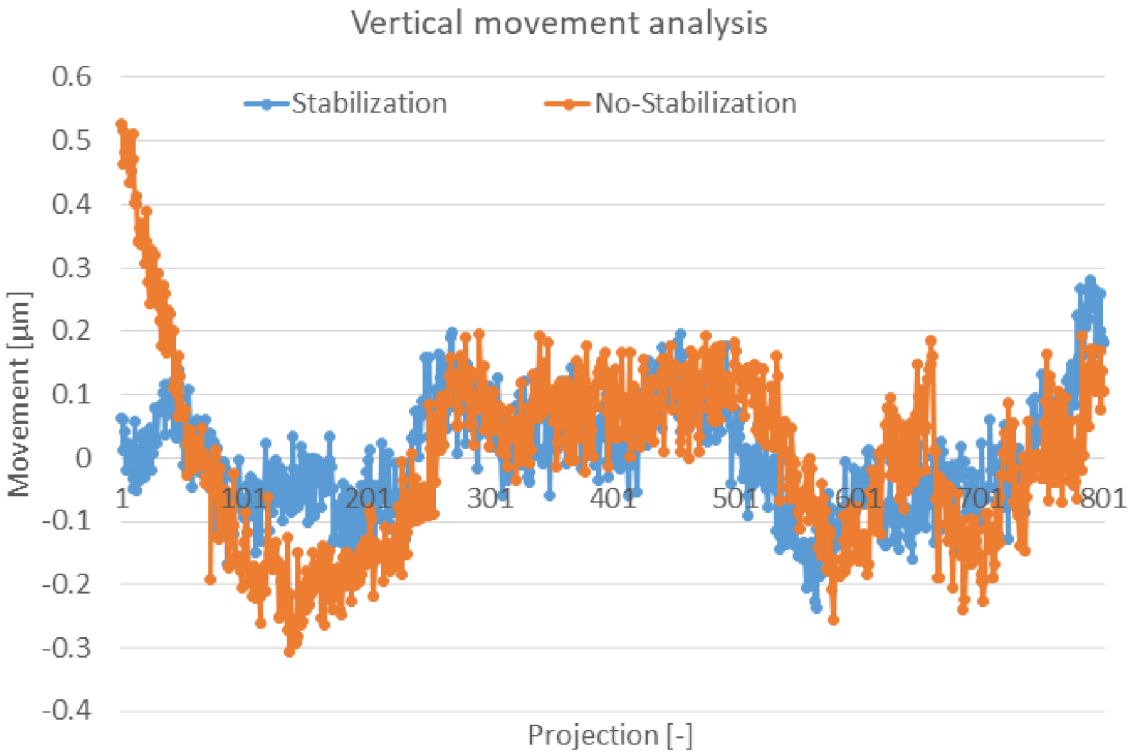


*Figure 28: Evaluation of the effect of sample's relaxation on the rotational stage before submicron CT acquisition: vertical movement.*

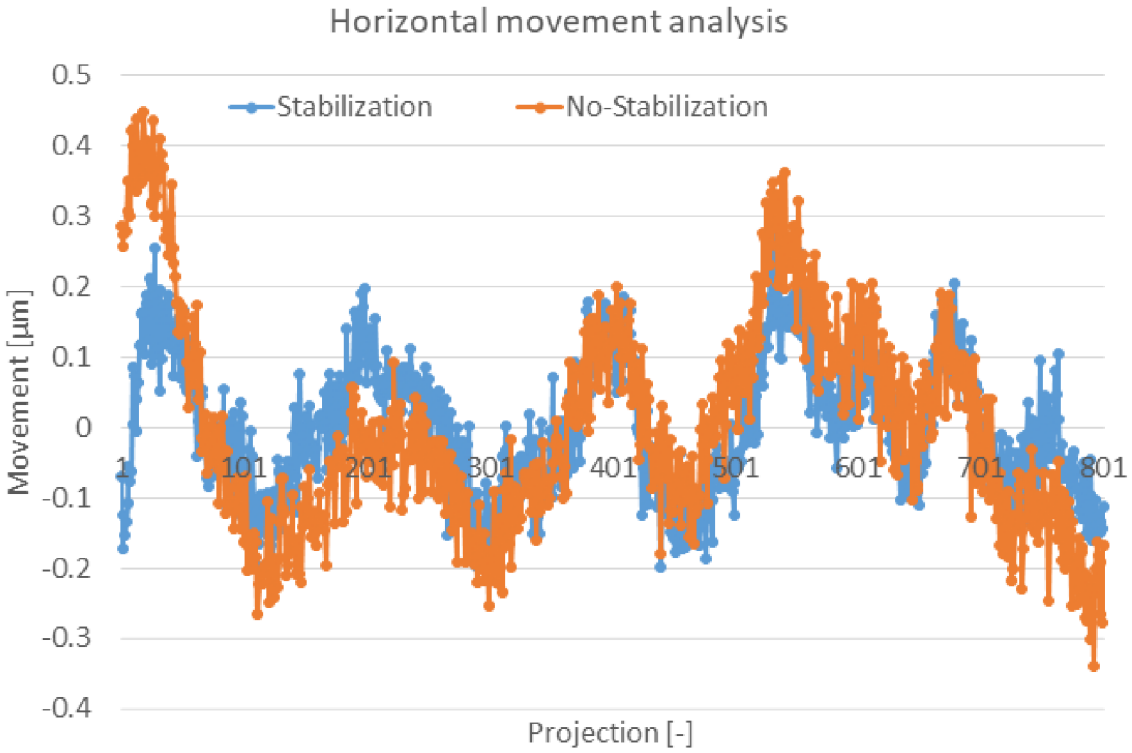


*Figure 29: Evaluation of the effect of sample's relaxation on the rotational stage before submicron CT acquisition: horizontal movement.*

Secondly, the rotational stage stability and precision assessment was realized for CT acquisition with voxel resolution above one micron and put in the context of three lab-based CT systems. The acquired results are summarised in the Table 18. For both Rigaku and Thermofisher CT systems the observed can be considered as negligible (below the voxel resolution of given measurements). In case of GE phoenix v|tome|x L240 both tested measurement scenarios resulted into significant movement. Especially when the hardware-based ring artifacts reduction was employed, the movement was found to be significant, reaching the maximum values of 25.93 µm in horizontal direction and 4.0 µm in vertical direction, corresponding to low functionality of used procedure in terms of precision of stage movement.

*Table 18: Comparison of CT systems in terms of their rotational stage precision during CT acquisition.*

| Device | Vertical movement [µm] | | Horizontal movement [µm] | |
|---|---|---|---|---|
| | Mean | Maximum | Mean | Maximum |
| Rigaku Nano3DX | -0.01 ± 0.13 | 0.35 | 5.73 e-05 ± 0.11 | 0.34 |
| Thermofisher Heliscan | -0.03 ± 0.24 | 0.92 | 5.62 e-10 ± 0.20 | 0.85 |
| GE phoenix v\|tome\|x L240 – RAR* on | -0.07 ± 2.15 | 4.00 | 0.00 ± 8.77 | 25.93 |
| GE phoenix v\|tome\|x L240 – RAR* off | 0.04 ± 0.70 | 2.25 | 4.22 e-07 ± 2.26 | 5.81 |

** Refers to hardware-based ring artifacts reduction*

In summary, it was found out that detectable stability and imprecision of rotational stages was variable among particular CT systems and also dependent on used acquisition parameters such as the voxel resolution or hardware-based ring artifacts reduction. Especially for submicron CT measurements using Rigaku nano3DX system, it was out that for such high-resolution measurements it is beneficial to let the sample relax and set on stage before starting the measurement.

### 3.5.2 Correction of rotational stage imprecision and instability

In the sphere of high-resolution CT, there are strict requirements on hardware components, when their positional instabilities are one of the most critical error sources. However, it is technologically almost impossible to achieve precision of those mechanical components that would be substantially smaller than the smallest achievable voxel size for given system. As presented in the previous section (3.5.1), the stability or rotational stage and its precision during submicron CT acquisition can be decreased by various factors. There exist various strategies for correction of rotational stage imprecision during the CT acquisition. Till today the marker-based methods are still the most used having various benefits over the marker-less methods such as low computational demands and robustness to acquired data quality. However, those techniques require mounting selected fiducials (usually golden particles with diameter ranging from nanometres to micrometres) on a sample prior CT acquisition. Especially for submicron CT applications, this is a very challenging task posing high demands on an operator and his skills.

The objective of this work was to create a multi-purpose solution for high-resolution CT applications that would allow to reduce the limits of current technology and overcome limits of existing correction techniques. Inspired by marker-based methods, this resulted into development of an advanced sample's holder containing reference area, therefore, no fiducial manipulation and mounting is required. This project was a follow-up of successful TAČR Zéta grant - TJ02000127: Differentiation of soft tissues using dual-target tomography, where one the outputs was a functional prototype of sample's holder with reference area for alignment of two datasets. Within practical realization of the project TJ02000127, the concept of dedicated sample holder with a reference area was proposed and designed (see Figure 30). This concept was then practically verified by creation of first functional prototype that was then tested in field trials. The concept was confirmed as successful for data registration of CT datasets of biological tissues acquired by dual-target CT practically implemented on Rigaku nano3DX system. Further, this concept was extended to enable not only the CT data registration with sub-pixel precision but to be also applicable for correction of rotational stage inaccuracies to enhance the overall quality and precision of acquired CT data. This was mainly achieved by development of dedicated processing methodology and its implementation.

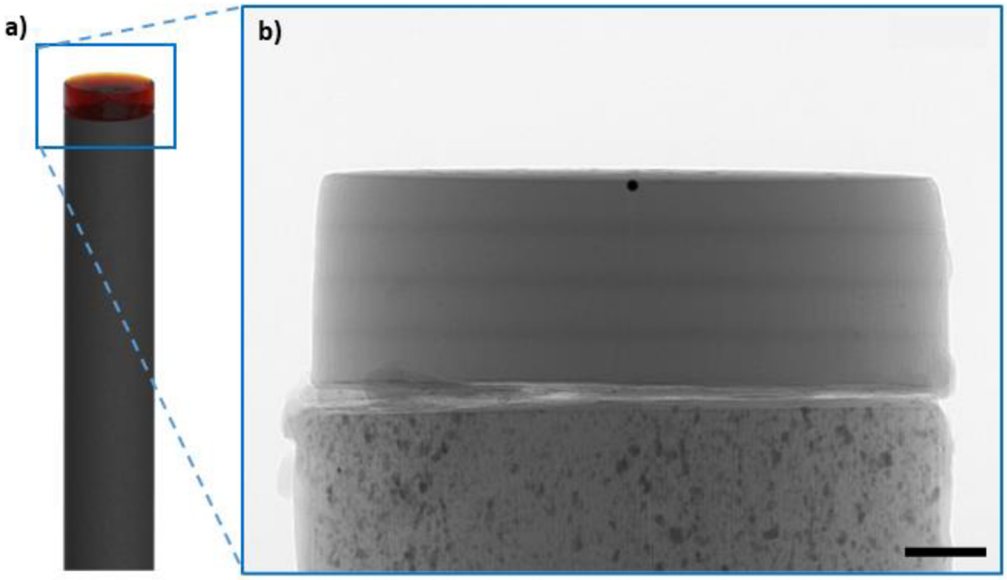


*Figure 30: Developed sample's holder with reference area: a) 3D render of technical design; b) Radiogram of the top part with fiducial marker. Scale bar: 100 µm.*

#### *3.5.2.1 Proposed methodology for correction of rotational stage imprecision and instability*

In this methodology, advantageous features of marker-based and marker-less methods are combined into complex procedure overcoming their individual limits. This procedure combines using developed sample's holder with reference area with dedicated processing procedure to allow for correction of rotational stage inaccuracies (i.e., centre of rotation misalignment and stage instability/movement during CT acquisition). Respectively to order of CT acquisition procedure, the methodology first consists of guidelines for optimal CT acquisition using developed sample's holder:

1. Mounting a sample on the top of a developed holder, the sample should be fixed properly to avoid unrelated movement of the sample and the holder.
2. Mounting the holder with the sample on the rotational stage of a CT device – if recommended by manufacturer of used CT system, allow it to thermally adapt for conditions in the measurement chamber and properly set on the rotational stage before CT measurement.
3. Setting the sample's position in FoV for CT measurement to make sure that the fiducial is visible in every projection image.
4. Setting the acquisition parameters (i.e., accelerating voltage and current, exposure, binning, averaging) according to standard guidelines for your CT device to reach a sufficient level of detected signal.
5. Starting the CT measurement.

Within the proposed data processing procedure, acquired projection data are analysed. For the analysis only bottom part of projection data (containing fiducial) is used to reduce computational demands. The data is further pre-processed by denoising (both impulse noise and shot noise are reduced using methodologies presented in section 3.3). Fiducial is then segmented in each projection image by global thresholding using combination of automatic threshold selection using Otsu's method [45] and local statistics evaluation. To calculate the fiducial's centres, the binary masks are fitted by circles using combination of Taubin [46] and Levenberg-Marquardt [47] methods. Having positions of fiducial's centres, both the rotary axis misalignment and sample's movement can be estimated and corrected. The rotary axis misalignment is estimated by evaluation of the fiducial's centre horizontal coordinates between corresponding projections at 0° and 180°. In ideal case, these two images should be only mirrored, if any horizontal shift between them is detected, its' half corresponds to rotary axis shift. Sample's movement is then estimated separately in vertical and horizontal directions using the coordinates of fiducial's centres. Both coordinates are fitted by ideal trajectories (i.e., sine function in vertical direction and cosine function in horizontal direction) and sample's movement is then calculated as deviation from those trend curves, similarly as in the work of Cheng [48]. For correction of both the rotary axis misalignment and samples movement it is recommended to use the b-spline interpolation method to reach the sub-pixel precision or optimizing the projection geometry within the tomographic reconstruction process.

#### *3.5.2.2 Results*

The functionality of proposed methodology for correction of rotational stage imprecision and instability is demonstrated on submicron CT measurement of pharmaceutical sample using Rigaku nano3DX system (Lens unit: L0270, Binning: 2x2, Target: Cu, Exposure: 30 s, voxel size: 0.54 µm). From the results (see Figure 31), it is evident that using proposed procedure the acquired data quality was significantly improved, when all the movement and rotary axis misalignment artifacts were reduced.

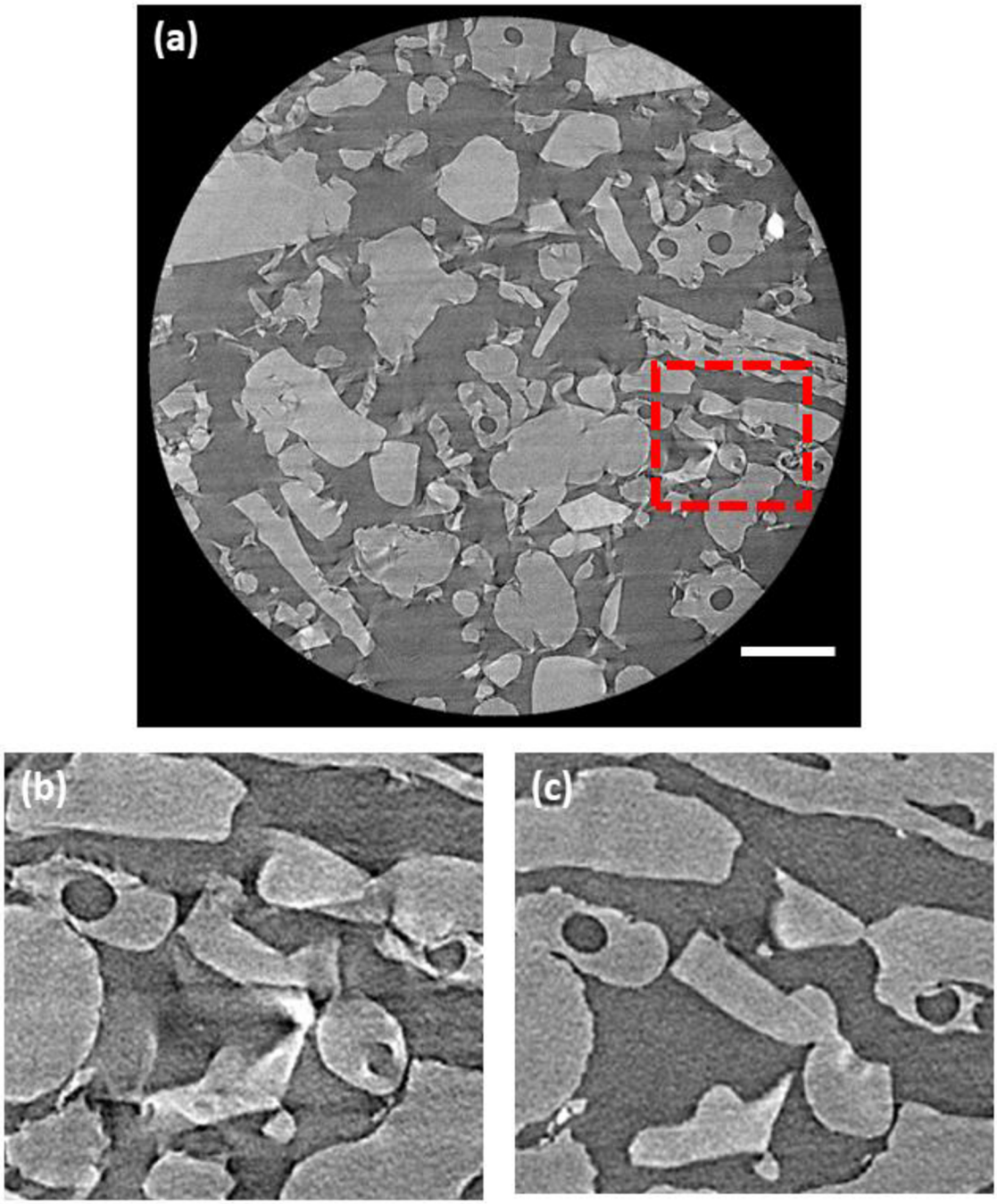


*Figure 31: Results of proposed methodology for correction of rotational stage imprecision and instability, demonstrated on pharmaceutical sample: a) and b) original data; c) corrected data. Scale bar: 100 µm.*

# 4 Spectral imaging

Spectral imaging has in recent years remerged in CT practise, mainly due to technological advances that enabled its' practical implementation. Spectral imaging methods generally aim to increase overall accuracy and quality of CT imaging including methods for tomographic artifacts reduction and to practical implementation of advanced quantification tools for sample's characterization. In terms of practical implementation of spectral CT, two main concepts can be applied, either the detector-based or X-ray source-based. The focus of this work is X-ray source-based Dual-energy CT, which refers to scanning at two energy levels and is a special case of spectral CT. Dedicated CT systems were designed exclusively for DECT, such as the Rigaku nano3DX system. Using this device, not only two energy separate X-ray spectra but also material specific spectra can be achieved during DECT by switching the X-ray source target material. Therefore, this special implementation of DECT is hereafter named as Dual-Target CT (DTCT). However, all the X-ray source-based approaches are practically limited by possible misalignment of acquired data and also by lack of knowledge about practical aspects of setting up DECT measurements. In this work, both these issues are addressed and practically implemented for Rigaku nano3DX device.

## 4.1 DTCT imaging using Rigaku nano3DX device

The DTCT measurement using the Rigaku nano3DX device consists of two consecutive acquisitions, between which, in addition to the change in the maximum energy of the X-ray radiation, the material of the target of the X-ray source (Cu and Mo), in which the radiation is generated, is changed. Resulting X-ray spectra are not only energetically but also materially different, which helps their separation (see Figure 32). This follows a generally valid rule for DECT, that between both measurements there should be sufficient spectral separation, meaning that the used X-ray spectra should have as small overlap as possible [49].

The sequential character of DTCT data acquisition, requires optimization of acquisition protocol to achieve sufficient data quality for subsequent data processing. In scope of this work, acquisition protocol is proposed to ensure optimal data quality for subsequent processing by optimizing the exposure times for both measurements. This protocol is based on procedure, where Cu target measurement is considered as refence in terms of noise properties and the exposure time for measurement using Mo target is optimized to reach comparable noise properties (for more details see section 4.2). The exposure time for reference measurement is then selected according to the recommendations of Rigaku (i.e., manufacturer of given device). For the DTCT acquisition, it is also proposed to use the developed samples holder with reference area (more details in section 3.5.2), that is utilized both for samples mounting and for the registration of acquired data. In terms of DTCT data processing, it is required that the data are perfectly aligned (i.e., corresponding structures are located on the same positions for both data), however, it is hardly achievable especially for submicron CT measurements mainly due to the rotational stage instability during CT acquisition (see section 3.5) and software-based alignment is therefore necessary. To simplify the task for data registration, it is also recommended to optimize the sample's preparation and mounting to reach sufficient stability and possible eliminations of sample's movement during CT acquisition process.

The proposed DTCT acquisition protocol for the Rigaku nano3DX device is summarized below:

1. Sample's mounting on the developed sample's holder with reference area.
2. CT data acquisition using Cu target (reference measurement):

a. exposure time set according to the manufacturer's recommendations to reach optimal contrast.

3. Switching the target material (Cu → Mo).
4. CT acquisition using Mo target (high energy measurement):
    a. exposure time set according to noise properties in reference measurement – minimizing the difference of total noise standard deviations in bright frames for Cu and Mo measurements (for more details see section 4.2).
5. Projection data processing:
    a. correction of rotational stage instability and imprecision for Cu projection data according to the procedure defined in section 3.5.2.1,
    b. transformation of Mo projection data according to the Cu projection data (for more details see section 4.3).
6. Tomographic reconstruction:
    a. reconstruction of aligned projection datasets using procedure defined in section 3.1.

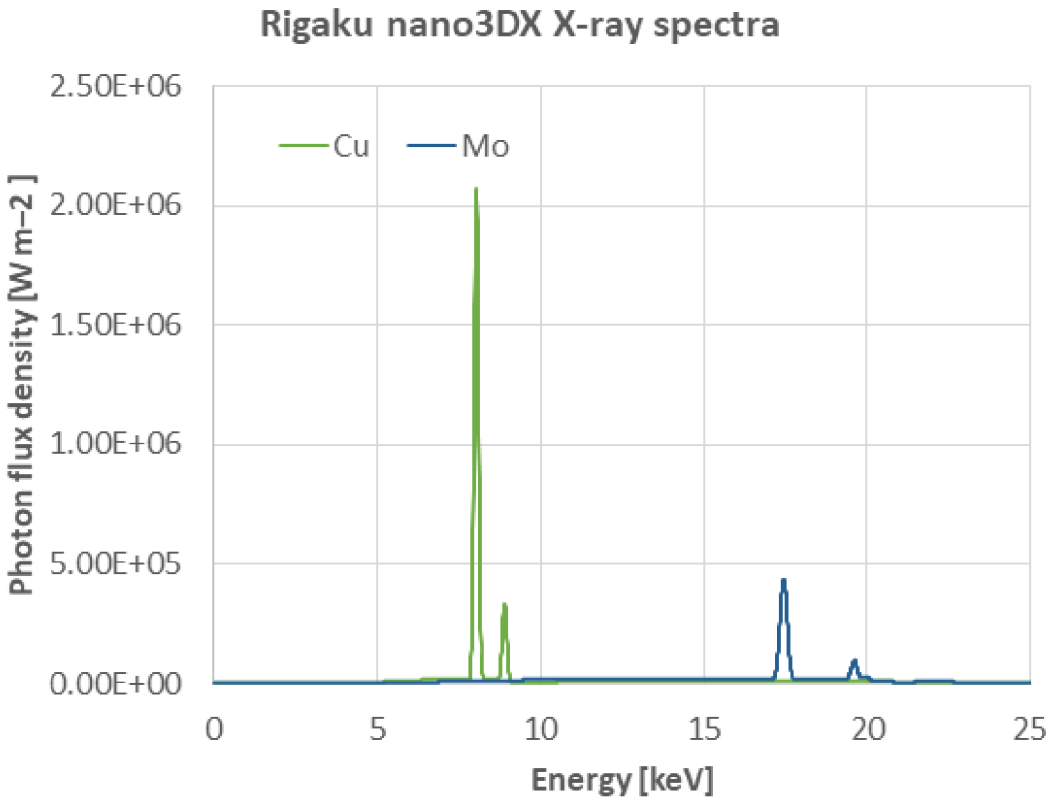


*Figure 32: X-ray spectra of Rigaku nano3DX (after 250 mm of air travelling) using both Cu and Mo target materials.*

## 4.2 DTCT acquisition settings

As already mentioned, the sequential character of DTCT data acquisition, requires optimization of acquisition protocol to achieve sufficient data quality for subsequent data processing. However, data acquired using different X-ray spectra mainly differ in terms of noise properties corresponding to different X-ray flux in both measurements, different detector sensitivity to individual X-ray energies and other factors. In the literature, this is usually solved by optimization of used X-ray spectra to achieve the best SNR [50]. However, during practical experiments it was found out that SNR is not ideal metric, because it does not respect the signal generation for different energies levels. Moreover, in case of nano3DX system, the X-ray spectra are unchangeable, and it is, therefore, necessary to optimize the data quality using different approach. Using nano3DX system the only relevant parameter in terms of setting up the parameters of DTCT measurements is the exposure time. Other theoretically relevant parameters affecting the shape of X-ray spectrum, such as accelerating voltage or current, are fixed by the manufacturer to achieve the maximal usage of characteristic part of X-ray spectrum for given target material. Therefore, it was proposed to optimize the exposure times according to noise properties of bright frames before flat-field correction of both Cu and Mo target measurements.

### 4.2.1 Noise dependence on acquisition parameters

First, noise properties dependence was studied for various acquisition parameters that are relevant within regular CT measurements using Rigaku nano3DX system equipped with CCD-based detector (XSight™ Micron LC X-ray CCD camera [17]). Specifically, we evaluated the effects of binning, sample-detector distance (refers to parameter XD), optical lens unit (i.e., optical magnification) and also used target material and related X-ray beam filtration. The used acquisition parameters are summarized in Table 19. Total noise was quantified from set of bright-field frames by subtraction of an average bright-field frame from intensity stabilized frames and then quantified using standard deviation calculation. This parameter was calculated for central area of original bright-frames (not flat-field corrected), when square-shape ROI with size scaled according to binning (1000 pixels' width for binning 1x1) was evaluated.

*Table 19: List of acquisition parameters used within noise dependence study.*

| | |
|---|---|
| Target material: | Cu/ Mo |
| Beam filtration: | None/ Al plate with 0.1 mm thickness (manufacturer recommendation when measuring high-density samles with Mo target) |
| XD [mm]: | 0.0/ 1.0/ 2.0 |
| Lens unit: | L0270 (FoV: 0.7 × 0.9 mm; minimal pixel size: 0.27 µm)/ L0540 (FoV: 1.4 × 1.8 mm; minimal pixel size: 0.54 µm) / L1080 (FoV: 2.8 × 3.6 mm; minimal pixel size: 1.08 µm) |
| Binning: | 1×1/ 2×2/ 4×4 |
| Exposure time [s]: | From minimal to exposure level for which the signal level in the central area of the FOV is 75% of the saturation level (i.e., around 45 000 DN for 16bit) |
| Number of projections: | 10 per exposure level |

#### 4.2.1.1 *Effect of binning*

According to the acquired results (see Figure 33), the total noise standard deviation was found to be exponentially dependent on exposure and linearly proportional to the used binning factor.

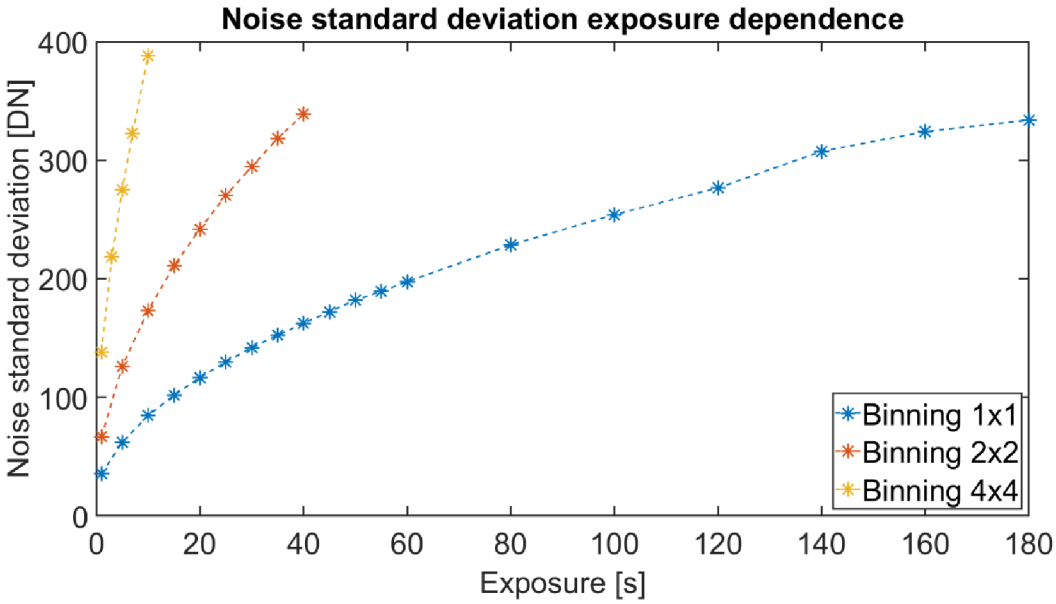


*Figure 33: Total noise standard deviation dependence on exposure and binning, evaluated for Cu target.*

#### 4.2.1.2 *Effect of XD distance*

Acquired results (see Figure 34) showed that the effect of XD distance on total noise properties is negligible within the commonly used interval of distances referring to regular CT measurements at used CT system.

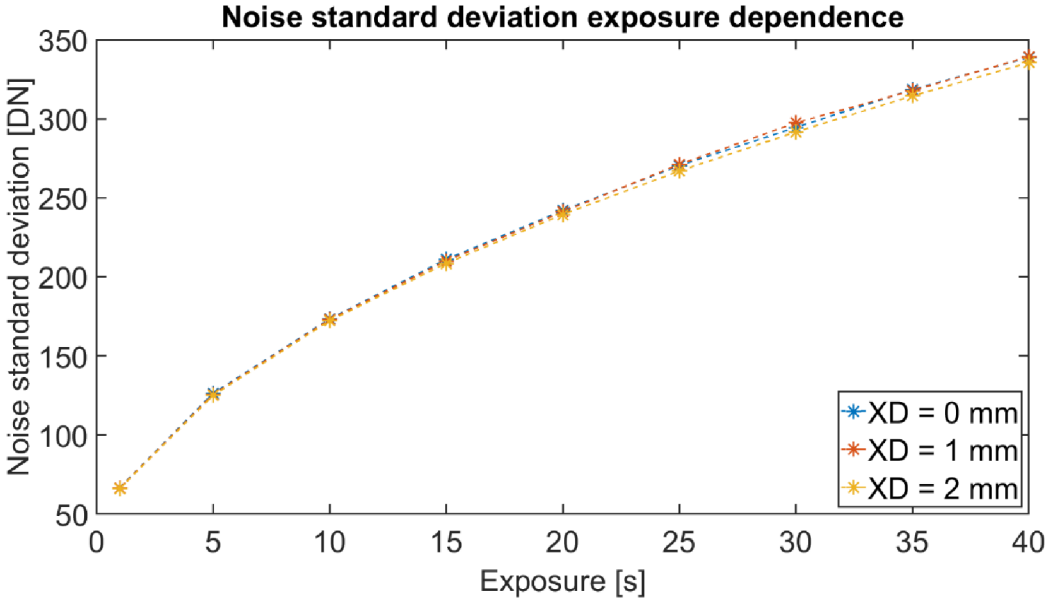


*Figure 34: Total noise standard deviation dependence on exposure and XD distance (refers to sample-detector distance), evaluated for Cu target*

#### *4.2.1.3 Effect of used target material*

According to the acquired results (see Figure 35, Figure 36 and Figure 37), the effect of used target material and beam filtration (aluminium plate with thickness 0.1 mm) was found to be variable within tested optical lens units. Specifically, for L0270 optical lens (Figure 35) the difference between Cu target and Mo target with beam filtration was found to be almost negligible. However, for the other two tested optical lens units, the difference between Cu and Mo targets was more relevant.

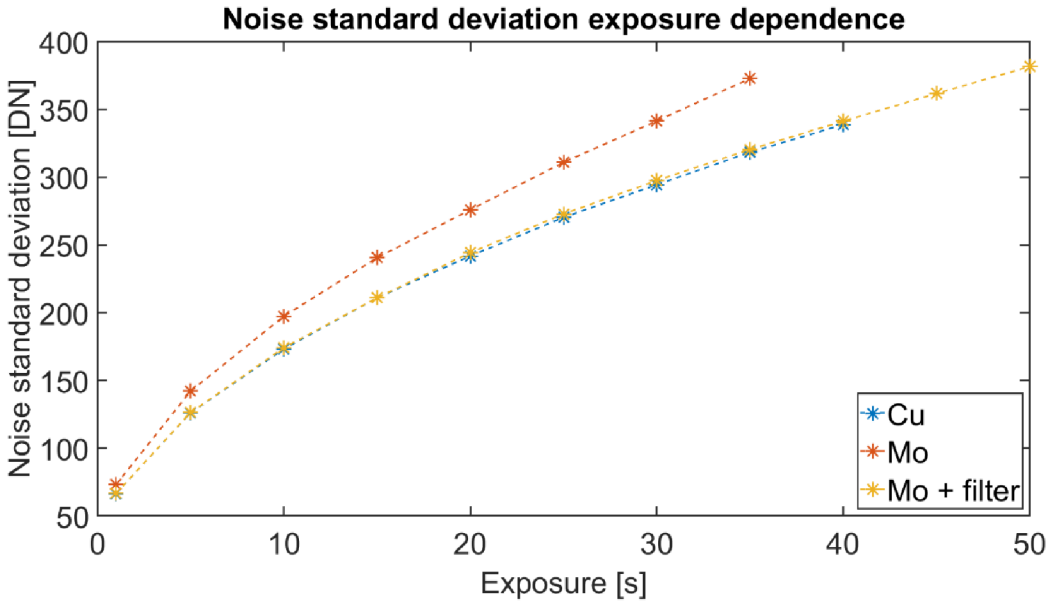


*Figure 35: Total noise standard deviation dependence on exposure and used target material, evaluated for optical lens unit L0270, binning 2×2.*

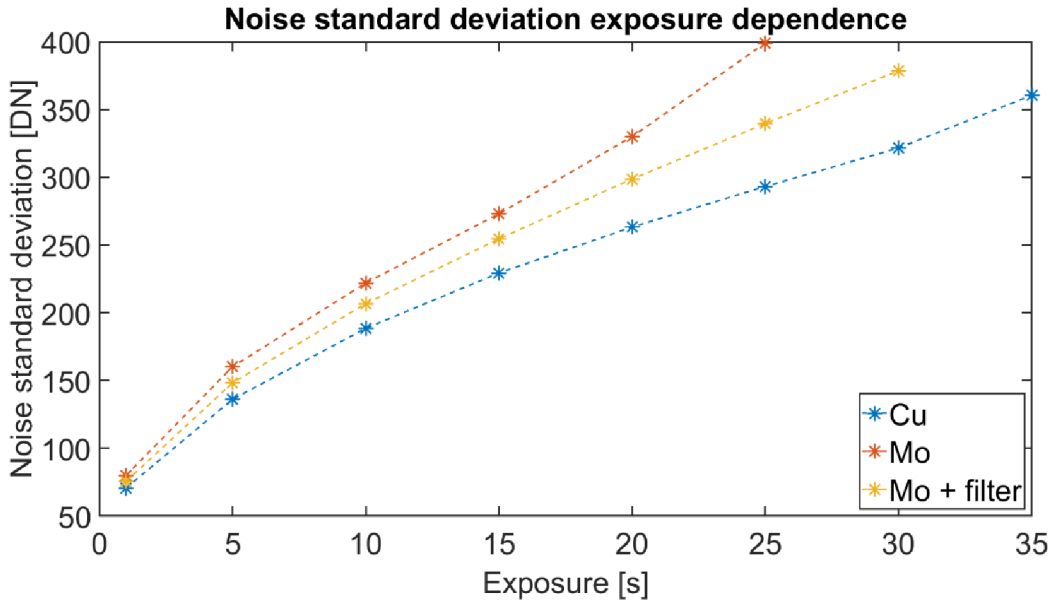


*Figure 36: Total noise standard deviation dependence on exposure and used target material, evaluated for optical lens unit L0540, binning 2×2.*

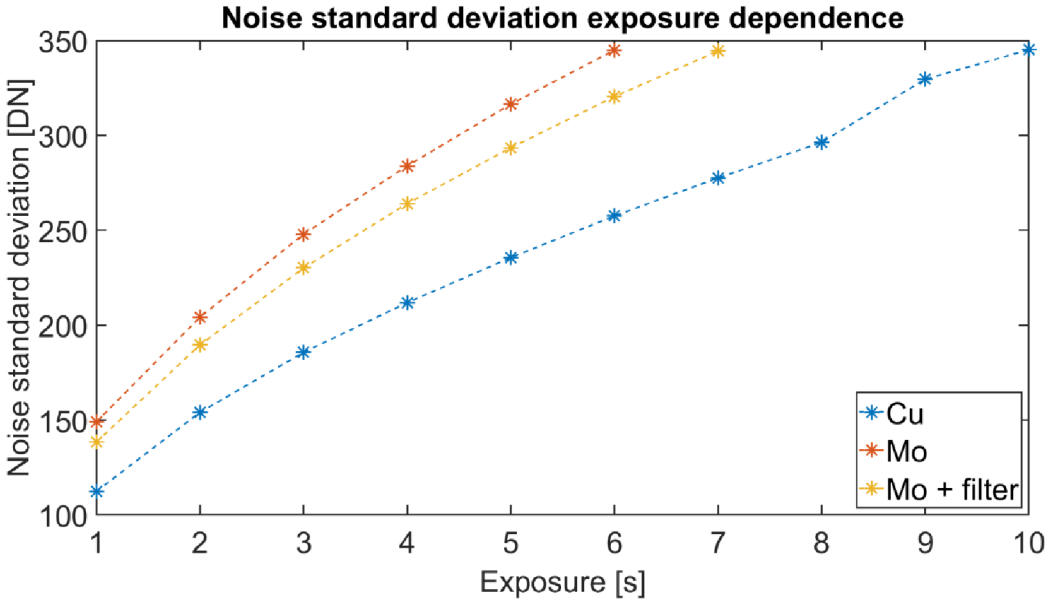


*Figure 37: Total noise standard deviation dependence on exposure and used target material, evaluated for optical lens unit L1080, binning 2×2.*

#### *4.2.1.4 Effect of used optical lens unit*

According to the acquired results (see Figure 38, Figure 39 and Figure 40), the effect of used optical lens unit was found to be almost negligible within tested target materials and beam filtration, but still unique for given optical lens unit.

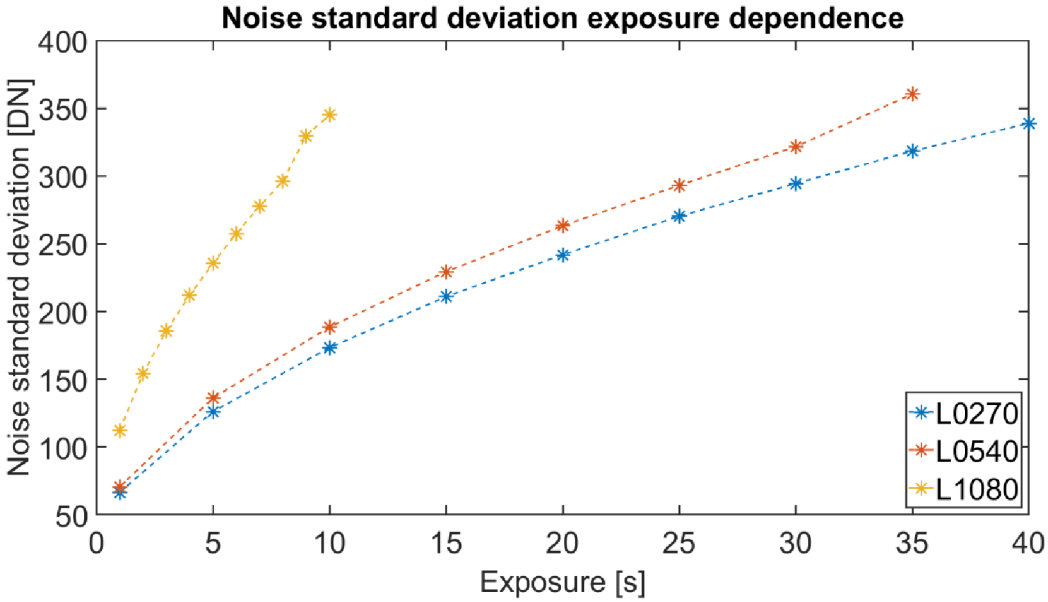


*Figure 38: Total noise standard deviation dependence on exposure and used optical lens unit, evaluated for Cu target.*

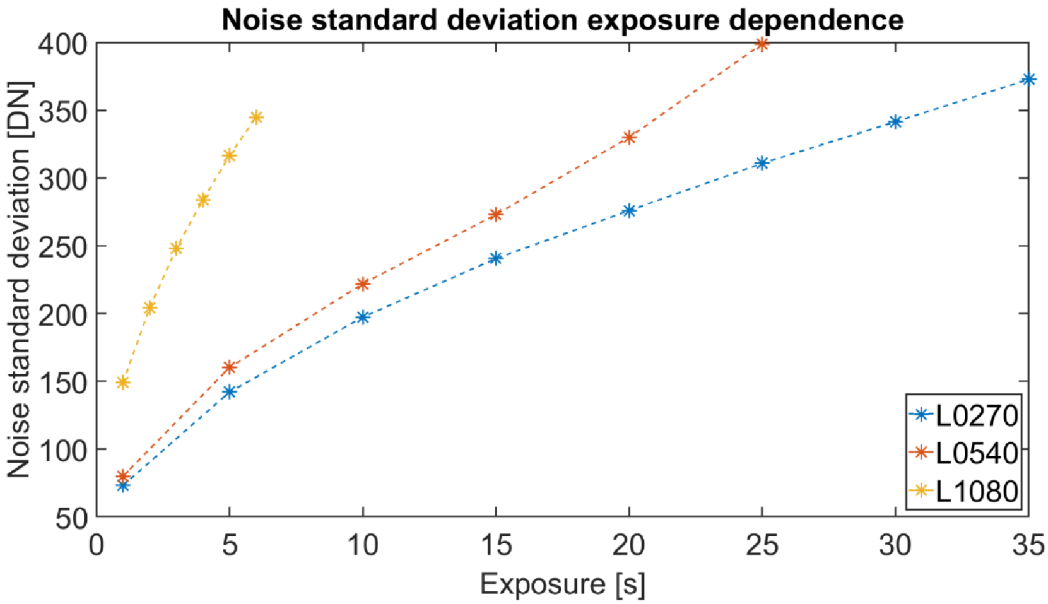


*Figure 39: Total noise standard deviation dependence on exposure and used optical lens unit, evaluated for Mo target, binning 2×2.*

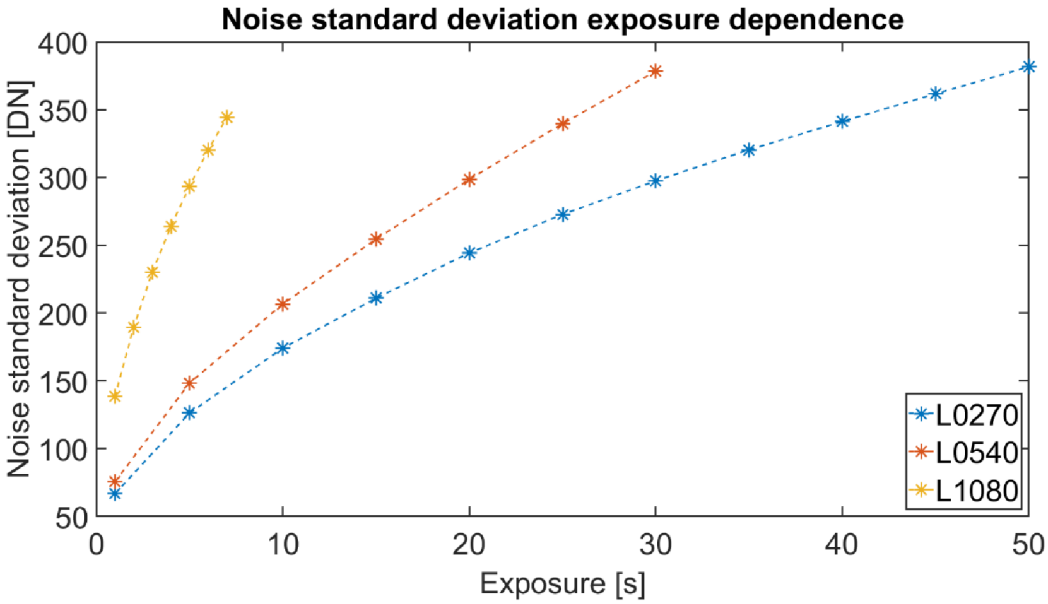


*Figure 40: Total noise standard deviation dependence on exposure and used optical lens unit, evaluated for Mo target with beam filtration (aluminium plate with thickness 0.1 mm), binning 2×2.*

### 4.2.2 Proposed strategies for exposure estimation

In scope of this work, it is proposed to use the standard deviation of total noise calculated from bright frames before flat-filed correction as optimization metric to set ideal exposure times for DTCT measurements using Rigaku nano3DX system. Specifically, the noise properties from Cu target measurement are considered as reference and exposure time for Mo target measurement is set to reach minimal difference in this parameter. Using this strategy, robust criteria is achieved that is independent on sample's properties and other factors. Considering the result from the previous section, two approaches are proposed within practical implementation of this strategy and summarized below including their individual advantages and disadvantages:

1. **Utilization of conversion factors:**
    - Multiplying reference exposure (Cu) by corresponding conversion factor (for more details see section 4.2.2.1).
    - Advantage – exposure for second measurement is calculated directly, no further data is required.
    - Disadvantage – calculation of conversion factors must be done for each CT setup, every optical lens unit and target material individually. The models are not constant, because properties of CT system components are not persistent.
2. **Bright frames analysis for each measurement individually:**
    - Bright frames acquisition and analysis before second measurement to set exposure having similar noise standard deviation as reference measurement (bright frames from first measurement are required):
        i. Acquisition of bright frames for at least 5 exposures around reference exposure (10 frames per exposure) and calculation of total noise standard deviations for given exposure.
        ii. Regression analysis of calculated noise dependence on exposure levels.
        iii. Estimating the exposure time with similar total noise standard deviation as for reference measurement.
    - Advantage – generally applicable and robust solution without any requirements for priory information.
    - Disadvantage – additional measurements of bright frames lead to longer acquisition time and significant time gap between the two consecutive CT measurements, when sample movement or structural changes can occur.

#### *4.2.2.1 Optimal exposure estimation according to regression model's analysis*

Using the results presented in section 4.2.1, noise dependence models on exposure of Mo target measurements with and without beam filtration were estimated for all tested optical lens units, considering the binning 2×2, which is the preferred settings in terms of given CT system. Those models were calculated using regression analysis, where the dependence of total noise standard deviation on exposure was used as the input. The individual regression models (see Figure 41) were manually optimized to achieve the best possible results in terms of regression (i.e., R-Squared coefficient was maximized). Using those models, noise standard deviation values were estimated for whole considered exposure's interval with step 0.01 s. Real measured Cu target values were then considered as reference and for each of those values the closest values for Mo target with and without filter were found using Euclidean distance metric. For such estimated noise standard deviation values corresponding

exposures were extracted. Conversion coefficients for each measured Cu exposure were estimated as ratio of those exposures and corresponding exposures for Mo target with and without filter (see Figure 42, Figure 43 and Figure 44). For all the evaluated optical lens units, the conversion factor reaches higher values for low exposures compared to remaining exposure interval, which corresponds to dark current and read-out noise components that are predominant for those exposures. In case of L1080 optical lens unit, the drop of conversion factor values at the end of exposure interval corresponds to the proximity of saturation level.

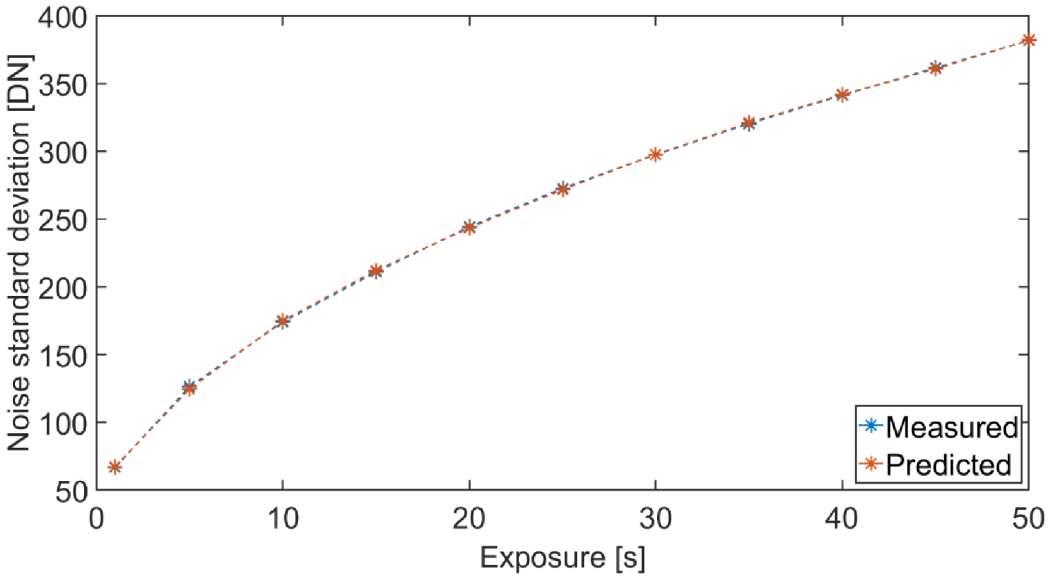


*Figure 41: Comparison of real measured data and calculated noise standard deviation regression model for Mo target with beam filtration (0.1 mm Al filter) and L0270 optical lens unit and binning 2×2. Parameters of the model: polynomial: 5; Root Mean Squared Error: 1.35; R-squared: 1.*

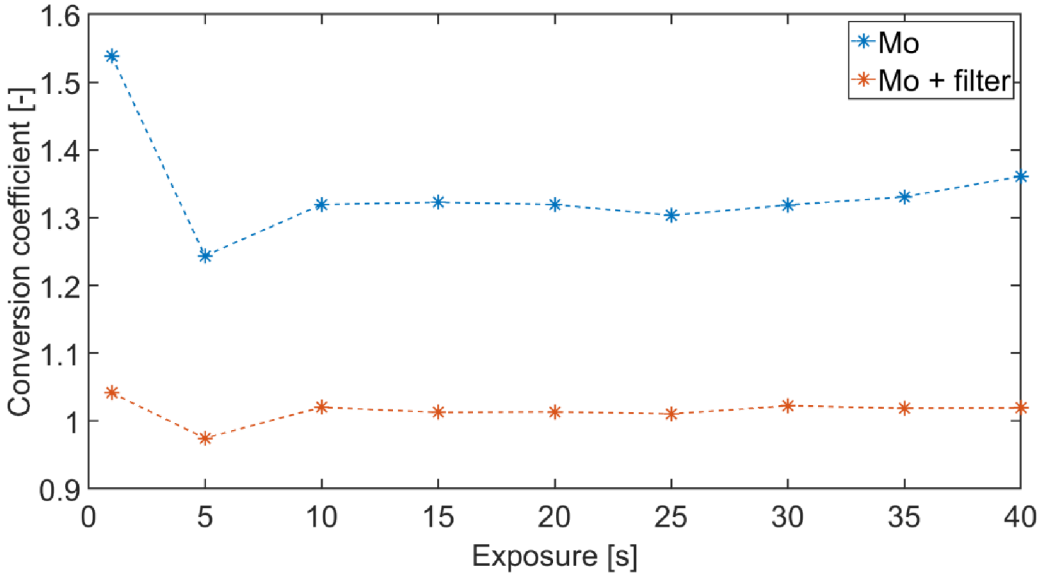


*Figure 42:Conversion coefficients calculated for L0270 optical lens unit, binning 2×2.*

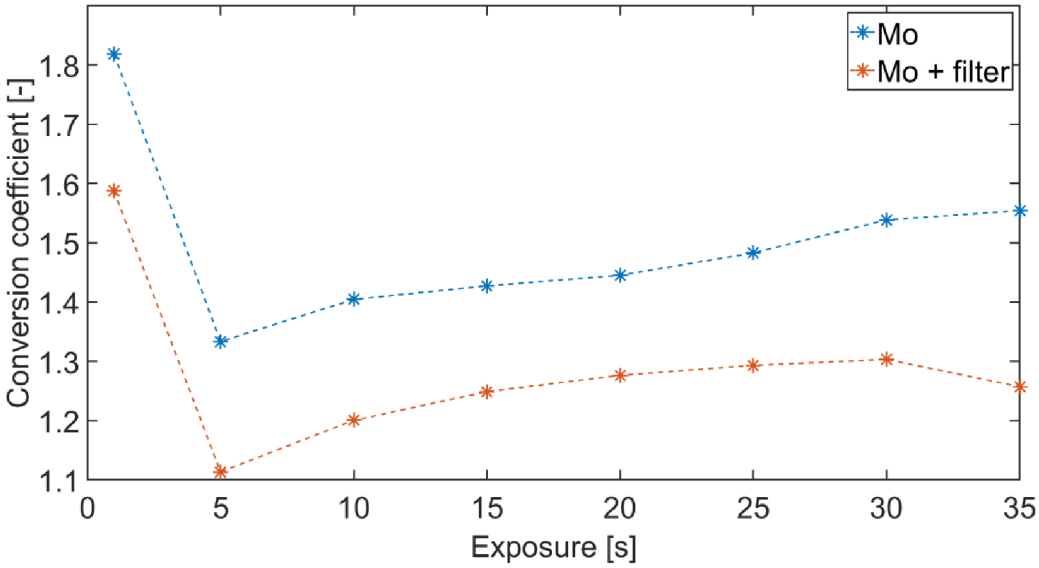


*Figure 43:Conversion coefficients calculated for L0540 optical lens unit, binning 2×2.*

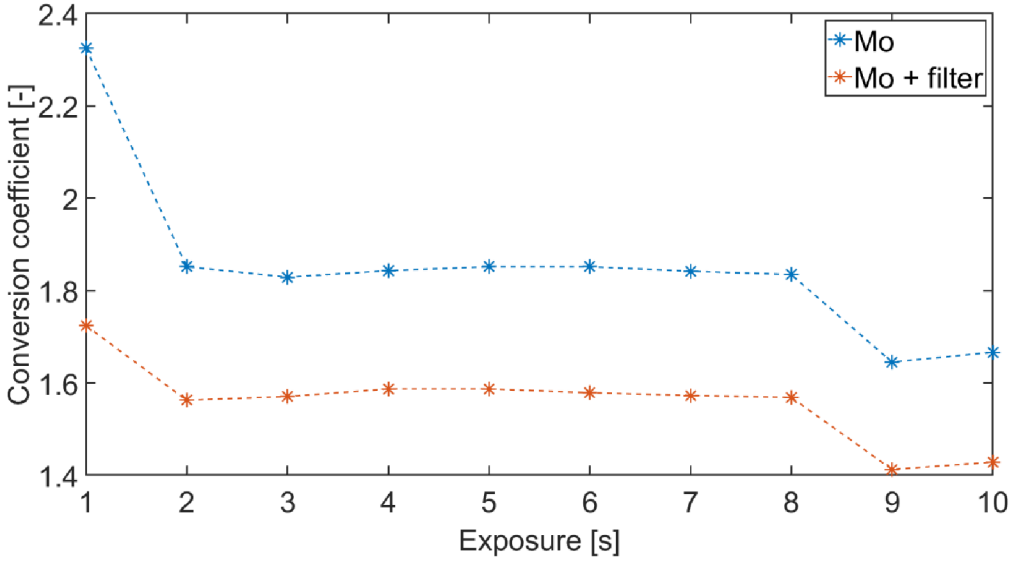


*Figure 44:Conversion coefficients calculated for L1080 optical lens unit, binning 2×2*

## 4.3 DTCT data registration

In terms of DTCT data processing, it is required that the data are perfectly aligned (i.e., corresponding structures are located on the same positions for both data). However, due to sequential character of DTCT acquisition using Rigaku nano3DX system, a difference in sample position between the two measurements cannot be ruled out because of various factors such as rotational stage instability (3.5.1) or sample's structural movement. Therefore, DTCT data alignment is necessary before further processing. Image registration is a process of transforming data from different sets of measurements into one coordinate system, which means that corresponding structural information from different times or imaged by different imaging modalities will be on same spatial coordinates. Practically it means that analysed images are aligned and geometrically transformed using a computational method for determining the point-by-point correspondence between those images. Used transformation models can be divided into several classes: rigid, affine, projective and nonrigid transformation when the complexity of the transforms in each transformation is characterised by degrees of freedom. Using such transformation models, an object can be transformed by translation, rotation or scaling. However, the key part of the registration procedure is the actual transformation parameters estimation. For this estimation, there exist many algorithms that can be divided into several classes: intensity-based methods [51], feature extraction based methods [52] or frequency domain methods [53]. However, functionality of those methods is dependent on the quality of input data, mainly in terms of noise and contrast of prominent structures and their overall detectability, which is hardly achievable especially for biological samples.

Therefore, this process is addressed in this work using developed samples holder with the reference area (for more details see section 3.5.2), whose detectability is guaranteed wide range of acquisition parameters due its' high density. This area specifically reduces the problem of volume registration to finding and alignment of a reference point within both acquired data, which increases the accuracy and speed of the whole image registration procedure over standard image registration methods. Within the proposed procedure, projection data are aligned using fully automatic image registration process based on detection of reference area within the developed sample's holder after DTCT acquisition. This procedure was used included in the DTCT workflow due to already mentioned possibility of sample's movement and rotational stage instability during the acquisition process, which cannot be corrected after tomographic reconstruction. Therefore, the registration of projection data prior to tomographic reconstruction enables their better alignment. Following the results from the section 3.5.1, the rotational movement of the stage is considered stable and consistent (perceived only in terms of rotational movement not stage stability), and the tilt of the sample is also considered constant, which reduces the problem of DTCT projection data registration to two parameters – vertical and horizontal displacement. The registration process consist of detecting the centre of reference fiducial in each Cu and Mo data projections, determining the ideal sinusoidal curse of this point within the Cu data acquisition (corresponding to the proposed procedure for rotational stage instability and inaccuracy correction presented in section 3.5.2.1), and then aligning the individual projections of both datasets so they match the estimated ideal course. This is done using b-spline interpolation to reach the sub-pixel precision (see Figure 45).

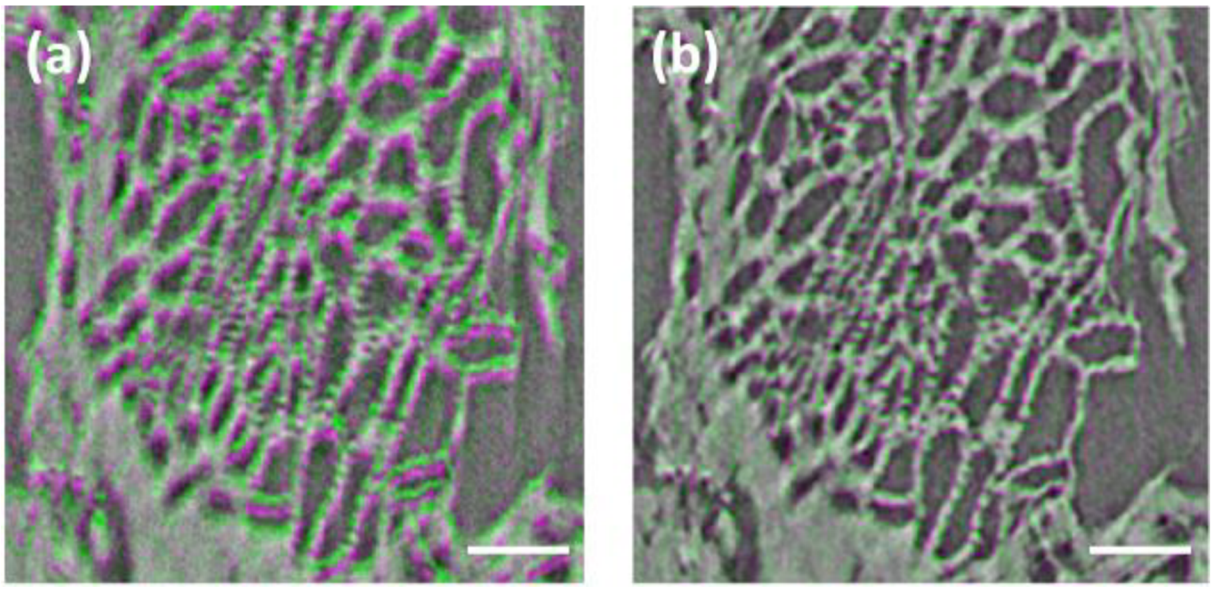


*Figure 45: Results of proposed DTCT data registration procedure demonstrated on DTCT data of cumin seed scanned using Rigaku nano3DX device – for visualization purposes CT slices of both Cu and Mo target data were overlapped and presence of green and purple colours indicates level of their misalignment: a) Original data; b) Aligned data. Scale bar: 100 µm.*

# 5 Quantitative analysis of CT data

The most widely used perception of quantitative computed tomography, is related to the quantitative characterization of acquired CT data. In scope of this thesis, two novel quantitative analysis methods were developed and published, and their main features and results relevant in scope of this work, are present in following text. For more details refer to the original works [54] and [55].

## 5.1 CT analysis of additive manufactured samples

X-ray computed tomography is a common method for non-destructive testing and analysis. One major application of CT is the porosity detection and quantification. This analysis is specifically important for metallic parts made by selective laser melting (SLM) technology, which are evaluated for internal porosity, when the presence of internal defects has a negative effect on their fatigue life and ultimate tensile strength (UTS) [54]. Therefore, one of the major challenges in the SLM production process is minimizing the internal porosity inside the manufactured parts. Currently, there are several possible ways to measure porosity, such as mass measurement, Archimedes method, metallography, and X-ray computed tomography. All these methods are based on different principles and incomparable in terms of getting the absolute value of the porosity for one sample [54]. Metallography is the most frequently used image-based method for the porosity analysis of SLM parts thanks to a high resolution that can be achieved and also to the fact that light or electron microscopes are accessible [54]. The weaknesses of this method are the necessary sample's surface preparation and also the fact that the evaluation of the total porosity (i.e., for the whole sample volume) as a mean value of several surfaces measurements, when the number and selection of the evaluated planar section have the major impact on the final porosity result. In comparison to metallography, CT technique has some undisputed benefits. CT technique enables to visualize the inner structure non-destructively, in three dimensions, and at one measurement process [54].

The porosity analysis using CT data is commonly based on pores segmentation by means of global thresholding, which has a major impact on results of the analysis [56]. Specifically, the threshold selection becomes a critical point influencing the result. In practice, threshold can be determined either automatically or manually by an operation. However, the automatic threshold selection depends on a material inner structure and also quality of input data. But the manual threshold selection is highly subjective and gives variable results depending on the operator's experience, knowledge of the studied sample and even on the way CT data are displayed on an ordinary monitor. This operator related variability brings a significant uncertainty to the porosity measurement in terms of the SLM production quality evaluation and was further studied in our work. These aspects rule out any trustworthy results coming from a comparative porosity measurement of two samples scanned in different laboratories and also of two samples measured in different times within one CT system. [54]

To overcome these issues, a new porosity analysis procedure on CT data was designed. It is based on a correlation with the metallographic image of the sample surface which is obtained with higher resolution and pore contrast than the CT data. For this reason, the metallographic image is used as a reference image for the threshold selection. The procedure respects the given voxel resolution of CT data, and it is objective and reproducible. These properties enable a comparative porosity analysis of samples from separate measurements which are even performed on different CT machines. The proposed procedure was tested on a sample of aluminium alloy including all possible defects related to additive manufacturing. Based on a comparison with manual and standard automatic techniques, the proposed method showed a reliable determination of pores and a good agreement with the value determined by a group of experienced CT users. [54]

### 5.1.1 Reproducible porosity analysis (RPA)

The proposed procedure was designed with a respect to the crucial points of tomographic data processing. These aspects are the user independence, correct pores' segmentation, reproducibility, and adaptation for different voxel resolutions. The workflow of proposed procedure is described in Figure 46. The method is based on a correlation between CT data and metallographic data. The characteristics of metallographic analysis using microscopy are high resolution and easy pores segmentation. Therefore, the metallographic analysis complies with the task of the reference and the calibration for the CT porosity analysis. [54]

The correlation of these techniques is based on an alignment of corresponding images, i.e., a light microscopic image of the sample surface (LM image) and a CT top cross-section (CT image). Getting such corresponding images can be guaranteed only when the CT measurement is performed on a sample whose surface was already analysed by metallography. The acquisition of LM and CT images is followed by an image registration which aims to unify both images to the same size and orientation. This is done by a geometric transformation of LM image because the LM reaches higher resolution than micro-CT does. The transformation including the scaling, rotation and translation is determined automatically by the phase correlation [57]. Then the LM image and CT data are trimmed around the sample centre to avoid distorted areas of the image caused by a mechanical preparation of the sample surface. Moreover, removing these edges simplifies the porosity calculation as there is no need to distinguish the background pixels (outer sample space) from the pore's pixels presented by the same grey values. [54]

The threshold selection is implemented on these registered corresponding images. The reference porosity value is determined from LM image using global thresholding with Otsu's automatic threshold selection [45] for pores' segmentation. This method works reliably on LM images because of a high pores/material contrast. The reference porosity value is subsequently used for the selection of an optimal threshold value for CT data. This selection is realized using a brute-force search during the optimization process. In this process, the porosity from CT image is calculated for a series of threshold values (from minimum to maximum CT image intensity value). A criterion function is expressed for each porosity value. This function is defined as Euclidean distance from the reference LM image porosity value and the CT image porosity value for a particular threshold. The optimal threshold for global thresholding of CT data is then selected as a threshold where the criterion function reaches its minimum. This threshold is subsequently applied to the trimmed CT data volume using the global thresholding (see Figure 47) and porosity value is then calculated. [54]

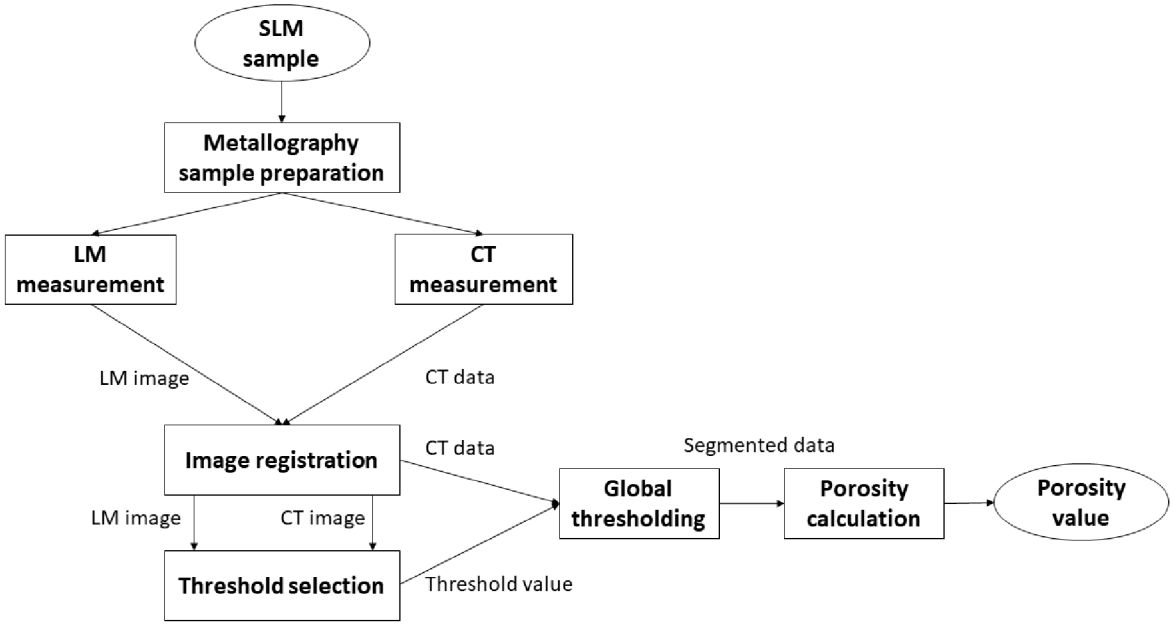


*Figure 46: Scheme of proposed reproducible porosity analysis procedure. [54].*

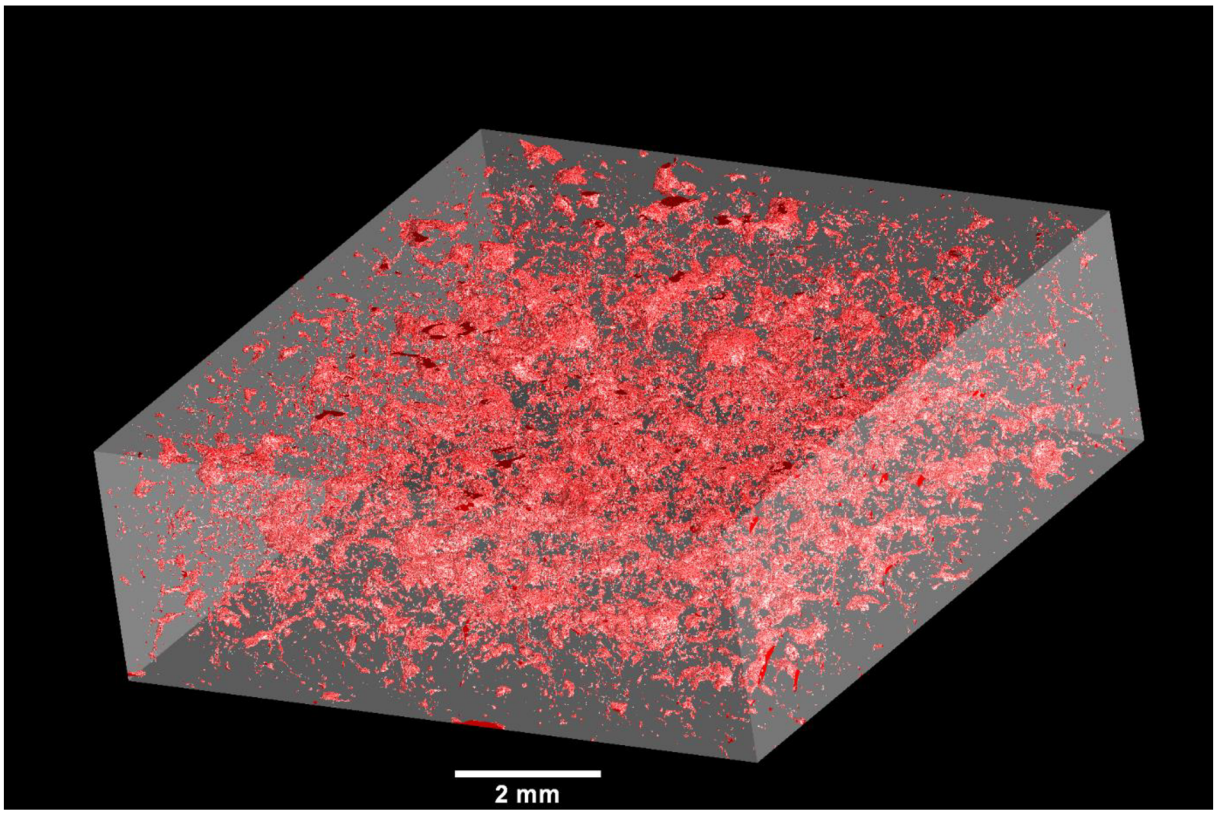


*Figure 47: 3D pores distribution in analysed volume of aluminium alloy sample – achieved from CT data with use of proposed porosity analysis procedure. [54]*

## 5.2 CT analysis of a mouse model for Alagille syndrome

The correct three-dimensional (3D) architecture of lumenized structures in our bodies is essential for function and our health [55]. The cardiovascular system, lungs, kidneys, liver, and other organs depend on precisely patterned tubular networks, when several diseases are caused by, or result in, alterations in the 3D architecture of those lumenized structures [55]. Precisely defining 3D architecture of healthy and diseased organs is a fundamental aspect of biology, and improved imaging methods would allow stricter characterization of animal models for human diseases. However, visualization of biological tubes in 3D is very challenging task, which has been until now restricted by a lack of adequate tools. Traditional microscopic imaging of anatomy structures enables only 2D visualization, using slices of tissue. This approach shows the cross-sections of tubes, but not how the ducts connect and interact [55]. An alternative is to use CT technique, which is, however, limited by poor contrast for soft tissues.

To overcome this, a new technique was developed called double resin casting micro computed tomography (DUCT) [55]. The approach involves making casts of biological tube systems using two types of radiopaque resin that show up differently under X-rays. Regarding instrumentation, the DUCT pipeline is not restricted to specific CT systems or acquisitions parameters, therefore samples can be imaged on any CT device with sufficient spatial resolution to study selected samples and their morphology. The new technique was tested on a mouse model of Alagille syndrome [58]. One resin was injected into the bile ducts, and another into the blood vessels, which enabled to reconstruct both trees digitally in 3D by means of CT and subsequent data segmentation (see Figure 48). For more details about developed pipeline for performing double resin casting microCT, please refer to the original work [55] or to the published protocol [59].

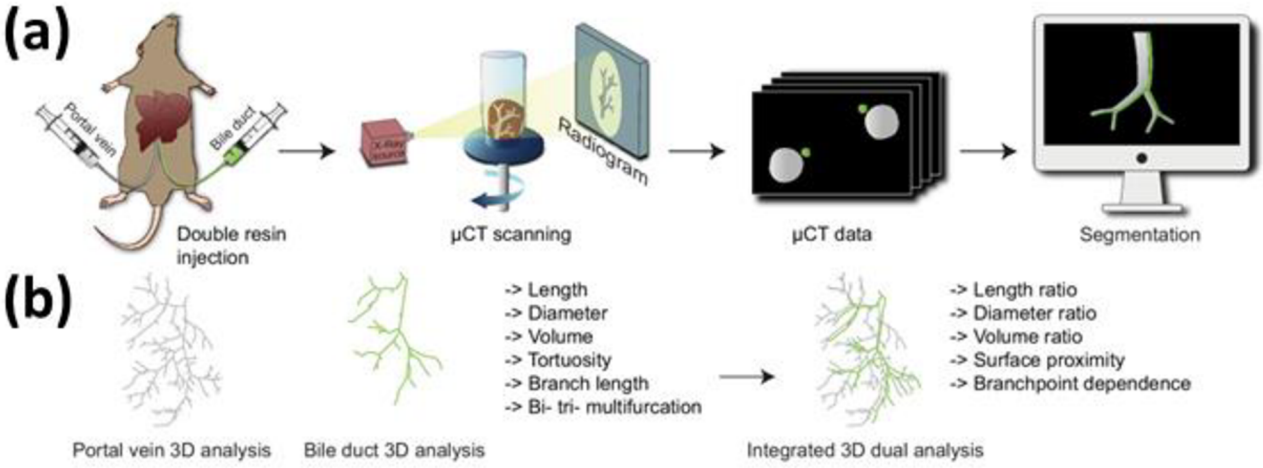


*Figure 48: Schematical diagram of: a) DUCT pipeline - resin injection into two systems (portal venous and biliary), microCT of the organ, or individual lobes, and segmentation of CT data into 3D binary masks. b) quantitative analysis pipeline – creating 3D skeletons from the binary masks and quantifying architectural parameters in individual or combined systems. [55]*

### 5.2.1 Quantitative analysis of 3D models of tubular systems

To extend possibilities of the DUCT technique, a new analysis pipeline was developed in scope of this thesis. This pipeline was as well included in the original work [55] and its' purpose was to enable quantitative assessment of 3D models resulting from DUCT procedure. This allowed to study architectural mechanisms of two tubular networks (i.e., revealing their length, volume, branching, and interactions) and together with DUCT could serve as a standard for whole organ analysis in animal models (see Figure 48), and can be further adapted for specific applications. The quantitative analysis pipeline was implemented in Matlab® programming environment and is freely available at: [60].

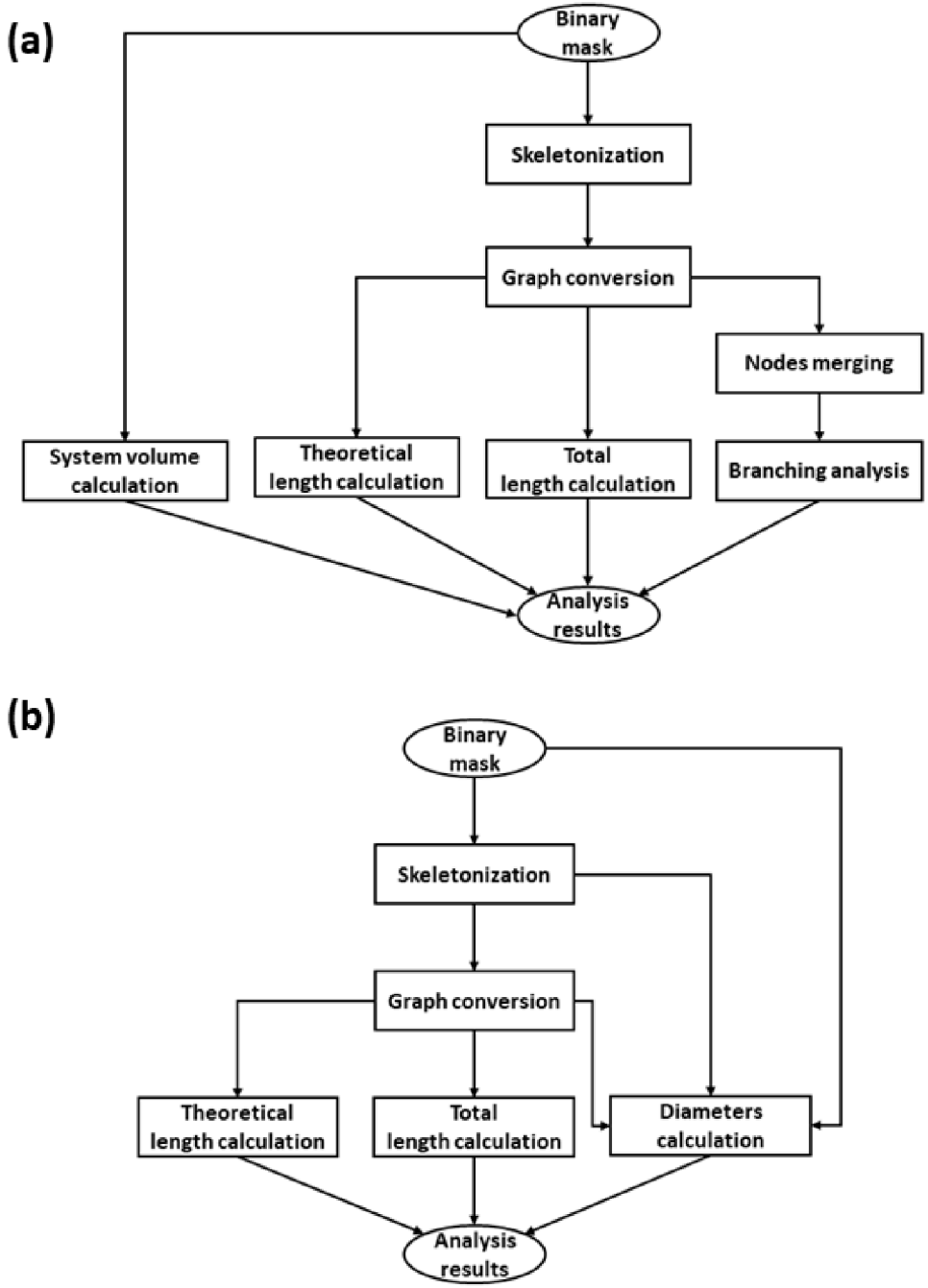


*Figure 49: Scheme of proposed algorithms for quantitative analysis of tubular systems: a) Whole system analysis algorithm; b) Main branch analysis algorithm. [55]*

Developed algorithm is compatible with 3D binary masks resulting from the DUCT method and was originally designed for morphological analysis of liver tubular system, i.e., bile duct (BD) and portal vein (PV). As result of DUCT, two separate masks of BD and PV system were generated, and the subsequent quantitative analysis was divided in two independent parts. First, the analysis of the entire portal vein and biliary system and second, analysis of the corresponding main branch (i.e., the longest branch) of each system. For detailed analysis and comparison of the whole system versus only the main branch, two algorithms were developed (see Figure 49). They differ in the input data and the evaluated parameters. [55]

However, the first step in both algorithms is to create a 3D skeleton of the input binary mask. The 3D skeleton was derived using the homotopic thinning algorithm originally described in the work by Lee et. al, [61] and subsequently optimized by Kerschnitzki et. al. [62]. Using available Matlab implementation of this algorithm [63], resulting network graph is formed by nodes and links between them, which are subject of further quantitative analysis:

- **Branching analysis**: analysing not only the branching itself but also the distance between BD and PV branching points. This parameter was calculated using 3D Euclidean distances between the BD branching points and the nearest branching point from PV system (see Figure 50). The data is represented as cumulative sum of percentage of BD branching point at a given distances between BD and PV branching points. The number of bi-furcations (i.e., one input and two outputs), tri-furcations (i.e., one input and three outputs) and quadri- and more-furcations (one input and more than three outputs), were assessed based on binary mask skeleton nodes that were divided into endpoints and branching points (see Figure 52). Branching points closer than 0.2 mm (this threshold value was derived based on visual assessment and knowledge of the system) were merged and further represented by one node. [55]

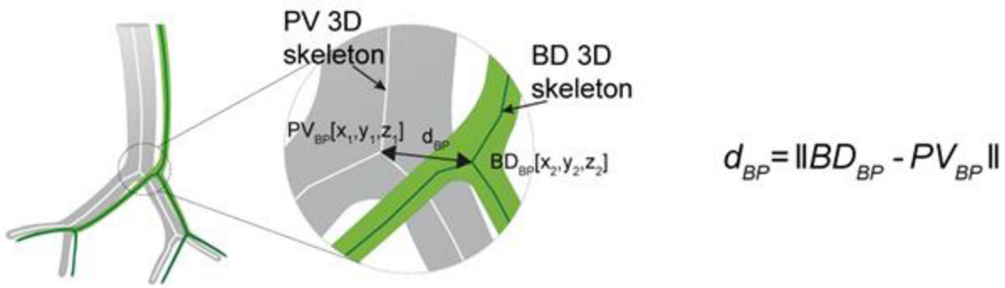


*Figure 50: Scheme representing BD to PV branch point analysis. $PV_{BD}$ = PV branch point, $BD_{BD}$ = BD branch point, $d_{BP}$ = Euclidean 3D distance between branch points. [55]*

- **Gap analysis between BD and PV**: to evaluate the gap between BD and PV the surface distances were calculated for each BD skeleton point by detecting the nearest PV skeleton point and connecting the two points with a line and measuring the non-resin area on this line (zero area in the input binary masks, see Figure 51). Surface distance was then calculated using 3D Euclidean distance between the detected non-resin voxel coordinates. [55]

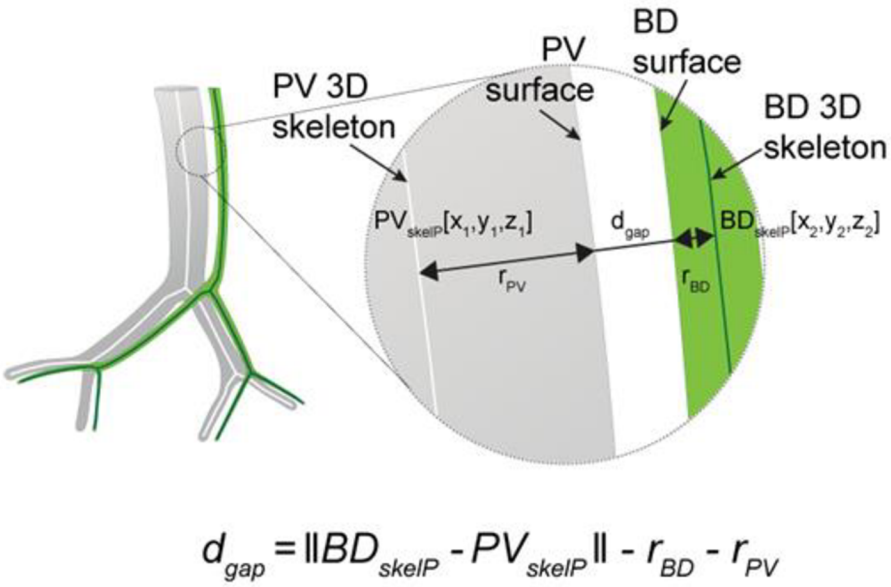


$$d_{gap} = \|BD_{skelP} - PV_{skelP}\| - r_{BD} - r_{PV}$$

*Figure 51: Scheme of BD to PV surface distance analysis. $PV_{skelP}$ = single point on PV skeleton, $BD_{skelP}$ = single point on BD skeleton, $r_{PV}$ = radius of PV at $PV_{skelP}$ (i.e., minimal distance from $PV_{skelP}$ to PV surface), $r_{BD}$ = radius of BD at $BD_{skelP}$ (i.e. minimal distance from $BD_{skelP}$ to BD surface), $d_{gap}$ = gap distance, which is derived by subtracting the radii from the skeleton to skeleton distance. [55]*

- **Tortuosity measurements: t**o quantify length and tortuosity, total (i.e., curved) and theoretical (i.e., chord) lengths were measured for the whole system length and for the corresponding main branch. The curved length was defined as a cumulative sum of 3D Euclidean distances between neighbouring graph points (i.e., links forming points) multiplied by voxel size. The chord length was defined as cumulative sum of 3D Euclidean distances between neighbouring nodes multiplied by voxel size. The chord length therefore reflects system length where any nodes are connected by links with the shortest possible length. To analyse the relationship between BD and PV a length of the BD was divided by a PV length (curved or chord). Tortuosity was calculated as curved length divided by chord length of the same system and distributed into regions based on the generation number as previously described. Tortuosity was assessed in %, as BD and PV are not straight lines the actual tortuosity measurements were subtracted by 100% (i.e., perfectly straight line). [55]
- **Volume analysis:** total system volume was calculated by multiplying a number of voxels representing PV or BD by volume of one voxel. The relationship between BD and PV volumes was addressed by dividing the BD volume by PV volume. [55]
- **Diameter measurements:** the main branch diameter was calculated every 1.5 mm (this value was derived based on visual assessment and knowledge of the system) along the total length of the main branch. The radius was defined as the minimal distance from the skeleton to the boundary of segmented area in the input binary mask (i.e., border between background and area of interest). This boundary was calculated using a two-step procedure. In the first step, the input map was eroded using a 3D spherical shaped structural element with one pixel radius. Subsequently, the eroded area was subtracted from the original binary mask. This resulted in a binary mask representing the boundary between the background and the area of

interest. One radius value at a given skeleton point was then expressed as the minimum distance from that point to the mask boundary. This was calculated, using the minimal value search in the intersection of the boundary mask and the distance map from that point. The distance map from a given skeleton point was calculated as 3D Euclidean distance of the spatial coordinates. Subsequently the diameter value was calculated as the minimum distance to the boundary area multiplied by 2. To avoid any misrepresentation, the one final diameter value at a given point (every 1.5 mm of branch length) was calculated as a mean value of a diameter at that point and diameters at four neighbouring points (two on each side). [55]

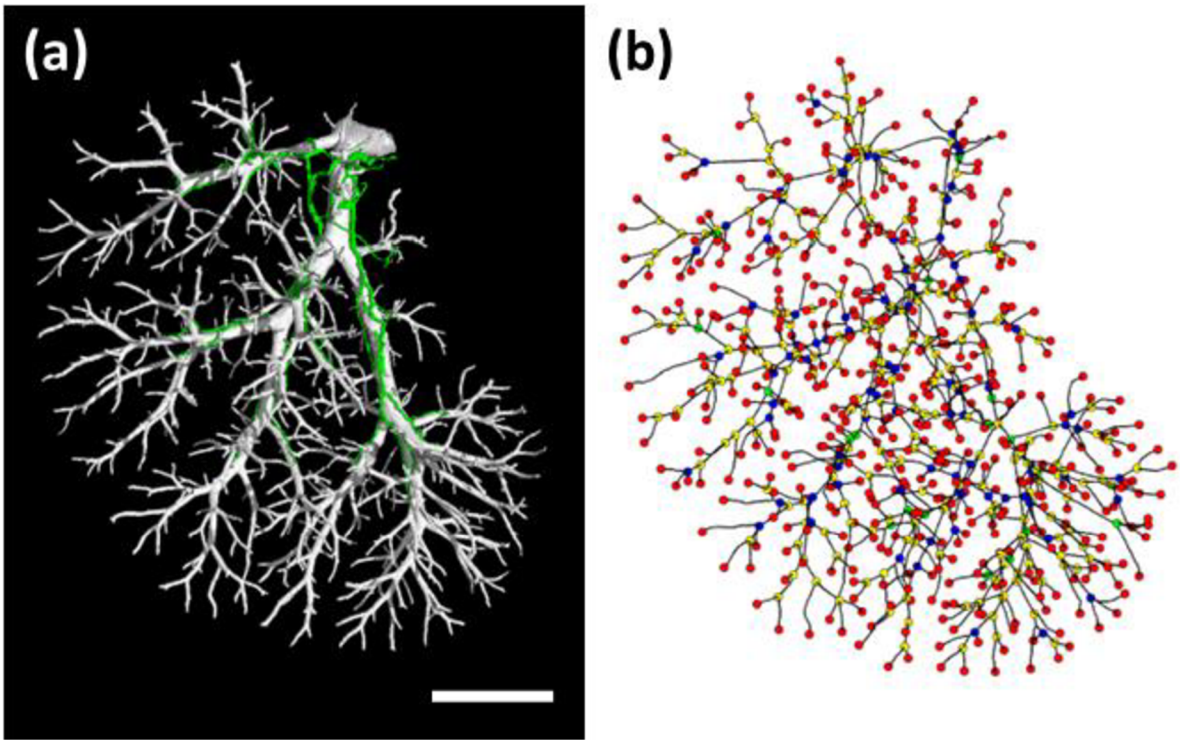


*Figure 52: Visual results of DUCT and quantitative analysis pipelines demonstrated on mouse liver sample: a) 3D visualization of segmentation and identification results: bile duct (green area) and portal vein (white area); b) Visualization of the truncation analysis results for portal vein system; red circles = endpoints, yellow circles = bi-furcations, blue circles = tri-furcations, green circles = quadri- and more- furcations, black lines represent branches between nodes; scale bar: 4 mm.*

# 6 Conclusion

The topic of this thesis reflects the current need of researchers from various R&D fields to have the possibly of utilizing a 3D non-destructive imaging method with sufficient spatial resolution, that will provide them information that would be solely dependent on sample's properties and applicable for further quantitative analysis. X-ray computed tomography can, in general, fulfil all those demands, but especially aiming for higher spatial resolution and implementation of advanced CT techniques (e.g., 4D CT or spectral CT), brings strict requirements for both the hardware and the software. In sphere of submicron CT, the possibility of acquisition of undistorted CT data and its' further quantitative analysis is still highly limited by various technological aspects and lack of dedicated methodologies and correction solutions.

Objectives of this work were dealing with all the aspects of quantitative CT with specific focus on a laboratory-based submicron CT system Rigaku nano3DX. Firstly, the optimal reconstruction process for submicron CT data was found, involving the use of analytical reconstruction method with optimized settings respecting the achievable spatial resolution and data quality. Then the technological limitations of submicron CT acquisition using this device were assessed. Focusing on the technology-based tomographic artifacts, their individual causes and properties were studied, and optimal reduction strategies were proposed. Some of the most prominent artifacts of this class – noise and ring artifacts, are found to be related to the detection system itself. Therefore, three detector types were assessed for the task of submicron CT acquisition and compared in terms of quality and accuracy of acquired data, and the results were further incorporated into proposed reduction procedures. Specifically, novel procedures were developed for ring artifacts reduction and denoising of all the noise types present in Rigaku nano3DX data. The denoising solution, specifically, involves new algorithms for random valued impulse noise reduction and noise absolute deviation estimation, and practically tested state-of-the-art methods for shot noise reduction. Dedicated solution was also developed for the instability and inaccuracy of the rotational stage during submicron CT acquisition. This development involved also studying this instability in terms of thermal dependence and also in context of commercial lab-based CT systems.

Dealing with the spectral imaging and its's implementation for submicron CT data acquisition using Rigaku nano3DX, dedicated acquisition and DTCT data registration methodologies were developed. In terms of the DTCT data acquisition, novel procedure was defined for selecting the optimal acquisition parameters using the noise properties as evaluation metric. For the task of DTCT data registration, developed sample's holder with reference area was utilized resulting into fully automatic, robust, and precise solution. For the quantitative analysis of CT data, two novel methods were developed. One was specifically designed for porosity analysis of additive manufactured samples with a respect to the crucial points of tomographic data processing, making it objective and reproducible. Second method was specifically designed for quantitative assessment of 3D models of biological tubular systems and was practically tested on a mouse model of Alagille syndrome.

Exploiting the results of this work, a multi-purpose solution in form of QCT can be achieved that allows to reduce the limits of current CT technology and to fulfil requirements of R&D and basic research from various fields e.g., materials' development, tissue engineering, pharmacy, and others. In those filed, there is, especially, a need to have the possibility of utilizing a 3D, nondestructive, high-resolution imaging method, that will provide information that is solely dependent on samples' properties and can be used for further quantitative analysis.

# References


[1] MARTZ, Harry E., Clint M. LOGAN, Daniel J. SCHNEBERK a Peter J. SHULL. *X-Ray Imaging: Fundamentals, Industrial Techniques and Applications*. 1st Edition. CRC Press: Boca Raton: Taylor & Francis, 2017. ISBN 9780849397721.

[2] DE CHIFFRE, L., S. CARMIGNATO, J.-P. KRUTH, R. SCHMITT a A. WECKENMANN. Industrial applications of computed tomography. *CIRP Annals*. 2014, **63**(2), 655-677. ISSN 00078506. Dostupné z: doi:10.1016/j.cirp.2014.05.011

[3] STOCK, Stuart. *Microcomputed tomography: methodology and applications*. Boca Raton: CRC Press, 2009. ISBN 978-142-0058-765.

[4] KRAEMER, Alexandra a Gisela LANZA. Assessment of the Measurement Procedure for Dimensional Metrology with X-ray Computed Tomography. *Procedia CIRP*. 2016, **43**, 362-367. ISSN 22128271. Dostupné z: doi:10.1016/j.procir.2016.02.018

[5] NGUYEN THI, Thanh, Mizuki MORIOKA, Atsushi YOKOYAMA, Senji HAMANAKA, Katsuhisa YAMASHITA a Chisato NONOMURA. Measurement of fiber orientation distribution in injection-molded short-glass-fiber composites using X-ray computed tomography. *Journal of Materials Processing Technology*. 2015, **219**, 1-9. ISSN 09240136. Dostupné z: doi:10.1016/j.jmatprotec.2014.11.048

[6] DU PLESSIS, Anton, Babatunde OLAWUYI, William BOSHOFF a Stephan LE ROUX. Simple and fast porosity analysis of concrete using X-ray computed tomography. *Materials and Structures*. 2016, **49**(1-2), 553-562. ISSN 1359-5997. Dostupné z: doi:10.1617/s11527-014-0519-9

[7] *Phoenix v|tome|x L – versatile and flexible CT system*. Germany, 2019. Dostupné také z: https://www.industrial.ai/sites/g/files/cozyhq596/files/acquiadam_assets/geit_31205_flyer_vtomex_l_en_1213.pdf

[8] KINGSTON, Andrew M., Glenn R. MYERS, Shane J. LATHAM, Benoit RECUR, Heyang LI a Adrian P. SHEPPARD. Space-Filling X-Ray Source Trajectories for Efficient Scanning in Large-Angle Cone-Beam Computed Tomography. *IEEE Transactions on Computational Imaging*. 2018, **4**(3), 447-458. ISSN 2333-9403. Dostupné z: doi:10.1109/TCI.2018.2841202

[9] RUEDEN, Curtis T., Johannes SCHINDELIN, Mark C. HINER, Barry E. DEZONIA, Alison E. WALTER, Ellen T. ARENA a Kevin W. ELICEIRI. ImageJ2: ImageJ for the next generation of scientific image

data. *BMC Bioinformatics*. 2017, **18**(1). ISSN 1471-2105. Dostupné z: doi:10.1186/s12859-017-1934-z

[10] VAN AARLE, Wim, Willem PALENSTIJN, Jeroen CANT et al. Fast and flexible X-ray tomography using the ASTRA toolbox. *Optics Express*. 2016, **24**(22), 25129-25147. ISSN 1094-4087. Dostupné z: doi:10.1364/OE.24.025129

[11] KRAEMER, Alexandra, Ekaterina KOVACHEVA a Gisela LANZA. *Projection based evaluation of CT image quality in dimensional metrology*. In: . Digital Industrial Radiology and Computed Tomography (DIR 2015). Belgium, Ghent, 2015.

[12] *IEC 62220-1:2003(E): Medical electrical equipment – Characteristics of digital X-ray imaging devices – Part 1: Determination of the detective quantum efficiency*. Switzerland: International Electrotechnical Commission, 2003.

[13] *ASTM E1695-95: Standard Test Method for Measurement of Computed Tomography (CT) System Performance*. West Conshohocken, PA,: ASTM International, 2013.

[14] ŠALPLACHTA, Jakub. *Kvantitativní počítačová tomografie* [online]. Brno, 2019 [cit. 2021-09-08]. Dostupné z: https://www.vutbr.cz/studenti/zav-prace/detail/123252. Pojednání. Vysoké učení technické v Brně, Středoevropský technologický institut VUT. Vedoucí práce Jozef Kaiser.

[15] WANG, Z., A.C. BOVIK, H.R. SHEIKH a E.P. SIMONCELLI. Image Quality Assessment: From Error Visibility to Structural Similarity. *IEEE Transactions on Image Processing*. 2004, **13**(4), 600-612. ISSN 1057-7149. Dostupné z: doi:10.1109/TIP.2003.819861

[16] ŠALPLACHTA, Jakub, Tomáš ZIKMUND, Martin HORVÁTH, Yoshihiro TAKEDA, Kazuhiko OMOTE, Ladislav PÍNA a Jozef KAISER. CCD and scientific-CMOS detectors for submicron laboratory based X-ray Computed tomography. In: *9th Conference on Industrial Computed Tomography (iCT) 2019, 13-15 Feb, Padova, Italy (iCT 2019)*. The e-Journal of Nondestructive Testing, 2019. ISSN 1435-4934.

[17] *Rigaku Corporation: Compact two-dimensional CC detector* [online]. [cit. 2019-08-21]. Dostupné z: https://www.rigaku.com/en/products/detectors/micron,

[18] *Rigaku Corporation: Compact two-dimensional sCMOS detector* [online]. [cit. 2019-08-21]. Dostupné z: https://www.rigaku.com/en/products/detectors/micron-cmos

[19] SALPLACHTA, Jakub, Tomas ZIKMUND a Jozef KAISER. DENOISING APPROACH FOR HIGH-RESOLUTION COMPUTED TOMOGRAPHY DATA. In: *IADIS International Conference Computer*

*Graphics, Visualization, Computer Vision and Image Processing 2018 (part of MCCSIS 2018)*. Spain: IADIS, 2018, s. 439-441. ISBN 978-989-8533-79-1.

[20] IMMERKæR, John. Fast Noise Variance Estimation. *Computer Vision and Image Understanding*. 1996, **64**(2), 300-302. ISSN 10773142. Dostupné z: doi:10.1006/cviu.1996.0060

[21] SHEN-CHUAN TAI, a SHIH-MING YANG. A fast method for image noise estimation using Laplacian operator and adaptive edge detection. In: *2008 3rd International Symposium on Communications, Control and Signal Processing*. IEEE, 2008, s. 1077-1081. ISBN 978-1-4244-1687-5. Dostupné z: doi:10.1109/ISCCSP.2008.4537384

[22] HUANG, T., G. YANG a G. TANG. A fast two-dimensional median filtering algorithm. *IEEE Transactions on Acoustics, Speech, and Signal Processing*. 1979, **27**(1), 13-18. ISSN 0096-3518. Dostupné z: doi:10.1109/TASSP.1979.1163188

[23] HWANG, H. a R.A. HADDAD. Adaptive median filters: new algorithms and results. *IEEE Transactions on Image Processing*. 1995, **4**(4), 499-502. ISSN 10577149. Dostupné z: doi:10.1109/83.370679

[24] VERMA, Kesari, Bikesh Kumar SINGH a A.S. THOKE. An Enhancement in Adaptive Median Filter for Edge Preservation. *Procedia Computer Science*. 2015, **48**, 29-36. ISSN 18770509. Dostupné z: doi:10.1016/j.procs.2015.04.106

[25] SHRESTHA, Suman. Image Denoising Using New Adaptive Based Median Filter. *Signal & Image Processing : An International Journal (SIPIJ)*. 2014, **5**(4), 1-13. ISSN 22293922. Dostupné z: doi:10.5121/sipij.2014.5401

[26] LIN YIN, , RUIKANG YANG, M. GABBOUJ a Y. NEUVO. Weighted median filters: a tutorial. *IEEE Transactions on Circuits and Systems II: Analog and Digital Signal Processing*. 1996, **43**(3), 157-192. ISSN 10577130. Dostupné z: doi:10.1109/82.486465

[27] KHAN, Sajid a Dong-Ho LEE. An adaptive dynamically weighted median filter for impulse noise removal. *EURASIP Journal on Advances in Signal Processing*. 2017, **2017**(1). ISSN 1687-6180. Dostupné z: doi:10.1186/s13634-017-0502-z

[28] POK, G. a JYH-CHARN LIU. Decision-based median filter improved by predictions. In: *Proceedings 1999 International Conference on Image Processing (Cat. 99CH36348)*. IEEE, 1999, 410-413 vol.2. ISBN 0-7803-5467-2. Dostupné z: doi:10.1109/ICIP.1999.822928

[29] SAMANTARAY, Aswini Kumar a Priyanka MALLICK. Decision Based Adaptive Neighborhood Median Filter. *Procedia Computer Science*. 2015, **48**, 222-227. ISSN 18770509. Dostupné z: doi:10.1016/j.procs.2015.04.174

[30] ARAKAWA, Kaoru. Median filter based on fuzzy rules and its application to image restoration. *Fuzzy Sets and Systems*. 1996, **77**(1), 3-13. ISSN 01650114. Dostupné z: doi:10.1016/0165-0114(95)00122-0

[31] ZHOU, Yan, Quan-hua TANG a Wei-dong JIN. Adaptive Fuzzy Median Filter for Images Corrupted by Impulse Noise. In: *2008 Congress on Image and Signal Processing*. IEEE, 2008, s. 265-269. ISBN 978-0-7695-3119-9. Dostupné z: doi:10.1109/CISP.2008.231

[32] TOH, K.K.V. a N.A.M. ISA. Noise Adaptive Fuzzy Switching Median Filter for Salt-and-Pepper Noise Reduction. *IEEE Signal Processing Letters*. 2010, **17**(3), 281-284. ISSN 1070-9908. Dostupné z: doi:10.1109/LSP.2009.2038769

[33] ZHOU WANG, a D. ZHANG. Progressive switching median filter for the removal of impulse noise from highly corrupted images. *IEEE Transactions on Circuits and Systems II: Analog and Digital Signal Processing*. 1999, **46**(1), 78-80. ISSN 10577130. Dostupné z: doi:10.1109/82.749102

[34] GARNETT, R., T. HUEGERICH, C. CHUI a WENJIE HE. A universal noise removal algorithm with an impulse detector. *IEEE Transactions on Image Processing*. 2005, **14**(11), 1747-1754. ISSN 1057-7149. Dostupné z: doi:10.1109/TIP.2005.857261

[35] WANG, Gaihua, Dehua LI, Weimin PAN a Zhaoxiang ZANG. Modified switching median filter for impulse noise removal. *Signal Processing*. 2010, **90**(12), 3213-3218. ISSN 01651684. Dostupné z: doi:10.1016/j.sigpro.2010.05.026

[36] WANG, Z., A.C. BOVIK, H.R. SHEIKH a E.P. SIMONCELLI. Image Quality Assessment: From Error Visibility to Structural Similarity. *IEEE Transactions on Image Processing*. 2004, **13**(4), 600-612. ISSN 1057-7149. Dostupné z: doi:10.1109/TIP.2003.819861

[37] HADDAD, R.A. a A.N. AKANSU. A class of fast Gaussian binomial filters for speech and image processing. *IEEE Transactions on Signal Processing*. 1991, **39**(3), 723-727. ISSN 1053587X. Dostupné z: doi:10.1109/78.80892

[38] COUPE, P., P. YGER, S. PRIMA, P. HELLIER, C. KERVRANN a C. BARILLOT. An Optimized Blockwise Nonlocal Means Denoising Filter for 3-D Magnetic Resonance Images. *IEEE Transactions on Medical Imaging*. 2008, **27**(4), 425-441. ISSN 0278-0062. Dostupné z: doi:10.1109/TMI.2007.906087

[39] COUPÉ, Pierrick, Martin MUNZ, Jose V. MANJÓN, Edward S. RUTHAZER a D. LOUIS COLLINS. A CANDLE for a deeper in vivo insight. *Medical Image Analysis*. 2012, **16**(4), 849-864. ISSN 13618415. Dostupné z: doi:10.1016/j.media.2012.01.002

[40] ŠALPLACHTA, Jakub, Tomáš ZIKMUND, Marek ZEMEK, Adam BŘÍNEK, Yoshihiro TAKEDA, Kazuhiko OMOTE a Jozef KAISER. Complete Ring Artifacts Reduction Procedure for Lab-Based X-ray Nano CT Systems. *Sensors*. 2021, **21**(1), 1-20. ISSN 1424-8220. Dostupné z: doi:10.3390/s21010238

[41] XU, Li, Qiong YAN, Yang XIA a Jiaya JIA. Structure extraction from texture via relative total variation. *ACM Transactions on Graphics*. 2012, **31**(6). ISSN 07300301. Dostupné z: doi:10.1145/2366145.2366158

[42] MÜNCH, Beat, Pavel TRTIK, Federica MARONE a Marco STAMPANONI. Stripe and ring artifact removal with combined wavelet—Fourier filtering. *Optics Express*. 2009, **17**(10), 8567-. ISSN 1094-4087. Dostupné z: doi:10.1364/OE.17.008567

[43] ELDIB, Mohamed, Mohamed HEGAZY, Yang MUN, Myung CHO, Min CHO a Soo LEE. A Ring Artifact Correction Method: Validation by Micro-CT Imaging with Flat-Panel Detectors and a 2D Photon-Counting Detector. *Sensors*. 2017, **17**(2). ISSN 1424-8220. Dostupné z: doi:10.3390/s17020269

[44] VO, Nghia, Robert ATWOOD a Michael DRAKOPOULOS. Superior techniques for eliminating ring artifacts in X-ray micro-tomography. *Optics Express*. 2018, **26**(22), 28396-28412. ISSN 1094-4087. Dostupné z: doi:10.1364/OE.26.028396

[45] OTSU, Nobuyuki. A Threshold Selection Method from Gray-Level Histograms. *IEEE Transactions on Systems, Man, and Cybernetics*. 1979, **9**(1), 62-66. ISSN 0018-9472. Dostupné z: doi:10.1109/TSMC.1979.4310076

[46] TAUBIN, G. Estimation of planar curves, surfaces, and nonplanar space curves defined by implicit equations with applications to edge and range image segmentation. *IEEE Transactions on Pattern Analysis and Machine Intelligence*. 1991, **13**(11), 1115-1138. ISSN 01628828. Dostupné z: doi:10.1109/34.103273

[47] LEVENBERG, Kenneth. A method for the solution of certain non-linear problems in least squares. *Quarterly of Applied Mathematics*. 1944, **2**(2), 164-168. ISSN 0033-569X. Dostupné z: doi:10.1090/qam/10666

[48] CHENG, Chang-Chieh, Chia-Chi CHIEN, Hsiang-Hsin CHEN, Yeukuang HWU, Yu-Tai CHING a Oscar Deniz SUAREZ. Image Alignment for Tomography Reconstruction from Synchrotron X-Ray

Microscopic Images. *PLoS ONE*. 2014, **9**(1). ISSN 1932-6203. Dostupné z: doi:10.1371/journal.pone.0084675

[49] SODICKSON, Aaron, Abhishek KERALIYA, Bryan CZAKOWSKI, Andrew PRIMAK, Jeremy WORTMAN a Jennifer UYEDA. Dual energy CT in clinical routine: how it works and how it adds value. *Emergency Radiology*. 2020.

[50] CLAVIJO, Carolina a Norbert PELC. Image-quality optimization for dual energy computed tomography (DECT) three-material decomposition. *REVISTA INGENIERÍA BIOMÉDICA*. 2009, **3**(5), 33-42.

[51] ZITOVÁ, Barbara a Jan FLUSSER. Image registration methods: a survey. *Image and Vision Computing*. 2003, **21**(11), 977-1000. ISSN 02628856. Dostupné z: doi:10.1016/S0262-8856(03)00137-9

[52] HAN, Renmin, Fa ZHANG, Xiaohua WAN, Jose-Jesus FERNÁNDEZ, Fei SUN a Zhiyong LIU. A marker-free automatic alignment method based on scale-invariant features. *Journal of Structural Biology*. 2014, **186**(1), 167-180. ISSN 10478477. Dostupné z: doi:10.1016/j.jsb.2014.02.011

[53] REDDY, B.S. a B.N. CHATTERJI. An FFT-based technique for translation, rotation, and scale-invariant image registration. *IEEE Transactions on Image Processing*. **5**(8), 1266-1271. ISSN 10577149. Dostupné z: doi:10.1109/83.506761

[54] ZIKMUND, Tomáš, Jakub ŠALPLACHTA, Aneta ZATOČILOVÁ et al. Computed tomography based procedure for reproducible porosity measurement of additive manufactured samples. *NDT & E International*. 2019, **103**, 111-118. ISSN 09638695. Dostupné z: doi:10.1016/j.ndteint.2019.02.008

[55] HANKEOVA, Simona, Jakub SALPLACHTA, Tomas ZIKMUND et al. DUCT reveals architectural mechanisms contributing to bile duct recovery in a mouse model for Alagille syndrome. *ELife*. 2021, **10**. ISSN 2050-084X. Dostupné z: doi:10.7554/eLife.60916

[56] JAQUES, Victory A J, Anton Du PLESSIS, Marek ZEMEK, Jakub ŠALPLACHTA, Zuzana STUBIANOVÁ, Tomáš ZIKMUND a Jozef KAISER. Review of porosity uncertainty estimation methods in computed tomography dataset. *Measurement Science and Technology*. 2021, **32**(12). ISSN 0957-0233. Dostupné z: doi:10.1088/1361-6501/ac1b40

[57] REDDY, B.S. a B.N. CHATTERJI. An FFT-based technique for translation, rotation, and scale-invariant image registration. *IEEE Transactions on Image Processing*. 1996, **5**(8), 1266-1271. ISSN 10577149. Dostupné z: doi:10.1109/83.506761

[58] ANDERSSON, Emma R., Indira V. CHIVUKULA, Simona HANKEOVA et al. Mouse Model of Alagille Syndrome and Mechanisms of Jagged1 Missense Mutations. *Gastroenterology*. 2018, **154**(4), 1080-1095. ISSN 00165085. Dostupné z: doi:10.1053/j.gastro.2017.11.002

[59] HANKEOVA, Simona, Jakub SALPLACHTA, Noemi VAN HUL, Michaela KAVKOVA, Afshan IQBAL, Tomas ZIKMUND, Jozef KAISER a Emma R. ANDERSSON. DUCT: Double Resin Casting followed by Micro-Computed Tomography for 3D Liver Analysis. *Journal of Visualized Experiments*. 2021, (175). ISSN 1940-087X. Dostupné z: doi:10.3791/62941

[60] *DUCT: Quantitative pipeline* [online]. San Francisco: Github, 2020 [cit. 2022-09-28]. Dostupné z: https://github.com/JakubSalplachta/DUCT

[61] LEE, T.C., R.L. KASHYAP a C.N. CHU. Building Skeleton Models via 3-D Medial Surface Axis Thinning Algorithms. *CVGIP: Graphical Models and Image Processing*. 1994, **56**(6), 462-478. ISSN 10499652. Dostupné z: doi:10.1006/cgip.1994.1042

[62] KERSCHNITZKI, Michael, Philip KOLLMANNSBERGER, Manfred BURGHAMMER, Georg N DUDA, Richard WEINKAMER, Wolfgang WAGERMAIER a Peter FRATZL. Architecture of the osteocyte network correlates with bone material quality. *Journal of Bone and Mineral Research*. 2013, **28**(8), 1837-1845. ISSN 08840431. Dostupné z: doi:10.1002/jbmr.1927

[63] *Skeleton3d-matlab* [online]. San Francisco, 2017 [cit. 2022-09-28]. Dostupné z: https://github.com/phi-max/skeleton3d-matlab

[64] DAVIS, G.R a J.C ELLIOTT. X-ray microtomography scanner using time-delay integration for elimination of ring artefacts in the reconstructed image. *Nuclear Instruments and Methods in Physics Research Section A: Accelerators, Spectrometers, Detectors and Associated Equipment*. 1997, **394**(1-2), 157-162. ISSN 01689002. Dostupné z: doi:10.1016/S0168-9002(97)00566-4

[65] RAVEN, Carsten. Numerical removal of ring artifacts in microtomography. *Review of Scientific Instruments*. 1998, **69**(8), 2978-2980. ISSN 0034-6748. Dostupné z: doi:10.1063/1.1149043

[66] ANAS, Emran, Soo LEE a Md. HASAN. Removal of ring artifacts in CT imaging through detection and correction of stripes in the sinogram. *Physics in Medicine and Biology*. 2010, **55**(22), 6911-6930. ISSN 0031-9155. Dostupné z: doi:10.1088/0031-9155/55/22/020

[67] LIANG, Xiaokun, Zhicheng ZHANG, Tianye NIU, Shaode YU, Shibin WU, Zhicheng LI, Huailing ZHANG a Yaoqin XIE. Iterative image-domain ring artifact removal in cone-beam CT. *Physics in Medicine & Biology*. 2017, **62**(13), 5276-5292. ISSN 0031-9155. Dostupné z: doi:10.1088/1361-6560/aa7017

[68] GILBERT, Peter. Iterative methods for the three-dimensional reconstruction of an object from projections. *Journal of Theoretical Biology*. 1972, **36**(1), 105-117. ISSN 00225193. Dostupné z: doi:10.1016/0022-5193(72)90180-4

[69] JI, Dongjiang, Gangrong QU a Baodong LIU. Simultaneous algebraic reconstruction technique based on guided image filtering. *Optics Express*. 2016, **24**(14), 15897-15911. ISSN 1094-4087. Dostupné z: doi:10.1364/OE.24.015897

[70] ARGYROU, Maria, Dimitris MAINTAS, Charalampos TSOUMPAS a Efstathios STILIARIS. Tomographic Image Reconstruction based on Artificial Neural Network (ANN) techniques. In: *2012 IEEE Nuclear Science Symposium and Medical Imaging Conference Record (NSS/MIC)*. IEEE, 2012, s. 3324-3327. ISBN 978-1-4673-2030-6. Dostupné z: doi:10.1109/NSSMIC.2012.6551757

[71] BUSHBERG, J. T., J. A. SEIBERT, E. M.Jr LEIDHOLDT a J. M. BOONE. *The Essential Physics of Medical Imaging:*. Third Edition. Philadelphia, PA, USA,: Lippincott Williams & Wilkins, 2012, 1048 pp. ISBN 9780781780575. Dostupné z: doi:10.1118/1.4811156

[72] BALLABRIGA, R., J. ALOZY, F. N. BANDI et al. Photon Counting Detectors for X-Ray Imaging With Emphasis on CT. *IEEE Transactions on Radiation and Plasma Medical Sciences*. 2021, **5**(4), 422-440. ISSN 2469-7311. Dostupné z: doi:10.1109/TRPMS.2020.3002949

[73] LLOPART, X., R. BALLABRIGA, M. CAMPBELL, L. TLUSTOS a W. WONG. Timepix, a 65k programmable pixel readout chip for arrival time, energy and/or photon counting measurements. *Nuclear Instruments and Methods in Physics Research Section A: Accelerators, Spectrometers, Detectors and Associated Equipment*. 2007, **581**(1-2), 485-494. ISSN 01689002. Dostupné z: doi:10.1016/j.nima.2007.08.079

[74] SHEPP, L. A. a Y. VARDI. Maximum Likelihood Reconstruction for Emission Tomography. *IEEE Transactions on Medical Imaging*. 1982, **1**(2), 113-122. ISSN 0278-0062. Dostupné z: doi:10.1109/TMI.1982.4307558

[75] DE MAN, B., J. NUYTS, P. DUPONT, G. MARCHAL a P. SUETENS. An iterative maximum-likelihood polychromatic algorithm for CT. *IEEE Transactions on Medical Imaging*. 2001, **20**(10), 999-1008. ISSN 02780062. Dostupné z: doi:10.1109/42.959297

[76] KAMPSCHULTE, M., A. LANGHEINIRCH, J. SENDER et al. Nano-Computed Tomography: Technique and Applications. *RöFo - Fortschritte auf dem Gebiet der Röntgenstrahlen und der bildgebenden Verfahren*. 2016, **188**(02), 146-154. ISSN 1438-9029. Dostupné z: doi:10.1055/s-0041-106541

[77] BARRETT, Julia F. a Nicholas KEAT. Artifacts in CT: Recognition and Avoidance. *RadioGraphics*. 2004, **24**(6), 1679-1691. ISSN 0271-5333. Dostupné z: doi:10.1148/rg.246045065

[78] PANG, Sing Chin a Sebastian GENNA. Corrections for X-Ray Polychromaticity Effects on Three-Dimensional Reconstruction. *IEEE Transactions on Nuclear Science*. 1976, **23**(1), 623-626. ISSN 0018-9499. Dostupné z: doi:10.1109/TNS.1976.4328316

[79] NALCIOGLU, O a R Y LOU. Post-reconstruction method for beam hardening in computerised tomography. *Physics in Medicine and Biology*. 1979, **24**(2), 330-341. ISSN 00319155. Dostupné z: doi:10.1088/0031-9155/24/2/009

[80] PACK, Jed D, Frédéric NOO a H KUDO. Investigation of saddle trajectories for cardiac CT imaging in cone-beam geometry. *Physics in Medicine and Biology*. 2004, **49**(11), 2317-2336. ISSN 0031-9155. Dostupné z: doi:10.1088/0031-9155/49/11/014

[81] CHEN, Zikuan, Vince D. CALHOUN a Shengjiang CHANG. Compensating the intensity fall-off effect in cone-beam tomography by an empirical weight formula. *Applied Optics*. 2008, **47**(32). ISSN 0003-6935. Dostupné z: doi:10.1364/AO.47.006033

[82] LIU, Tong. Comparison between four methods for central ray determination with wire phantoms in micro-computed-tomography systems. *Optical Engineering*. 2006, **45**(6). ISSN 0091-3286. Dostupné z: doi:10.1117/1.2214717

[83] JUN, Kyungtaek a Seokhwan YOON. Alignment Solution for CT Image Reconstruction using Fixed Point and Virtual Rotation Axis. *Scientific Reports*. 2017, **7**(1). ISSN 2045-2322. Dostupné z: doi:10.1038/srep41218

[84] VO, Nghia T., Michael DRAKOPOULOS, Robert C. ATWOOD a Christina REINHARD. Reliable method for calculating the center of rotation in parallel-beam tomography. *Optics Express*. 2014, **22**(16). ISSN 1094-4087. Dostupné z: doi:10.1364/OE.22.019078

[85] DONATH, Tilman, Felix BECKMANN a Andreas SCHREYER. Automated determination of the center of rotation in tomography data. *Journal of the Optical Society of America A*. 2006, **23**(5). ISSN 1084-7529. Dostupné z: doi:10.1364/JOSAA.23.001048

[86] VISKOE, A. Computed tomography postacquisition data correction for system alignment errors. *IEEE Transactions on Instrumentation and Measurement*. IEEE, 1999, **48**(5), 972-977. ISSN 00189456. Dostupné z: doi:10.1109/19.799656

[87] GARNETT, Richard. A comprehensive review of dual-energy and multi-spectral computed tomography. *Clinical Imaging*. 2020, **67**(), 160-169. ISSN 08997071. Dostupné z: doi:10.1016/j.clinimag.2020.07.030

[88] D'ANGELO, Tommaso, Giuseppe CICERO, Silvio MAZZIOTTI et al. Dual energy computed tomography virtual monoenergetic imaging: technique and clinical applications. *The British Journal of Radiology*. 2019, **92**(1098). ISSN 0007-1285. Dostupné z: doi:10.1259/bjr.20180546

[89] LONG, Yong a Jeffrey A. FESSLER. Multi-Material Decomposition Using Statistical Image Reconstruction for Spectral CT. *IEEE Transactions on Medical Imaging*. 2014, **33**(8), 1614-1626. ISSN 0278-0062. Dostupné z: doi:10.1109/TMI.2014.2320284

[90] NIU, Tianye, Xue DONG, Michael PETRONGOLO a Lei ZHU. Iterative image-domain decomposition for dual-energy CT. *Medical Physics*. 2014, **41**(4). ISSN 00942405. Dostupné z: doi:10.1118/1.4866386

# Author's publications and other outputs

## Publications

### First-author

**ŠALPLACHTA, J.**; ZIKMUND, T.; ZEMEK, M.; BŘÍNEK, A.; TAKEDA, Y.; OMOTE, K.; KAISER, J. Complete Ring Artifacts Reduction Procedure for Lab-Based X-ray Nano CT Systems. *SENSORS,* 2021, vol. 21, no. 1, p. 1-20. ISSN: 1424-8220.

### Shared first-author

**HANKEOVÁ, S.; ŠALPLACHTA, J.;** VAN HUL, N.; KAVKOVÁ, M.; IQBAL, A.; ZIKMUND, T.; KAISER, J.; ANDERSSON, E. DUCT: Double Resin Casting followed by Micro-Computed Tomography for 3D Liver Analysis. *Journal of visualized experiments : JoVE,* 2021, vol. 175, no. e62941, p. 1-19. ISSN: 1940-087X.

**HANKEOVÁ, S.; ŠALPLACHTA, J.;** ZIKMUND, T.; KAVKOVÁ, M.; VAN HUL, N.; BŘÍNEK, A.; SMÉKALOVÁ, V.; LÁZŇOVSKÝ, J.; DAWIT, F.; JAROŠ, J.; BRYJA, V.; LENDAHL, U.; ELLIS, E.; NEMETH, A.; FISCHLER, B.; HANNESO, E.; KAISER, J.; ANDERSSON, E. DUCT reveals architectural mechanisms contributing to bile duct recovery in a mouse model for Alagille syndrome. *eLife,* 2021, no. 10, p. 1-29. ISSN: 2050-084X.

### Co-author

CASTALDO, R.; AVOLIO, R.; COCCA, M.; ERRICO, M.; LAVORGNA, M**.; ŠALPLACHTA, J**.; SANTILLO, CH.; GENTILE, G. p Hierarchically porous hydrogels and aerogels based on reduced graphene oxide, montmorillonite and hyper-crosslinked resins for water and air remediation. *CHEMICAL ENGINEERING JOURNAL,* 2022, vol. 430, no. 4, p. 1-10. ISSN: 1385-8947.

MATULA, J.; POLÁKOVÁ, V.; **ŠALPLACHTA, J.**; TESAŘOVÁ, M.; ZIKMUND, T.; KAUCKÁ, M.; ADAMEYKO, I.; KAISER, J. Resolving complex cartilage structures in developmental biology via deep learning-based automatic segmentation of X-ray computed microtomography images. *Scientific Reports,* 2022, vol. 12, no. 1, p. 1-13. ISSN: 2045-2322.

KAVKOVÁ, M.; ZIKMUND, T.; KALA, A.; **ŠALPLACHTA, J.**; LISSETTE PROSKAUER PENA, S.; KAISER, J.; JEŽEK, K. Contrast enhanced X-ray computed tomography imaging of amyloid plaques in Alzheimer disease rat model on lab based micro CT system. *Scientific Reports,* 2021, vol. 11, no. 1, p. 1-10. ISSN: 2045-2322.

JAQUES, V.; DU PLESSIS, A.; ZEMEK, M.; **ŠALPLACHTA, J.**; ŠTUBIANOVÁ, Z.; ZIKMUND, T.; KAISER, J. Review of porosity uncertainty estimation methods in computed tomography dataset. *Measurement Science and Technology,* 2021, vol. 32, no. 8, p. 1-17. ISSN: 0957-0233.

OLIVER, C.; IBAÑEZ, R.; FLORES-MERINO, M.; VOJTOVÁ, L.; **ŠALPLACHTA, J.**; ČELKO, L.; KAISER, J.; MONTUFAR JIMENEZ, E. Lyophilized Polyvinylpyrrolidone Hydrogel for Culture of Human Oral Mucosa Stem Cells. *Materials,* 2021, vol. 14, no. 1, p. 1-14. ISSN: 1996-1944.

GAMBLE, J.; TOBYN, M.; ZHANG, S.; ZHU, A.; **ŠALPLACHTA, J.**; MATULA, J.; ZIKMUND, T.; KAISER, J.; OBERTA, P. Characterization of the Morphological Nature of Hollow Spray Dried Dispersion Particles Using X-ray Submicron-Computed Tomography. *AAPS PHARMSCITECH,* 2021, vol. 23, no. 1, p. 1-7. ISSN: 1530-9932.

KUNISHIMA, N.; TAKEDA, Y.; HIROSE, R.; KALASOVÁ, D.; **ŠALPLACHTA, J.**, OMOTE, K. Visualization of internal 3D structure of small live seed on germination by laboratory-based X-ray microscopy with phase contrast computed tomography. *PLANT METHODS,* 2020, vol. 16, no. 1, p. 1-10. ISSN: 1746-4811.

ZIKMUND, T.; **ŠALPLACHTA, J.**; ZATOČILOVÁ, A.; BŘÍNEK, A.; PANTĚLEJEV, L.; ŠTĚPÁNEK, R.; KOUTNÝ, D.; PALOUŠEK, D.; KAISER, J. Computed tomography based procedure for reproducible porosity measurement of additive manufactured samples. *NDT & E INTERNATIONAL,* 2019, vol. 103, no. 1, p. 111-118. ISSN: 1879-1174.

VOJTOVÁ, L.; ZIKMUND, T.; PAVLIŇÁKOVÁ, V.; **ŠALPLACHTA, J.**; KALASOVÁ, D.; PROSECKÁ, E.; BRTNÍKOVÁ, J.; ŽÍDEK, J.; PAVLIŇÁK, D.; KAISER, J. The 3D imaging of mesenchymal stem cells on porous scaffolds using high-contrasted x-ray computed nanotomography. *Journal of Microscopy,* 2019, vol. 273, no. 3, p. 169-177. ISSN: 1365-2818.

PROCHAZKA, D.; ZIKMUND, T.; POŘÍZKA, P.; BŘÍNEK, A.; KLUS, J.; **ŠALPLACHTA, J.**; NOVOTNÝ, J.; KAISER, J. Joint utilization of double-pulse laser-induced breakdown spectroscopy and X-ray computed tomography for volumetric information of geological samples. *Journal of Analalytical Atomic Spectrometry,* 2018, no. 9, p. 1-7. ISSN: 0267-9477.

## Products

KALASOVÁ, D.; **ŠALPLACHTA, J.**; PAVLIŇÁKOVÁ, V.; ZIKMUND, T.; KAISER, J.: Sample's holder nanoCT – SEM. (functional sample)

**ŠALPLACHTA, J**.; TESAŘOVÁ, M.; ZEMEK, M.; KAISER, J.: Sample's holder with reference area. (functional sample)

## Grants

**March 2020** **CEITEC Specific research programme** – main solver

**– February 2021** **Project name:** 3D visualization of Lithium-ion batteries internal structures by X-ray microscope Rigaku nano3DX.

**May 2019** **TAČR programme ZETA** – member of participating team

**– April 2021** **Project name:** Differentiation of soft tissues using dual-target tomography.

**Role in team:** Software and algorithms development for CT data registration and tomographic reconstruction. Development and optimization of sample holder with reference area for data registration.

**January 2018** **TAČR programme ZETA** – member of participating team

**– December 2019** **Project name:** Advanced techniques for biological samples imaging using X-ray computed nanotomography.

**Role in team:** Software and algorithms development for CT data analysis and post-processing.

**March 2019** **CEITEC Specific research programme** – main solver

**– February 2020** **Project name:** Data registration for Dual-Target X-ray nano Computed tomography

**March 2018** **CEITEC Specific research programme** – main solver

**– February 2019** **Project name:** Quantitative nano computed tomography

## Conferences

**5th International Conference on Tomography of Materials and Structures (ICTMS 2020)**

27.6. – 1. 7. 2022, Grenoble, France

**Oral presentation:** Beyond the limits of lab-based submicron CT for metrology

**9th Conference on Industrial Computed Tomography (ICT 2019)**

13. – 15. 2. 2019, Padova, Italy

**Poster:** CCD and scientific-CMOS detectors for submicron laboratory- based X-ray Computed Tomography

**12th International Conference on Computer Graphics, Visualization, Computer Vision and Image Processing (CGVCVIP 2018)**

18 – 20 July 2018, Madrid, Spain

**Poster:** Denoising approach for high-resolution computed tomography data